Nanocrystalline oxides prepared by mechanochemical reactions

Von der Fakultät für Lebenswissenschaften

der Technischen Universität Carolo-Wilhelmina

zu Braunschweig

zur Erlangung des Grades eines

Doktors der Naturwissenschaften

(Dr. rer. nat.)

genehmigte

Dissertation

von Maksym Myndyk
aus Mshana, Lviv region, Ukraine

1. Referent: Prof. Dr. Klaus Dieter Becker
2. Referent: Prof. Dr. Fred Jochen Litterst
eingereicht am: 14.12.2009
mündliche Prüfung (Disputation) am: 04.03.2010

Druckjahr 2010

Dissertation an der Technischen Universität Braunschweig,
Fakultät für Lebenswissenschaften

Vorveröffentlichungen der Dissertation

Teilergebnisse aus dieser Arbeit wurden mit Genehmigung der Fakultät für Lebenswissenschaften, vertreten durch die Mentor der Arbeit, in folgenden Beiträgen vorab veröffentlicht:

Publikationen

*V. Šepelák, M. Myndyk, J. Bednarcik, D. Trots, K. D. Becker, Thermal stability of polycrystalline FeS powder investigated by in-situ XRD. *Annual Report Deutsches Electronen-Synchrotron (HASYLAB) 2007, Part 1,* (2008) 881.

D. Bellušova, T. Alshuth, R. H. Schuster, M. Myndyk, V. Šepelák, I. Hudec, Influence of barium ferrites on the performance of BR-elastomers. *Kautschuk Gummi Kunststoffe* 3 (2008) 118.

M. J. Nasr Isfahani, M. Myndyk, V. Šepelák, J. Amighian, A Mössbauer effect investigation of the formation of MnZn nanoferrite phase. *Journal of Alloys and Compounds* 470 (2009) 434.

M. J. Nasr Isfahani, M. Myndyk, D. Menzel, A. Feldhoff, J. Amighian, V. Šepelák, Magnetic properties of nanostructured MnZn ferrite. *Journal of Magnetism and Magnetic Materials* 231 (2009) 152.

*A. Feldhoff, J. Martynczuk, M. Arnold, M. Myndyk, I. Bergmann, V. Šepelák, U. Vogt, A. Hähnel, J. Woltersdorf, Spin-transition of iron in the perovskite-type $(Ba_{0.5}Sr_{0.5})(Fe_{0.8}Zn_{0.2})O_{3-\delta}$ oxygen-ion and electron mixed conductor. *Journal of Solid State Chemistry* 182 (2009) 2961.

*E. Turianicová, Z. Orolinová, P. Baláž, M. Myndyk, M. Fabian, V. Šepelák, ^{57}Fe Mössbauer study of olivine $(Mg,Fe)_2SiO_4$ milled in industrially eccentric vibratory mill. *Chemical Papers* (2009), submitted.

Tagungsbeiträge

*M. Myndyk, A. Feldhoff, K. D. Becker, Mössbauer spectroscopy of iron sulfides. *99th Bunsen Colloquium on Solid State Reactivity: From Macro to Nano*, 7-9 July 2007, Monastery Eberbach, Germany.

M. Myndyk, A. Feldhoff, D. Menzel, K. D. Becker, V. Šepelák, Nanocrystalline $BaFe_{12}O_{19}$ and $SrFe_{12}O_{19}$ hexaferrites prepared by top-down approach. *ZFM Students Conference 2008*, 20 February 2008, Hannover, Germany.

---

*The results of the work are not included in the Thesis.

M. Myndyk, D. Menzel, D. Bellušová, A. Feldhoff, R. H. Schuster, K. D. Becker, V. Šepelák, Size-dependent magnetic properties of nanocrystalline $BaFe_{12}O_{19}$ and $SrFe_{12}O_{19}$ hexaferrites. *8th Conference on Solid State Chemistry*, 6-11 July 2008, Bratislava, Slovakia.

M. Myndyk, D. Bellušova, A. Feldhoff, R. H. Schuster, K. D. Becker, V. Šepelák, Local structure and size-dependent magnetic properties of nanocrystalline $BaFe_{12}O_{19}$ and $SrFe_{12}O_{19}$. *Mössbauer Colloquium: 50 Years after – The Mössbauer effect today and in the future*, 9-10 October 2008, Munich, Germany

M. Myndyk, M. J. Nasr Isfahani, D. Menzel, A. Feldhoff, J. Amighian, V. Šepelák, K. D. Becker, Mechanosynthesis and magnetic properties of nanostructured MnZn ferrite. *Seminar: 10 Years Cooperation between TU Braunschweig and Slovak Academy of Sciences, Košice*, 18-20 February 2009, Košice, Slovakia.

[#]M. Myndyk, M. J. Nasr Isfahani, D. Menzel, A. Feldhoff, J. Amighian, K. D. Becker, V. Šepelák, Mechanosynthesis and magnetic properties of nanostructured MnZn ferrite. *Bunsentagung 2009*, 21-23 May 2009, Köln, Germany.

M. Myndyk, M. J. Nasr Isfahani, D. Menzel, A. Feldhoff, J. Amighian, K. D. Becker, V. Šepelák, Mechanosynthesis and magnetic properties of nanostructured MnZn ferrite. *The International Scientific Workshop: Oxide Materials for Electronic Engineering – Fabrication, Properties and Application, OMEE-2009*, 22-26 June 2009, Lviv, Ukraine.

M. Myndyk, M. J. Nasr Isfahani, D. Menzel, A. Feldhoff, J. Amighian, K. D. Becker, V. Šepelák, Mechanosynthesis and magnetic properties of nanostructured MnZn ferrite. Local structure and magnetic behavior of nanocrystalline MnZn spinel ferrite prepared by a one-step mechanochemical route, *Bunsen Colloquium: Spectroscopic Methods in Solid State Diffusion and Reactions,* 24-25 September 2009, Hannover, Germany.

[#] The work was awarded the *PCCP Hot Topic Poster Prize*, Bunsentagung 2009, Köln

Contents

1 Introduction

2 Experimental

Attachment

Acknowledgement

The results presented in this PhD Thesis have been achieved within my graduate studies (2005-2009) at the Solid State Chemistry Group (Institute of Physical and Theoretical Chemistry, Braunschweig University of Technology) in the framework of the Graduate Programme *“New Materials with Tailored Properties”* established at the Center of Solid State Chemistry and New Materials (ZFM) at the Leibniz University Hannover - one of the main centres for chemically orientated solid state research in Germany. My sincere thanks go to the State of the Lower Saxony for the support of my work within a *Georg Christoph Lichtenberg Stipend*.

I am grateful for the professional supervision to Professor Klaus Dieter Becker and Professor Vladimír Šepelák, who oriented me towards the study of problems with which I deal in my Thesis and who were permanently interested in my work. I would like to acknowledge the support and hospitality extended to me by the staff of the Solid State Chemistry Group, especially to Mrs. Kerstin-Ilona Talk and Mrs. Angela Tiefnig. The scientific discussions with Mr. Klebson Lucenildo da Silva and Dr. Jens Röder have helped me to interpret some of the experimental results.

I have had the good fortune to associate with one of the outstanding Mössbauer spectroscopy laboratories. This enabled me to investigate the structure of nanocrystalline materials on the local atomic scale. A three months research stay at the Brazilain Center for Physics Research (CBPF) in Rio de Janeiro (Brazil) allowed me to perform Mössbauer measurements at low temperatures and under an applied external magnetic field. I thank very much for this opportunity Professor Fred Jochen Litterst (Institute of Condensed Matter Physics, TU Braunschweig) as well as Professor Elisa Baggio Saitovitch (CBPF).

With great gratitude I acknowledge the scientific cooperations with Professor Robert-Hans Schuster and Ms. Denisa Belusova (German Institute of Rubber Technology, Hannover), Dr. Armin Feldhoff (Leibniz University Hannover), Dr. Jozef Bednarčík (DESY, Hamburg), and Dr. Dirk Menzel (TU Braunschweig), who have directly or indirectly contributed to this work.

I would like to express my gratitude to Dr. L. John Berchmans (Central Electrochemical Research Institute, Karaikudi, India), Mrs. Janetta Žaková, Ms. Zuzana Orolínová and Dr. Martin Fabián (Slovak Academy of Sciences, Košice, Slovakia), Mr. M. J. Nasr Isfahani (University of Isfahan, Iran), and Mr. Adrian Constantinescu (Linde, Munich) whose scientific advices and assistance I appreciate very much.

Finally, I thank my mother, father, sister Yulja and my girlfriend Galja for their understanding and encouragement to achieve this task.

Braunschweig *Maksym Myndyk*
November 2009

1 Introduction

1.1 Nanostructured Materials

In 1959 at the California Institute of Technology, Nobel laureate physicist Richard Feynman delivered his now famous lecture “There is Plenty of Room at the Bottom” [1]. He stimulated his audience with the vision of exciting new discoveries if one could fabricate materials and devices at the atomic/molecular scale. He pointed out that, for this to happen, a new class of miniaturized instrumentation would be needed to manipulate and measure the properties of these small “nano”– structures. He was talking about nanoparticles, nanostructured materials, and nanodevices before these words existed. It was not until the 1980s that instruments were invented with the capabilities Feynman envisioned. These instruments, including scanning tunneling microscopes, atomic force microscopes, and near-field microscopes, provide the “eyes” and “fingers” required for nanostructure measurement and manipulation [2]. In a parallel development, expansion of computational capability enabled sophisticated simulations of material behavior at the nanoscale. These new tools and techniques have sparked excitement throughout the scientific community. Scientists from many disciplines are now avidly fabricating and analyzing nanostructures to discover novel phenomena based on *structures with at least one dimension under the “critical scale length” of 100 nm*.

Almost any property in a solid is associated with a particular length scale, and below this length, the property will vary. When characteristic structural features are intermediate in extent between isolated atoms and bulk materials, in the range of about 10^{-9} to 10^{-7} m (1 to 100 nm), the objects often display physical attributes substantially different from those displayed by either atoms or bulk materials. By creating nanometer-scale structures, it is possible to control fundamental properties of materials like their melting temperature, magnetic properties, charge capacity, and even their color, without changing the material’s chemical composition. Properties of matter at the nanoscale are not necessarily predictable from those observed at larger scales. Important changes in behavior are caused not only by continuous modification of characteristics with diminishing size, but also by the emergence of totally new phenomena such as quantum size confinement, wave-like transport, and predominance of interfacial phenomena [3]. Utilizing the potential of nanoscale structures leads to new, high-performance technologies that were not possible before. This also creates great opportunities for fundamental science in condensed matter physics, solid state chemistry, materials science, electrical engineering, biology, and other disciplines.

The field of nanostructure science and technology is a broad and interdisciplinary area of worldwide research and development activity. It has been growing explosively in the past years, since the realization that creating new materials and devices from nanoscale building blocks could access new and improved properties and functionalities. The field is simply too large, too geographically dispersed, and changing too rapidly to cover exhaustively [4].

Therefore, what this introductory Section of the Thesis presents is only a brief description of the field of nanoscience and nanostructured materials. Rigorous reviews of the field and a worldwide study of research and development status and trends in nanoparticles, nanostructured materials, and nanodevices may be found in several recent reviews, monographs, and conference proceedings [5-8].

There is a wide range of disciplines contributing to the developments in nanostructure science and technology worldwide. An ever increasing number of researchers from diverse disciplines enter the field, and an ever increasing breadth of novel ideas and exciting new opportunities explode on the international nanostructure scene. The rapidly mounting level of interdisciplinary activity in nanostructuring is truly exciting. Exploring the science of nanostructures has become a new theme common to many established disciplines. In electronics, nanostructures represent the step into quantum devices and fundamentally new processor architectures. In molecular biology, nanostructures are the fundamental machines that drive the cell - histones and proteosomes - and they are components of the mitochondrion, the chloroplast, the ribosome, and the replication and transcription complexes. In catalysis, nanostructures are the templates and pores of zeolites and other vitally important structures. In materials science, the nanometer length scale is the largest one over which a crystal can be made essentially perfect. Each of these disciplines has evolved its own separate view of nanoscience; the opportunities for integrating these views and for sharing tools and techniques developed separately by each field are today among the most attractive in all of science.

There is a very wide range of diverse synthesis and assembly strategies being employed in nanostructuring, all the way from fundamental biological methods for self-assembling molecules, to sophisticated chemical precipitation methods, to a variety of physical and chemical techniques for making clusters or nanoparticles (e.g., generation of nanoparticles including nano-clusters, -layers, -tubes, and two- and three-dimensional nanostructures via aerosols, colloids, plasma, combustion, sol-gel, chemical vapor deposition, high-energy milling, molecular and cluster assembling, and other synthesis methods). All of these strategies contribute in essential ways to the growth of this field. Each may have unique capabilities that will benefit a particular property, application, or process. Each method employed to produce nanostructured materials has advantages and disadvantages depending on the desired properties or application.

1.2 Nanocrystalline Materials Prepared by Mechanochemical Methods

Increased activity in the synthesis of nanocrystalline materials in recent years dates back to the pioneering investigations of Gleiter [9] of the Saarland University in Germany in 1981. He synthesized ultrafine nanoscale metallic particles using an inert gas condensation technique and consolidated them into small discs under ultrahigh vacuum conditions. Since 1981 a number of synthesis and assembly strategies have been developed in which the starting material can be either in the solid, liquid, or gaseous states [10]. The methods which have been commonly employed to synthesize nanoscale materials include, for example, inert gas condensation, spray conversion processing, controlled crystallization of amorphous phases, vapour deposition, coprecipitation, sol-gel process, plasma processing, laser ablation, hydrothermal pyrolysis, sonochemical processing, as well as mechanochemical processing. The later method becomes more widely used at present due to its relative simplicity and availability. Correspondingly, terms such as *mechanochemistry*, *mechanical activation*, *mechanosynthesis*, *mechanical alloying*, or various variants, are becoming increasingly common in the materials sciences the condensed matter physics, and chemistry literature [11]. Mechanochemical techniques have been most commonly employed to produce large quantities of nanocrystalline materials [10], and they can deliver the designed phases and structures by single step processing of materials in a closed activation chamber at room temperature. A typical mechanochemical reactor (high-energy ball mill) of the planetary type is depicted in Fig. 1.1 [12].

The first systematic papers concerned with the mechanical activation on properties of substances were published in the 19th century by Carey Lea [13]. He investigated the halides of gold, silver, platinum and mercury and observed that they decomposed to halogen and metal because of milling in a mortar. According to the author, the decomposition cannot be attributed to temperature because these substances exhibit sufficient thermal stability. Carey Lea was the first who pointed out that not only heat, light, and electric energy but also mechanical energy is able to initiate chemical reactions.

Fig. 1.1. Planetary mono mill “Pulverisette 6” (Fritsch, Idar-Oberstein, Germany) used in this work for the mechanochemical preparation of various nanooxides.

The term *mechanochemistry* was introduced by Ostwald [14] who was engaged in the systematization of chemical sciences from the energetic point of view. He understood mechanochemistry in a wider sense when compared with the present view, regarding it as a part of physical chemistry like thermochemistry, electrochemistry, sonochemistry or photochemistry. In German literature we also meet with the term tribochemistry [15]. At present the definition of mechanochemistry by Heinicke is widely accepted:
"Mechanochemistry is a branch of chemistry which is concerned with chemical and physical transformations of substances in all states of aggregation produced by the effect of mechanical energy" [15].

The term *mechanical activation* was introduced into the literature by Smékal [16] who regarded it as a process involving an increase in reaction ability of the substance. A central underlying theme in mechanical activation is to energize the material and to bring it into a highly nonequilibrium (activated/metastable) state through mechanical treatment. This may lead to an enhancement of reactivity of a solid in a subsequent process. The multi-step character of mechanical activation involves the accumulation of energy due to the formation of new surfaces, structural disorder in the bulk and even the change in the chemical composition of a solid [17]. The term *mechanochemical activation* instead of mechanical activation is better in this case [19].

Mechanical alloying technique, was developed around 1966 by Benjamin and his co-workers [19] as a part of the program to produce oxide dispersion strengthened Ni-base superalloys for gas turbine applications. The process of production of alloys by high-energy milling was initially referred to as milling/mixing. The term mechanical alloying was actually coined by Ewan C. McQueen [20]. Mechanical alloying has been widely used for the preparation of various nanocrystalline metals, amorphous alloys, intermetallic compounds, extended solid solution, nanocomposites, etc. One of the greatest advantages of this technique is its ability to produce novel alloys, i.e., alloying of normally immiscible elements [21], which is not possible by any other technique.

Despite the physical nature of the high-energy milling process, chemical changes can be detected in milled solids. These can be categorized along the same lines that are commonly used in solid state chemistry and in chemistry, in general. The mechanochemical preparation route to nanoscale solids proceeds through chemical reactions either of *homogeneous* or of *heterogeneous* type [22]. In the former, nanosized particles are produced by high-energy milling of a bulk material (*top-down approach*) without changes in its chemical composition. The homogeneous mechanochemical reactions include, for example, mechanically induced phase transformations, the formation of Schottky or Frenkel defects as well as mechanically induced structural disorder associated with the redistribution of cations over nonequivalent cation sublattices provided by a structure. In the case of a heterogeneous mechanochemical reaction between precursors, a new nanocrystalline phase can be formed as a result of the processing. The most important types of heterogeneous mechanochemical reactions are represented by formation reactions (mechanosynthesis) of compounds, reduction/oxidation (mechanochemical redox) reactions, and decomposition of compounds. The heterogeneous mechanochemical reaction, which includes several stages such as the mixing of precursors at the atomic level, the nucleation of the new phase and its growth, can be considered as a *bottom-up approach* for preparing nanostructured solids [23].

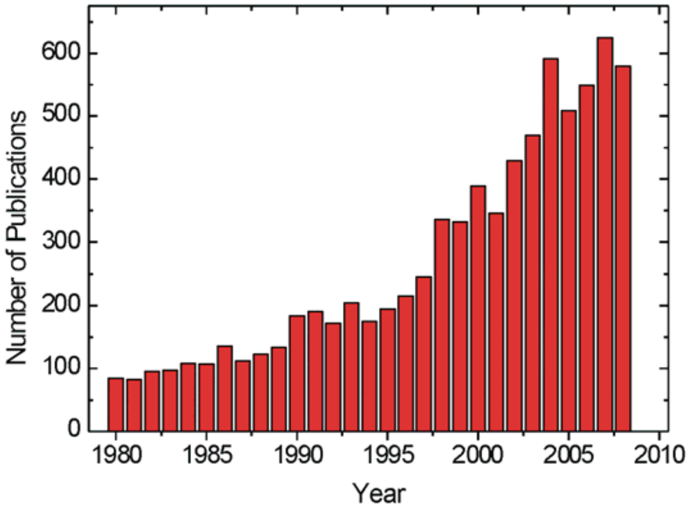

Fig. 1.2. The growth of number of publications in the field of mechanochemistry during the period 1980-2008. Source: SciFinder Scholar using the keyword "mechanochemistry"; State: June 13, 2009. The local maximum for the year 2004 is mostly related to the publication [11]: V. Šepelák, K. D. Becker, Z. A. Munir (Eds.), *Mechanochemistry and Mechanical Alloying 2003*. Kluwer Academic Publishers, Boston, 2004 [in: *J. Mater. Sci.* 39 (2004) pp. 4983-5530].

It should be emphasized that the synthesis of nanocrystalline materials based on mechanochemical methods is a rapidly expanding field of solid state science. The extent to which research developments are occurring in this field is reflected by the number of papers published on this topic in recent years. Figure 1.2 presents the growth of publications in the field during the period 1980-2008. A number of international conferences have been organized on the subject covering various aspects related to this wide field such as alloys, nanostructured materials, amorphization, structural disorder, mechanochemistry, metastable materials, powder metallurgy, etc.. Despite numerous efforts, the understanding of the nonequilibrium (far-from-equilibrium) mechanochemical processes is considered to be far from complete, leaving large scope for further research in this exciting field.

1.3 Relevance of the Theme and Aims of the PhD Thesis

Although important progress has been made in the study of nanocrystalline materials prepared by mechanochemical methods, there is still a number of open questions, whose solution could help to advance both their theory and practical applications.

Among the challenges facing mechanochemists are those concerned with the *structure characterization* of materials at ever finer size scales. We must be able to give a more detailed description of the mechanically induced structural disorder, and we must eventually use computational approaches for *structure refinement*, i.e., experiments revealing the structural features simply cannot do it alone; theory and modeling are essential. Another task is to fully understand the critical role that surfaces and interfaces play in nanostructured mechanically prepared materials. We need to know in detail not only the *structures of these interfaces*, but also their local chemistries and the effects of segregation and interaction between the nanocrystallites and their surroundings. Thus, for any picture of the properties of nanostructures to be complete, the nature of *the surface and interior disorder* must be determined.

Due to their finite sizes, the surface and interior structures of nanoscale materials prepared by mechanochemical routes may have particular importance for their chemical and physical properties. The *structure-property relationships* in nanoscale materials is also an area where there is a large scope for further research. In most of the mechanochemically prepared nanostructures, the physics underlying their behavior is understood only incompletely; there is an opportunity now to discover many new properties resulting from the mechanically induced disorder, from high ratios of surface to volume, or from some other aspects of small size.

Since nanostructures prepared by mechanochemical methods are often inherently unstable owing to their small constituent sizes and high chemical activity, we also need to be concerned with the *chemical and structural stability* of nanostructured materials.

In line with the above-mentioned challenges, the *aims of the Thesis* are directed towards basic research tightly connected to the present research trends in the field of mechanochemistry/solid state chemistry. The Thesis has the following overall aims:

- to prepare novel nanocrystalline oxides ($BaFe_{12}O_{19}$, $SrFe_{12}O_{19}$, $Mn_{0.5}Zn_{0.5}Fe_2O_4$, $CaFe_2O_4$, Fe_2SiO_4, $FeMgSiO_4$, Mg_2SiO_4, FeO-SnO_2 composites) via homogeneous and heterogeneous mechanochemical reactions;
- to demonstrate the possibility of performing various types of heterogeneous mechanochemical reactions in oxides such as mechanochemical formation reactions, mechanochemical redox reactions, and mechanochemical decomposition reactions;
- to obtain quantitative microstructural information on the mechanically induced structural disorder (nonequilibrium cation distribution, noncollinear spin arrangement, deformation of polyhedron geometry, etc.) in mechanochemically prepared oxides; to formulate on the basis of the structure refinement the origin of metastability of nanosized mechanically treated solids;
- to reveal unusual physical (magnetic) behavior of the mechanochemically prepared materials; to understand the unusual properties possessed by nanoscale oxides; to explain

the fundamental origin of the size-dependent magnetic properties of materials, i.e., to contribute to the understanding the structure-nanomagnetism relationship in solids prepared by mechanochemical routes.

The Thesis is divided into five Chapters. After the brief Introduction (Chapter 1) and Experimental (Chaper 2), the results achieved on Homogeneous Mechanochemical Reactions (Chapter 3) and Heterogeneous Mechanochemical Reactions (Chapter 4) are presented. Chapter 5 summarizes the results of the Thesis.

2 Experimental

2.1 Materials

The Thesis deals with the following oxide systems: $BaFe_{12}O_{19}$, $SrFe_{12}O_{19}$, $Mn_{0.5}Zn_{0.5}Fe_2O_4$, $CaFe_2O_4$, Fe_2SiO_4, $FeMgSiO_4$, Mg_2SiO_4, and FeO-SnO_2 composites.

The *M*-type barium hexaferrite ($BaFe_{12}O_{19}$) and strontium hexaferrite ($SrFe_{12}O_{19}$), used as starting materials for subsequent mechanochemical treatment (see Chapter 3), were synthesized using a chemically reliable co-precipitation route [24]. The precursor materials of barium chloride (respectively, strontium chloride) and iron chloride (99% purity) were dissolved in deionized water, and subsequently solutions of Na_2CO_3 and NaOH were added to achieve ph = 6. The precipitated precursors were sintered at 900 °C to obtain $BaFe_{12}O_{19}$ and $SrFe_{12}O_{19}$, respectively.

The starting $MnFe_2O_4$ and $ZnFe_2O_4$ materials used for subsequent mechanochemical synthesis of $Mn_{0.5}Zn_{0.5}Fe_2O_4$ (see Section 4.1), were prepared in polycrystalline form by a conventional solid state reaction [25]. Here stoichiometric mixtures of the constituent MnO_2/Fe_2O_3 and ZnO/Fe_2O_3 powders (Merck, Darmstadt, Germany) were homogenized in a ball mill. Powdered mixtures were pressed into tablets under a pressure of 30 MPa in a steel mold in order to obtain a high degree of compaction of the reactants. The tablets were 20 mm in diameter and 4 mm thick. The greenbodies were sintered at 1373 K in air for 3 h. The conventional ceramic synthesis of the $MnFe_2O_4$ and $ZnFe_2O_4$ spinel compounds was performed in air. At the completion of the sintering process, $MnFe_2O_4$ and $ZnFe_2O_4$ samples were removed from the furnace and cooled by water and air, respectively.

For the mechanochemical synthesis of $CaFe_2O_4$ (see Section 4.2), stoichiometric mixtures of α-Fe_2O_3 and CaO as well as α-Fe_2O_3 and granulated Ca (Merck, Darmstadt, Germany) were used as starting materials. Similarly, α-Fe_2O_3, Fe, MgO, and SiO_2 powders (Merck, Darmstadt, Germany) were used for the mechanosynthesis of nanocrystalline silicates $(Fe_{1-x}Mg_x)_2SiO_4$ ($x = 0$, 0.5 and 1), see Section 4.3. Finally, α-Fe_2O_3 and SnO (Merck, Darmstadt, Germany) were used for the preparation of FeO-SnO_2 nanocomposites (Section 4.4).

2.2 Mechanochemical Preparation of Nanooxides

Various special milling devices (mills) in which the high power density (of the order of 10^{-1}-10^{1} kW/m^3) is several times greater than in conventional tumbling mills (~ 10^{-2} kW/m^3) are used for ultrafine grinding and mechanochemical processing purposes [17]. They are termed *high-energy mills*. The majority of the mills used for experimental research in mechanochemistry and for production of small batches of nanomaterials are variants of the ball mill. The high energy associated with the heavy balls impacting on the powdered material produces, for example, the cold welding needed for either the formation of alloys, or, in the case of brittle materials, the fracture required for particle/crystallite size reduction. The last decade has been characterized by an extensive development of high-energy mills, so that a great variety of mills is available at present, differing in type, size, design, and performance [26]. The main types of high-energy mills currently used in the field of mechanical alloying or mechanochemistry include stirred ball mills or attritors, mixer mills, vibration mills, jet mills, and planetary mills. A detailed description of high-energy mills has been published in several monographs, e.g., [27-29].

There are various factors affecting the milling process such as type of mill, type of grinding media (balls, rods or other shapes), material of grinding tools (e.g., stainless steel, tungsten carbide, zirconium oxide, aluminum oxide, silicon nitride), grinding environment (e.g., vacuum, gas atmosphere - inert or reactive, wet environment - various liquids), ball-to-activated material mass ratio, grinding temperature, operating conditions of the mill (speed, frequency), milling time, etc. [26-29]. It should be emphasized that almost all studies on mechanochemistry report the time of mechanical treatment along with some of the milling parameters, such as the velocity of rotation for planetary mills, the ball-to-powder mass ratio, or the filling volume. All of these parameters directly affect the structure of the resulting milled material. In practice, however, it is sometimes difficult to compare results obtained in the study of the same or similar materials in different laboratories because of the different types of mills used. Systematic studies on the standardization of the milling conditions and their description have been proposed [30,31]. This standardization is important because of the availability of a wide range of different types of mills, each with their own individual characteristics and different milling conditions.

In order to prepare nanocrystalline $BaFe_{12}O_{19}$ and $SrFe_{12}O_{19}$ (see Chapter 3), these hexaferrites previously prepared by co-precipitation method were mechanically treated in a high-energy planetary mill Pulverisette 6 (Fritsch, Idar-Oberstein, Germany) in the Solid State Chemistry Group (Institute of Physical and Theoretical Chemistry, Technische Universität Braunschweig), see Fig. 1.1. The as-prepared samples (10 g) were ground for various times (up to 8 h) in a tungsten carbide (WC) grinding chamber. The volume of the grinding chamber was 250 cm^3. Balls made of WC with diameter of 10 mm were used. The ball-to-powder mass ratio was 20:1. Grinding experiments were performed in air at 600 rpm.

Fig. 2.1. SPEX 8000M mixer/mill (Spex CertiPrep Inc., USA) used in this work for the mechanochemical preparation of nanocrystalline $Mn_{0.5}Zn_{0.5}Fe_2O_4$ and FeO-SnO_2 nanocomposites.

To prepare nanostructured $Mn_{0.5}Zn_{0.5}Fe_2O_4$ by mechanosynthesis (see Section 4.1), single phase $MnFe_2O_4$ and $ZnFe_2O_4$ ferrites were thoroughly ground in an agate mortar in the ratio appropriate for the reaction: $MnFe_2O_4 + ZnFe_2O_4 \rightarrow 2\ Mn_{0.5}Zn_{0.5}Fe_2O_4$. Then, a total of 5 g of the powders, together with four 9 mm and three 12 mm hardened steel balls were loaded in a hardened steel vial and milled in air for various times (up to 30 h) in a SPEX 8000M mixer/mill (Spex CertiPrep Inc., USA) at room temperature. The ball-to-powder mass ratio was 7:1. In the case of the mechanochemical preparation of FeO-SnO_2 nanocomposites (Section 4.4), the α-Fe_2O_3/SnO mixtures were mechanically treated under the same conditions as those used for the mechanosynthesis of $Mn_{0.5}Zn_{0.5}Fe_2O_4$. The SPEX 8000M mixer/mill is depicted in Fig. 2.1.

The mechanochemical route was used for the preparation of nanostructured $CaFe_2O_4$ and of silicates $(Fe_{1-x}Mg_x)_2SiO_4$ ($x = 0$, 0.5 and 1), see Sections 4.2 and 4.3. In the case of the mechanosynthesis of $CaFe_2O_4$, two different mixtures of precursors (5 g), CaO and α-Fe_2O_3 as well as Ca and α-Fe_2O_3, were milled in air for various times (up to 12 h) in a Pulverisette 6 planetary ball mill (600 rpm; the ball-to-powder mass ratio: 40:1). In the case of silicates, 10 g of the α-Fe_2O_3/Fe/MgO/SiO_2 mixtures with the stoichiometry required for the compositions $(Fe_{1-x}Mg_x)_2SiO_4$ with $x = 0$, 0.5, and 1, were mechanically treated under argon atmosphere in the same mill at 600 rpm (the ball-to-powder mass ratio 20:1). In both cases, the grinding chamber (250 cm^3 in volume) and balls (10 mm in diameter) made of WC were used.

2.3 Experimental Methods

^{57}Fe and ^{119}Sn *Mössbauer spectroscopy*, as one of the main nuclear spectroscopic techniques, have extensively been employed in this Thesis to investigate local structures and the role that these play in controlling the properties of mechanochemically prepared nanoscale oxides. These methods enable one to follow the mechanochemical preparation route to Fe-containing as well as to Sn-containing nanoscale oxides. Moreover, they provided quantitative microstructural information on both ionic and spin configurations within the oxide nanoparticles.

^{57}Fe Mössbauer spectroscopy, as a nuclear probe technique, is very well suited for the investigation of the local symmetry, the magnetic state, and the charge state of iron ions in Fe-containing materials. This local sensitivity is due to interactions of the ^{57}Fe nuclei with their neighborhood. The main aim of this Section is to briefly outline the *hyperfine interactions* in order to facilitate the understanding of the following main Chapters.

In ferrite materials, which are the main subject of this Thesis, Mössbauer spectra are often dominated by *magnetic interactions*. The splitting of the characteristic six-line spectra reveals the local magnetic fields (H) at the positions of the Mössbauer nuclei. At room temperature and at lower temperatures, these fields often are of the order of 50 T [32].

Quadrupolar interaction (QS) of the Mössbauer nuclei reflects local symmetry. Here, the symmetry of the charge distribution is experienced through the electric field gradients set up the charges surrounding the nuclei. In the case of ferric ions, this interaction is dominated by the distribution of ionic charges in the lattice. On the other hand, the *isomer shift* (IS) reflects the electron density at the nuclei. This interaction causes a marked dependence of the position of the Mössbauer transition on the charge state of the Mössbauer ion and, to a lesser extent, on the geometry of its coordination.

Because of its great sensitivity to the magnetic fluctuations, ^{57}Fe Mössbauer spectroscopy was found to be a suitable technique for the detection of *superparamagnetism*. Such magnetic fluctuations can, however, complicate the analysis of spectra by a collapse of the magnetic hyperfine field far below the Néel temperature and give rise to relaxation line broadening and even down to very low temperatures - to unresolved hyperfine field distributions [33].

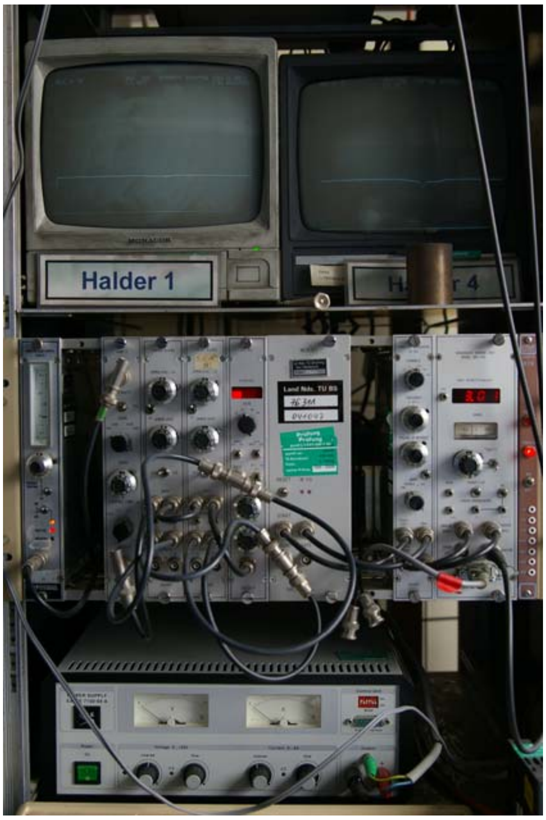

Fig. 2.2. Electronic setup of Mössbauer spectrometer in the Solid State Chemistry Group (Institute of Physical and Theoretical Chemistry, Braunschweig University of Technology).

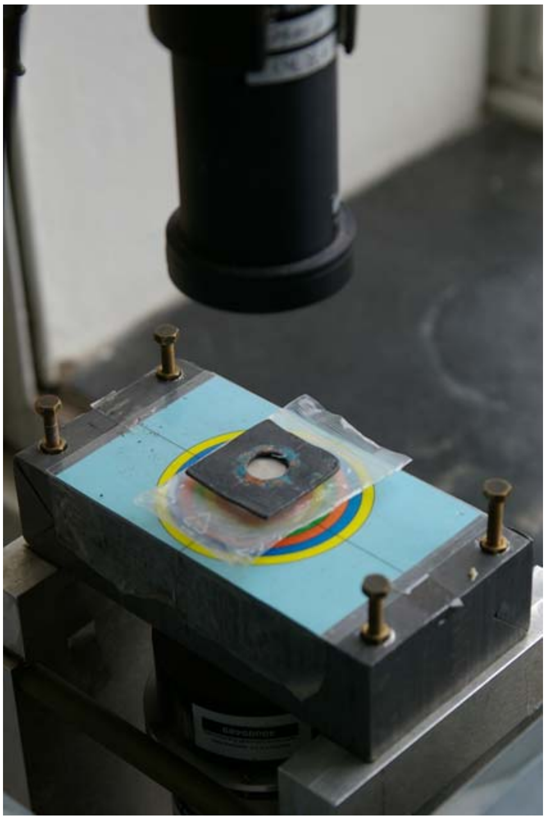

Fig. 2.3. Detailed view on the sample holder (bottom) and detector (top) used in this work for Mössbauer spectroscopic measurements in the Solid State Chemistry Group.

In this work, the room-temperature ^{57}Fe Mössbauer spectroscopy measurements without magnetic field were performed in transmission geometry using a microcomputer-controlled spectrometer in sinusoidal velocity sweep in the Mössbauer Laboratory of the Solid State Chemistry Group (Institute of Physical and Theoretical Chemistry, Braunschweig University of Technology), see Figs 2.2 and 2.3.

High-field Mössbauer measurements were carried out at 4.2 K in an external magnetic field of 7 T applied parallel to the γ-ray direction. These measurements were performed by the candidate during his three months research stay at the Brazilian Center for Physics Research (CBPF) in Rio de Janeiro. Figure 2.4 displays the Mössbauer spectrometer at CBPF.

Fig. 2.4. Mössbauer spectrometer consisting of a cryostat (left) and electronic setup (right) used in this work for low-temperature (4.2 K) in-field (7 T) Mössbauer measurements at CBPF in Rio de Janeiro.

For ^{57}Fe Mössbauer spectroscopic measurements, a ^{57}Co/Rh γ-ray source was used. 'Recoil' spectral analysis software [34] was used for the quantitative evaluation of the Mössbauer spectra. The spectra consist of distribution of hyperfine interaction which are fitted using Voigt profile. Populations of iron cations on various sublattices provided by a complex oxide were calculated from the relative intensities of corresponding sextets. In the case of spinel ferrites, the degree of inversion, λ, characterizing the distribution of cations over the two nonequivalent cation sublattices (tetrahedral (A) and octahedral [B]) of the spinel structure was calculated from the Mössbauer subspectral intensities ($I_{(A)}/I_{[B]} = f_{(A)}/f_{[B]} \times \lambda/(2-\lambda)$), assuming that the ratio of the recoilless fractions is $f_{[B]}/f_{(A)} = 1$ at low temperatures [35]. The average canting angle, Ψ, was calculated from the ratio of the intensities of lines 2 and 1, I_2/I_1, according to $\Psi = \arcsin\{[3(I_2/I_1)/2]/[1+3(I_2/I_1)/4]\}^{1/2}$ [36].

^{119}Sn Mössbauer spectroscopic measurements were performed in transmission geometry at 293 K in the Mössbauer Laboratory of the Solid State Chemistry Group in Braunschweig. ^{119}Sn in a $CaSnO_3$ matrix was used as γ-ray source.

X-ray powder diffraction (XRD) measurements were carried out in the XRD Laboratory of the Solid State Chemistry Group in Braunschweig. XRD patterns were collected using a PW 1820 powder diffractometer (Philips, Netherlands) with Cu Kα radiation, see Fig. 2.5.

Fig. 2.5. X-ray powder diffractometer used in this work for XRD measurements.

In order to get refined information on the crystal structure of the studied materials, their X-ray powder diffraction patterns were analyzed in detail using Rietveld refinement [37]. This method is a powerful tool for the extraction and refinement of structural information from powder diffraction patterns, quantitative phase analysis, and for obtaining microstructural characteristics such as crystallite size and microstrain. The refinement consists in minimizing the differences (residuals) between a calculated pattern based on a starting structure and the experimental diffraction pattern by adjusting iteratively the crystallographic and instrumental parameters affecting the intensity at each diffraction angle.

The Rietveld method was fully implemented in 1969 [38]. At this time, the method was mainly used to refine structures from data obtained by fixed wavelength neutron diffraction. It had been suggested that the method could also be applied to X-ray data, but it was not until 1977 [39] that the method became generally accepted for X-ray as well as neutron diffraction, first with fixed wavelength and then also with fixed angle (energy dispersive data). The method has been so successful that nowadays the structure of materials, in the form of powders, is routinely being determined nearly as accurately as the results obtained by single crystal diffraction techniques. The Rietveld method has contributed to a renewed interest in powder diffraction techniques, even to the extent that in some applications it replaces single crystal techniques. In the last 20 years, the Rietveld method has played a crucial role in almost every high profile area of materials research and it has been applied to a wide range of solids [40].

In the present work, the computer program '*PowderCell*' [41] was used for the least-squares structure refinement of the X-ray powder diffraction data of the investigated oxides. The microstructural characteristics (crystallite size and strains) were obtained from the analysis. The JCPDS PDF database [42] was utilized for phase identification using the STOE software. The goodness of the least-squares structure refinement was assessed by R_B, R_p and R_{wp} factors [43], which are the most significant indicators of the agreement between the crystal structure model [calculated intensities $I_i(cal.)$] and the actual structure [observed intensities $I_i(obs.)$]:

$$R_{\mathrm{B}} = \frac{\sum \left| I_{\mathrm{i}}(obs.) - I_{\mathrm{i}}(cal.) \right|}{\sum I_{\mathrm{i}}(obs.)}; \quad R_{\mathrm{p}} = \sqrt{\frac{\sum \left[I_{\mathrm{i}}(obs.) - I_{\mathrm{i}}(cal.) \right]^2}{\sum I_{\mathrm{i}}^2(obs.)}}; \quad R_{\mathrm{wp}} = \sqrt{\frac{\sum w_{\mathrm{i}} \left[I_{\mathrm{i}}(obs.) - I_{\mathrm{i}}(cal.) \right]^2}{\sum w_{\mathrm{i}} I_{\mathrm{i}}^2(obs.)}}.$$

were w_i is the weight assigned to the intensity observation at the *i*th step, and is usually based only on counting statistics.

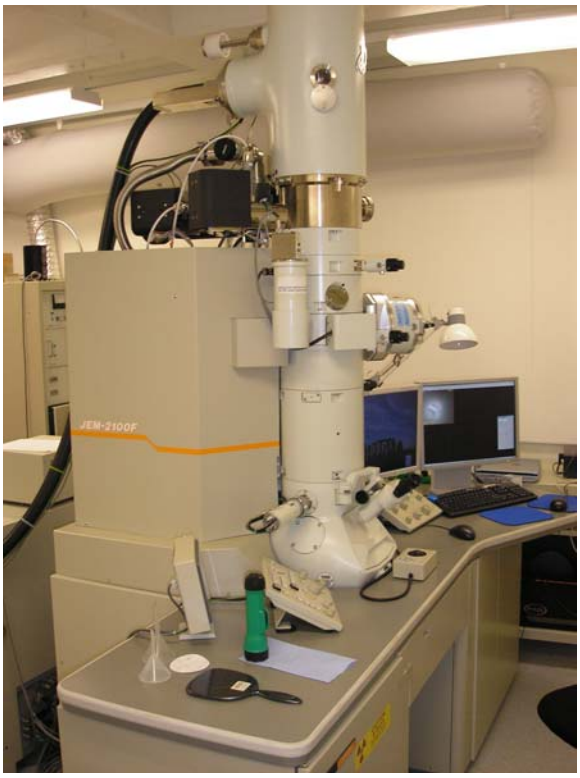

Fig. 2.6. (Scanning) transmission electron microscope used in this work.

The morphology of the investigated oxides and the sizes of individual crystallites was studied using a combined *field-emission (scanning) transmission electron microscope* (S)TEM (JOEL JEM-2100F-UHR) with an ultrahigh-resolution pole piece that provides a point resolution better than 0.19 nm at 200 kV. (S)TEM investigations were performed at the Institute of Physical Chemistry and Electrochemistry of the Leibniz University Hannover in cooperation with Dr. A. Feldhoff. Figure 2.6 shows the (scanning) transmission electron microscope employed in this work.

Prior to TEM investigations, powders were crushed in a mortar, dispersed in ethanol, and fixed on a copper-supported carbon film. The (S)TEM method in combination with the high angle annular dark field (HAADF) technique, selected area electron diffraction (SAED), and energy-dispersive X-ray spectroscopy (EDXS) was used to obtain additional information on the local chemistry and the structure of the investigated materials.

Fig. 2.7. Superconducting quantum interference device (SQUID magnetometer) used in this work.

Magnetic measurements were made using a superconducting quantum interference device (SQUID magnetometer), that allow to measure extremely small magnetic fields. This magnetometer requires cooling with liquid helium (4.2 K) or liquid nitrogen (77 K) to operate. Hence the packaging requirements are rather stringent both from a thermal-mechanical as well as magnetic standpoint. SQUID investigations were performed at the Institute of Condensed Matter Physics of Braunschweig University of Technology in cooperation with Dr. D. Menzel. Figure 2.7 shows the SQUID employed in this work.

The *field-dependent magnetization measurements* (hysteresis loops) were performed at liquid helium temperatures up to H_{ext} = 5 T. Moreover, the *temperature-dependent magnetization curves* of the investigated materials were also measured. Néel temperatures were determined using a Faraday balance equipped with a permanent magnet (0.004 T).

2.4 Magnetic Properties of Oxides

In this Section a short description of the most important magnetic effects in nanocrystalline ferrites is given, and the influence of these effects on Mössbauer spectra is discussed.

Magnetic ordering mechanisms in oxides result mostly in antiparallel spin arrangements. Spinel compounds were the first examples of Néel's theory of *ferrimagnetism*, in which the magnetic behavior of two sublattice systems with *unequal and antiparallel magnetic moments* is described [44]. Direct evidence of antiparallel spin alignment in spinel ferrites was first obtained by neutron diffraction [45]. With increasing temperature, spinel ferrites undergo a transition from an ordered ferrimagnetic state for $T < T_N$, to a disordered, paramagnetic state at $T > T_N$. Thermodynamically, this is a second-order transition. The transition temperature, T_N, in ferrites is known as *Néel temperature*.

Due to the relatively large distances between the cations the magnetic interactions are mainly of the indirect-exchange type, i.e., the anion acts as an intermediary. An essentially qualitative model for this indirect interaction, also referred to as *superexchange*, is as follows [46]. Consider two transition-metal cations separated by an O^{2-}, Fig. 2.8. The O^{2-} has no net magnetic moment since it has completely filled shells, with *p*-type outermost orbitals. Orbital p_x has two electrons: one with spin up, and the other with spin down, consistent with Pauli's principle. When one of the cations is brought close to the O^{2-}, partial electron overlap (between a 3*d* electron of the cation and a 2*p* electron of the O^{2-}) can occur only for antiparallel spins, because electrons with the same spin are repelled. Empty 3*d* states in the cation are available for partial occupation by the O^{2-} electron, with an antiparallel orientation. Electron overlap between the other cation and the O^{2-} then occurs resulting in antiparallel spins and therefore antiparallel order between the cations. A general, semiempirical approach has been discussed by Anderson [47].

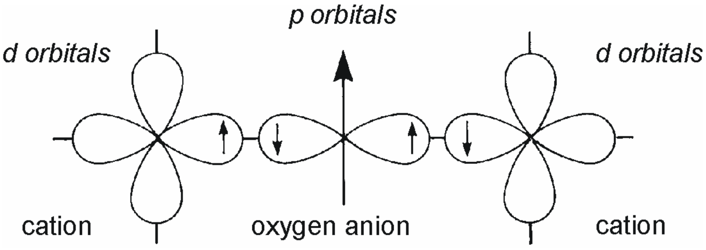

Fig. 2.8. Schematic representation of the superexchange interaction in magnetic oxides. After R. Valenzuela, *Magnetic Ceramics*. Cambridge University Press, Cambridge, 1994; [46].

The peculiar magnetic properties of ultrafine ferrite particles have been of particular interest for a long time, see e.g., [48]. Comprehensive reviews of the basic magnetic properties of nanoscale oxides particles have been published elsewhere [49-53].

The magnetic anisotropy energy of magnetically ordered particle/crystallite, E, as a measure of the energy required to rotate the magnetization direction, is proportional to the particle/crystallite volume, V, and is also a function of anisotropy energy constant, K:

$$E(\theta) = KV \sin^2\theta,$$

where θ is the angle between the magnetization vector and the easy direction of magnetization [49]. In nanoscale crystallites the energy barrier, KV, which separates the two energy minima at $\theta = 0°$ and $\theta = 180°$, may be comparable to the thermal energy (kT). Consequently, there is a finite probability that magnetization vector is not oriented along one of the easy directions but fluctuates betweeng the energy minima with a *relaxation time* τ. Thus, the magnetic moments of nanoparticles undergo, above a certain temperature, spontaneous thermal fluctuations, analogous to the behavior of paramagnetic atoms, and exhibit a so-called *superparamagnetic behavior* [49].

Because of its great sensitivity to magnetic fluctuations, Mössbauer spectroscopy was found to be a suitable technique for the detection of superparamagnetism. Such magnetic fluctuations can, however, complicate the analysis of spectra by a collapse of the magnetic hyperfine field far below the Néel temperature and give rise to relaxation line broadening or - even down to very low temperatures - to unresolved hyperfine field distributions. The first observation by Mössbauer spectroscopy of superparamagnetism in spinel ferrites was reported by Schuele *et al.* [54] in 10-20 nm $CoFe_2O_4$ and 3-20 nm $NiFe_2O_4$ ultrafine particles. A collapse of the magnetic hyperfine field far below the Néel temperature was observed which could be interpreted as motional narrowing due to the onset of superparamagnetism. Eibschütz and Shtrikman [55] demonstrated that this motional narrowing can partly be restored by application of an external magnetic field, suggesting the polarization of the particles by the field.

It is well known that the influence of the superparamagnetic relaxation on Mössbauer spectra depends on the relaxation time τ compared to the time scale of Mössbauer spectroscopy, which is approximately given by the Larmor precession time τ_L of the nuclear magnetic moment in the magnetic hyperfine field. In ^{57}Fe Mössbauer spectroscopy, τ_L is normally of the order of 10^{-8}-10^{-9} s. The relaxation time for the reversal of magnetization in a particle is given by the expression:

$$\tau(V,T) = \tau_0 \exp(KV/kT),$$

where τ_0 is typically of the order of 10^{-10}-10^{-12} s [56].

In the Mössbauer spectrum, a material can be observed as superparamagnetic if the relaxation time τ is smaller than the Larmor precession time τ_L of the nuclear magnetic moment. On the other hand, for $\tau > \tau_L$ a magnetically split Mössbauer spectrum is observed. In an assembly of particles/crystallites with different volumes (nonuniformity of particle/crystallite sizes), the experimental Mössbauer spectra will be given by the superposition of spectra with different relaxation times, since τ is sensitive to the volume and K anisotropy density energy. Thus, the components in the spectra of mechanically activated oxides (e.g. ferrites) can be understood to arise from ^{57}Fe in crystallites with relaxation times $\tau < \tau_L$ (leading to a simple doublet pattern due to electric quadrupolar interaction in the superparamagnetic state) and $\tau > \tau_L$ (broadened sextets).

Since the relaxation time characterizing the superparamagnetic phenomenon is also a function of temperature [56, 57, 58], the influence of superparamagnetic relaxation can be counteracted by reducing the sample temperature. The superparamagnetic blocking temperature T_B is defined as the temperature below which the superparamagnetic relaxation is slow compared to the time scale of the experimental technique used for the study of the magnetic properties of small particles (i.e., about 10^{-8}-10^{-9} s for ^{57}Fe Mössbauer spectroscopy). In practice, a nanoscale milled sample always exhibits a crystallite size distribution. At given temperature, some crystallites may therefore be below their blocking temperature, whereas other may be above T_B, i.e., a distribution of blocking temperatures is present in the milled system. Consequently, the complex Mössbauer spectra of nanosized mechanically treated spinel ferrites consist of a superposition of a superparamagnetic doublet and several broadened sextets over a wide temperature range [60, 61, 59]. As the temperature is decreased, there is a gradual replacement of the superparamagnetic doublet component by a magnetically split component.

Average magnetic hyperfine fields in nanoscale ferrites are reduced and diminish much faster with increasing temperature than expected from the magnetization behavior of the bulk, the latter varying rather slowly below T_B because the Néel temperatures in spinel ferrites are generally much higher than T_B. In order to explain these phenomena, it should be noted that in the vicinity of T_B, the Mössbauer spectra of nanocrystalline ferrites may still be affected by fluctuations of the magnetization vector in directions close to an easy direction of magnetization. These fluctuations, the so-called *collective magnetic excitations* (CME), lead to a reduction of the magnetic hyperfine field [62]. For a nanoparticle with a magnetic energy $E(\Psi) = KV \sin^2 \Psi$, the observed hyperfine field is thus given by [63]:

$$H_{\text{obs}}(V,T) = H(V{=}\infty,T)\langle\cos\psi\rangle,$$

where H($V{=}\infty,T$) is the saturation hyperfine field, that is, the hyperfine field in the absence of fluctuations. For $kT/KV << 1$, one may use the approximation [64]:

$$\langle\cos\psi\rangle \cong 1-\tfrac{1}{2}(kT/KV).$$

Thus, the spectra of nanoscale material just below T_B are governed by a linear relationship between the average magnetic hyperfine field and temperature:

$$H_{\text{obs}}(V,T) = H(V{=}\infty,T)[1-\tfrac{1}{2}(kT/KV)].$$

The maximum reduction in the magnetic hyperfine field due to collective magnetic excitations is of the order of 5-15% (in the vicinity of T_B) [49]. A decrease in the temperature (well below T_B) leads to the suppression of the CME, i.e., the degree of hyperfine field reduction due to CME should approach zero at low temperatures.

^{57}Fe Mössbauer spectroscopy offers a unique possibility to study the approach to magnetic saturation of iron-containing materials [36]. The relative intensities of second (I_2) and fifth (I_5) lines in magnetically split six-line spectra depend on the angle between the magnetic hyperfine field and the gamma ray direction [64]. Thus, by applying an external magnetic field with sufficient strength one can study the degree of alignment of the spins along the field direction. The ratio of the areas of lines 2 and 5, $I_{2,5}$, and the lines 1 and of 6, $I_{1,6}$, is given by [65]:

$$I_{2,5}/I_{1,6} = \frac{4\sin^2\psi}{3(1+\cos^2\psi)},$$

where Ψ is the angle between the magnetic hyperfine field and the gamma ray direction. When the spins are collinear in an external magnetic field applied perpendicular to the direction of the Mössbauer radiation (Ψ = 90°), the ratio $I_{2,5}/I_{1,6}$ is 4/3. On the other hand, when the aligned moments are composed of canted local spin moments, the directions of the magnetic hyperfine fields are no longer parallel to the external field and both I_2 and I_5 will change. From the area ratio of these lines relative to the first (or last) line, $I_{2,5}/I_{1,6}$, the *canting angle* Ψ can be calculated according to [65]:

$$\psi = \arcsin\left[\frac{\frac{3}{2}(I_{2,5}/I_{1,6})}{1+\frac{3}{4}(I_{2,5}/I_{1,6})}\right]^{1/2} .$$

3 Homogeneous Mechanochemical Reactions

This Chapter deals with the crystal structure refinement of the *M*-type hexaferrites $BaFe_{12}O_{19}$ and $SrFe_{12}O_{19}$, their structural response to the mechanochemical processing as well as with their particle size-dependent magnetic properties. These ferrites have been intensively investigated as materials for permanent magnets, high-density recording magnetic, magnetooptic media, and microwave devices. For these applications, a high saturation magnetization, a suitable coercivity, and low-temperature synthesis for ultrafine particle sizes are desired. The following Sections provide evidence for the fact that the highly nonequilibrium nature of the mechanochemical processing creates an opportunity to prepare nanoscale hexaferrites with improved and/or novel physical properties.

3.1 Crystal Structure Refinement of Bulk $BaFe_{12}O_{19}$ and $SrFe_{12}O_{19}$ Hexaferrites: XRD and Mössbauer Spectroscopic Studies

Although an enormous amount of research has been devoted to microcrystalline hexaferrites, there are still a number of problems to be addressed and eventually solved. The problem involved is, above all, the clear understanding of the crystal structure of hexaferrites that is often an invaluable initial step in understanding synthesis-structure-property relationships. In spite of a huge number of structural studies spanning many years [15-80] (and references therein), the number of precise structure refinements of hexaferrites appearing in the literature is surprisingly small [76-78]. Therefore, the literature data contain certain differences in the values of the main structural parameters (a, c) of hexaferrites [69,70,80]. Thus, in our opinion, a lot of published experimentally determined crystal parameters of hexaferrites can be considered as poorly characterized and may be in error, e.g., [79].

It is clear that prior to any interpretation of the structure and properties of a nanocrystalline hexaferrite prepared by homogeneous mechanochemical reactions, the atomic configuration of the bulk material (which serves as a reference material in our studies) has to be known. An effective way to do this is by means of diffraction techniques (using X-rays or neutrons) and of spectroscopic methods (e.g., Mössbauer spectroscopy, X-ray photoelectron spectroscopy, etc.). Application of sophisticated software for the evaluation of powder diffraction and of spectroscopic data opens new ways to get more precise (refined) information on the crystal structure of studied materials.

The aim of this Section is to outline by examples how both X-ray diffraction and Mössbauer spectroscopy can provide unique refined insight into the structure of bulk hexaferrites.

In order to get refined information on the crystal structure of $BaFe_{12}O_{19}$ and $SrFe_{12}O_{19}$, we analyzed in detail their XRD pattern using Rietveld refinement [37]. Figure 3.1 illustrates the profile fit and the difference patterns for these materials. As seen, the calculated pattern fits the observed one very well. All peaks can be indexed to the hexagonal magnetoplumbite structure with the space group $P6_3/mmc$. The Pseudo-Voigt function defined by Young and Wiles [43] was used for the representation of individual reflection profiles. The background was represented by a polynomial of degree 5. The refined parameters were: background parameters, 2Θ zero-point, lattice constants, profile half-width parameters (u, v, w), the mixing parameters of the Pseudo-Voigt function (N_A, N_B), asymmetry correction factor (P), occupation factors, atom coordinates (x, y, z), and isotropic thermal parameters.

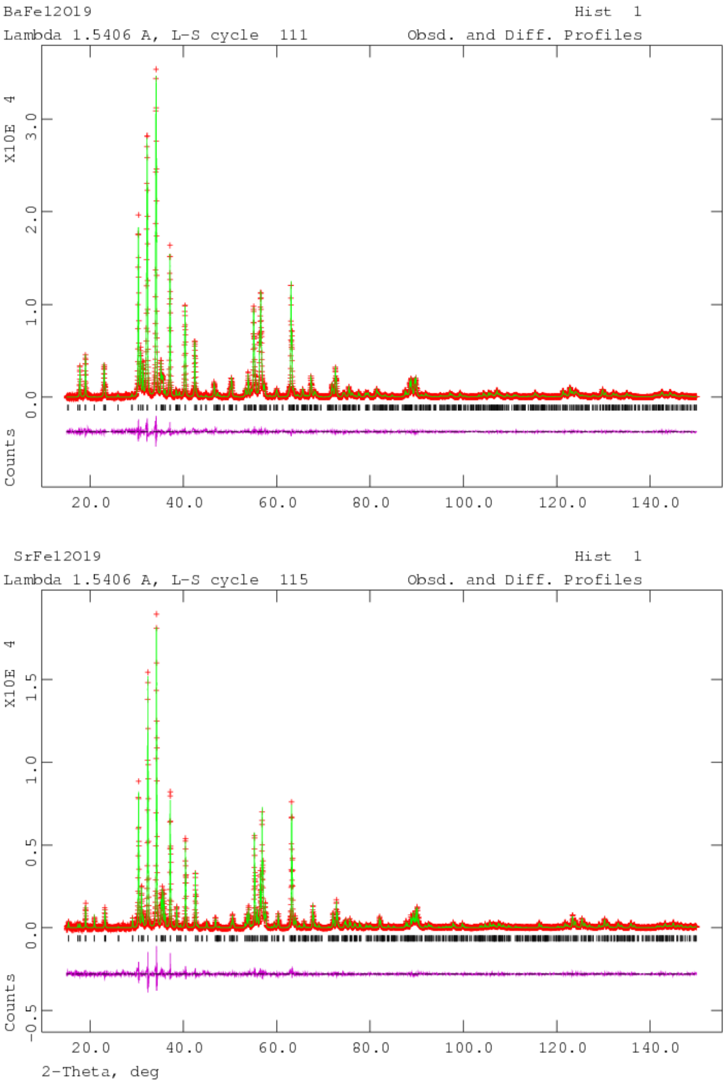

Figure 3.1. The output from the Rietveld refinement analysis of the XRD patterns for (top) $BaFe_{12}O_{19}$ and (bottom) $SrFe_{12}O_{19}$.

The Rietveld fits yield satisfactory crystal structure model indicators ($BaFe_{12}O_{19}$: R_B = 3.6, R_p = 5.2; $SrFe_{12}O_{19}$: R_B = 2.9, R_p = 4.5). The values of 5.1 ($BaFe_{12}O_{19}$) and 0.046 ($SrFe_{12}O_{19}$) obtained in the present study for the weighted R_{wp}-factors, which are very sensitive to the reflection profile functions used to describe the observed diffraction line profile, are very similar to data obtained for $SrFe_{12}O_{19}$ observed in Rietveld refinements of X-ray diffraction powder data [77]. Final results of the Rietveld refinements of $BaFe_{12}O_{19}$ and $SrFe_{12}O_{19}$ are listed in Table 3.1.

Table 3.1. Final results of the Rietveld refinement of $BaFe_{12}O_{19}$ and $SrFe_{12}O_{19}$ in space group $P6_3/mmc$; *x*, *y*, *z* - positional parameters, *g* - occupation factor.

Atom	**Wyck. letter**	***x***	***y***	***z***	***g***	**Atom**	**Wyck. letter**	***x***	***y***	***z***	***g***
$BaFe_{12}O_{19}$						**$SrFe_{12}O_{19}$**					
Ba	2d	0.33	0.66	0.25	0.938	Sr	2d	0.33	0.66	0.25	0.946
Fe1	2a	0.00	0.00	0.00	0.969	Fe1	2a	0.00	0.00	0.00	0.968
Fe2	2b	0.00	0.00	0.24	0.500	Fe2	2b	0.00	0.00	0.24	0.474
Fe3	$4f_1$	0.33	0.66	0.97	0.978	Fe3	$4f_1$	0.33	0.66	0.97	0.972
Fe4	$4f_2$	0.33	0.66	0.81	1.00	Fe4	$4f_2$	0.33	0.66	0.81	0.954
Fe5	12k	0.17	0.33	0.39	0.998	Fe5	12k	0.16	0.33	0.39	0.959
O1	4e	0.00	0.00	0.34	1.000	O1	4e	0.00	0.00	0.34	0.928
O2	4f	0.33	0.66	0.44	1.000	O2	4f	0.33	0.66	0.44	0.951
O3	6h	0.82	0.64	0.25	1.000	O3	6h	0.82	0.63	0.25	0.918
O4	12k	0.84	0.69	0.45	0.937	O4	12k	0.84	0.69	0.45	0.872
O5	12k	0.50	0.99	0.35	1.000	O5	12k	0.50	0.99	0.35	0.893

In addition to atom coordinates and occupation factors also unit cell dimensions of $BaFe_{12}O_{19}$ and $SrFe_{12}O_{19}$ were refined to be $a = b = 5.892(5)$ Å, $c = 23.202(1)$ Å and $a = b = 5.882(4)$ Å, $c = 23.046(7)$ Å, respectively.

The refined final set of atomic coordinates (Table 3.1) may be used to calculate the geometry of the magnetoplumbite structure of ferrites. Table 3.2 gives bond lengths and bond angles for both compounds.

Table 3.2. Bond lengths and bond angles obtained from Rietveld refinement of $BaFe_{12}O_{19}$ and $SrFe_{12}O_{19}$.

Type	**Bond length (Å) or Bond angle (deg)**	**Type**	**Bond length (Å) or Bond angle (deg)**
$BaFe_{12}O_{19}$		**$SrFe_{12}O_{19}$**	
Ba-O	2.9489(4)	Sr-O	2.9454(4)
Ba-Fe2	3.4090(5)	Sr-Fe2	3.40205(35)
Ba-Fe5	3.6958(16)	Sr-Fe5	3.6528(13)
Fe1-O4	1.975(6)	Fe1-O4	1.980(4)
Fe2-O1	2.419(13)	Fe2-O1	2.391(10)
Fe2-O3	1.845(9)	Fe2-O3	1.871(6)
Fe3-O2	1.925(9)	Fe3-O2	1.879(6)
Fe3-O4	1.923(6)	Fe3-O4	1.919(4)
Fe4-O3	2.095(7)	Fe4-O3	2.064(5)
Fe4-O5	1.963(6)	Fe4-O5	1.953(6)
Fe5-O1	2.021(6)	Fe5-O1	2.007(4)
Fe5-O2	2.089(5)	Fe5-O2	2.108(4)
Fe5-O4	2.101(4)	Fe5-O4	2.1029(28)
Fe5-O5	1.942(4)	Fe5-O5	1.9365(34)
Fe4-Fe4	2.776(6)	Fe4-Fe4	2.759(4)
Fe5-Fe5	2.934(4)	Fe5-Fe5	2.9164(28)
Fe4-O5-Fe5	127.61(19)	Fe2-Fe2	127.05(18)
Fe5-O5-Fe5	98.13(30)	Fe2-Fe5	97.70(24)
Fe2-O1-Fe5	122.31(25)	Fe2-O1-Fe5	121.43(19)
Fe3-O2-Fe5	125.79(19)	Fe3-O2-Fe5	126.95(14)
Fe5-O1-Fe5	94.10(34)	Fe5-O1-Fe5	95.29(25)
Fe5-O4-Fe5	89.48(23)	Fe5-O4-Fe5	89.70(17)

The importance of *local structure* on the physical properties of materials is evident. As Mössbauer spectroscopy [81] makes observations on a *local scale*, and not on a spaceaveraged scale it often can provide crucial information needed for a clear understanding of local structural features and of the behavior of a solid on a macroscopic scale. The continuous improvement of computation capabilities for spectral analyses, and the introduction of sophisticated software for the treatment of Mössbauer data has enabled researchers to obtain rich and valuable information available from the Mössbauer experiments as well as to study the structure of materials with higher accuracy and from complementary points of view.

Since the properties of a hexaferrite are to a large extent determined by its distribution of cations among available lattice sites, it is clear that prior to any interpretation of the properties of a ferrite, the ionic configuration must be well established. Due to its local sensitivity, Mössbauer spectroscopy has found wide use in the solution of this crystallographic problem.

The room-temperature Mössbauer spectra of $BaFe_{12}O_{19}$ and $SrFe_{12}O_{19}$ (Fig. 3.2) can well be fitted by a superposition of five magnetically split components (sextets). Based on the values of isomer shifts of the spectral components, it can be stated that no ferrous (Fe^{2+}) ion is present in the as-prepared materials [82]. Sextets with IS > 0.19 mm/s correspond to octahedrally coordinated ferric (Fe^{3+}) ions in the $4f_2$, 12k and 2a positions of hexaferrites, respectively [83]. The spectral component with the lowest value of IS (0.13-0.14 mm/s) is typical for Fe^{3+} cations in tetrahedral ($4f_1$) coordination [82]. The sextet with a relatively large quadrupole splitting (QS ~ 1.1 mm/s), indicating the presence of a large electric field gradient acting on iron nuclei, corresponds to Fe^{3+} ions in the trigonal bi-pyramidal (2b) sites of $BaFe_{12}O_{19}$ [83]. The Mössbauer parameters resulting from the least-squares fitting of the spectra of as-prepared $BaFe_{12}O_{19}$ and $SrFe_{12}O_{19}$ are given in Table 3.3. From the relative intensities of sextets, the number of iron cations located on $4f_2$, 12k, 2a, $4f_1$ and 2b sublattices was calculated to be 2, 6, 1, 2 and 1 (per formula unit of hexaferrites), respectively. A structural representation of hexaferrites together with the five different Fe nearest-neighbour configurations is shown in Fig. 3.3.

Thus, on the basis of Rietveld analysis the exact coordinates of atoms, the unit cell dimensions as well as the interatomic distances and angles in $BaFe_{12}O_{19}$ and $SrFe_{12}O_{19}$ were determined. The intrinsic high resolution of Mössbauer spectroscopy provided a high quality analytical tool for the characterization of both phases, and for the delineation of detailed aspects of the local atomic environment including quantitative information on hyperfine parameters.

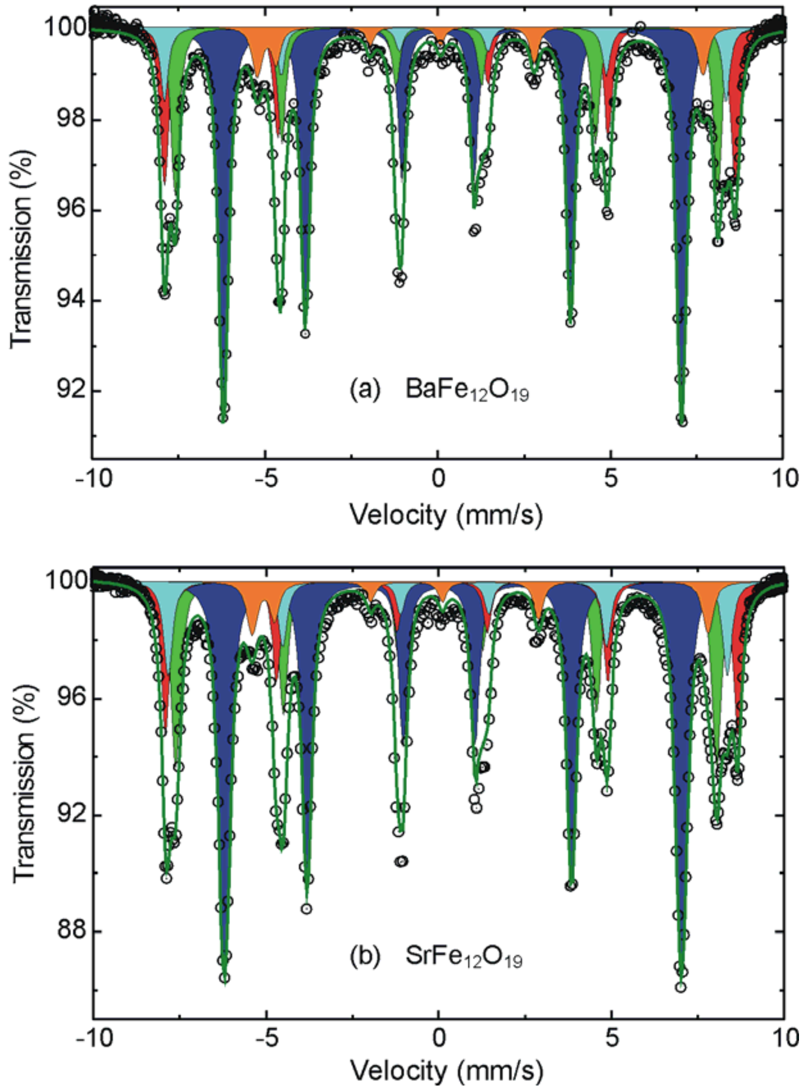

Figure 3.2. Room-temperature Mössbauer spectra of (a) $BaFe_{12}O_{19}$ and (b) $SrFe_{12}O_{19}$. Blue, green, red, light blue, and orange colors denote subspectra corresponding to Fe^{3+} cations in 12k, $4f_1$, $4f_2$, 2a, and 2b sites, respectively.

Table 3.3. Hyperfine parameters (IS – isomer shift, QS – quadrupole splitting, H – magnetic hyperfine field) obtained by fitting the room-temperature Mössbauer spectra of $BaFe_{12}O_{19}$ and $SrFe_{12}O_{19}$.

Site	**Coordination of Fe^{3+} ions**	**IS (mm/s)**	**QS (mm/s)**	***H* (T)**	**Number of Fe^{3+}/f.u.**
		$BaFe_{12}O_{19}$			
$4f_2$	octahedral	0.252(7)	0.102(8)	51.21(8)	2
12k	octahedral	0.218(1)	0.210(1)	41.10(1)	6
2a	octahedral	0.196(2)	0.022(2)	50.40(2)	1
$4f_1$	tetrahedral	0.139(4)	0.111(3)	48.66(3)	2
2b	bi-pyramidal	0.142(1)	1.083(1)	39.99(9)	1
		$SrFe_{12}O_{19}$			
$4f_2$	octahedral	0.238(3)	0.136(4)	51.35(3)	2
12k	octahedral	0.215(1)	0.198(1)	40.99(7)	6
2a	octahedral	0.218(6)	0.045(6)	50.19(5)	1
$4f_1$	tetrahedral	0.129(2)	0.092(2)	48.53(2)	2
2b	bi-pyramidal	0.134(9)	1.063(8)	40.88(6)	1

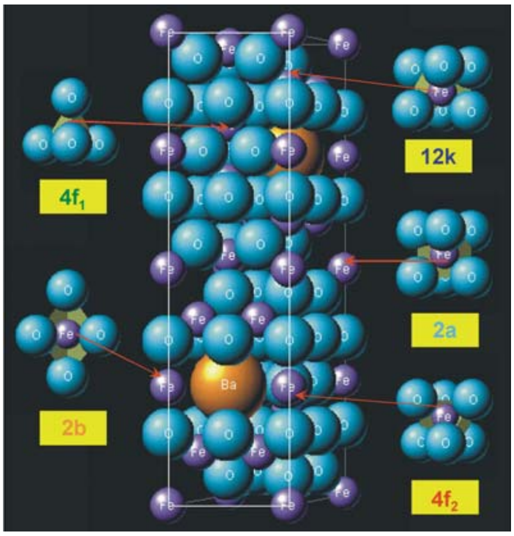

Figure 3.3. The crystal structure of hexagonal *M*-type ferrite and the five Fe sites with their surroundings.

3.2 Mechanical Activation of $BaFe_{12}O_{19}$ and $SrFe_{12}O_{19}$ Hexaferrites

The influence of mechanical activation on structural features of solids is assessed in a number of published papers in terms of changes in integral quantities such as crystallite size, microstrains, specific surface area, etc. Although these quantities are considered as not sufficient to describe mechanically induced disordering, they remain to be a part of the complex description of any particular system.

Figures 3.4 (a) and (b) show the morphology of the as-prepared $BaFe_{12}O_{19}$ powder. The particles of the co-precipitated ferrite were found to be uniform in shape; the majority of them are hexagonal platelet crystals. Whereas the thickness of the ferrite platelets is in the 20-100 nm range, their length ranges from 300 to 400 nm. The corresponding selected area electron diffraction (SAED) pattern of the ferrite is dominated by discrete diffraction spots originating from the well crystalline hexagonal platelets, see Fig. 3.4 (c), were each spot corresponds to a satisfied diffraction condition of the sample's crystal structure.

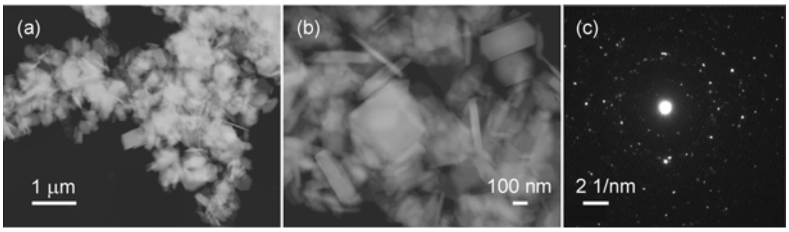

Figure 3.4. Electron microscopy images (a, b) and the corresponding SAED pattern (c) illustrating the presence of hexagonal platelet crystals in the co-precipitated $BaFe_{12}O_{19}$.

The disintegration of ferrite particles by mechanical treatment is accompanied by an increase in the number of particles and by generation of fresh, previously unexposed, surfaces. The milling of the hexaferrite decreases the thermodynamic stability of the material by increasing the number of extended imperfections, such as dislocations and interfaces.

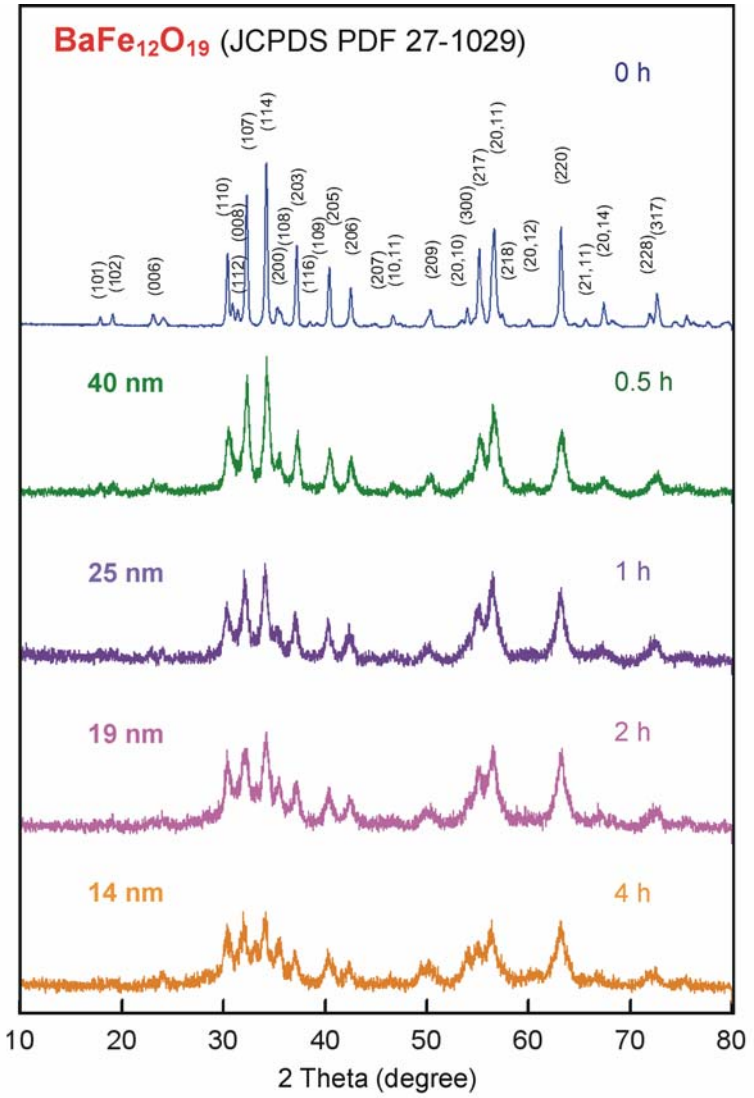

Figure 3.5. XRD patterns of $BaFe_{12}O_{19}$ milled for various milling times. Diffraction peaks of the bulk $BaFe_{12}O_{19}$ are denoted by Miller indices. The milling times and corresponding crystallite sizes are shown in the figure.

Powder particles mechanically activated for a prolonged period consist of small *crystallites* separated by high-energy *grain boundaries* in which the atomic arrangement may lack any long- or short-range order [84]. Due to the accumulation of structure imperfections with prolongation of the mechanical treatment, the well-known phenomena of diffraction line broadening and of redistribution of diffraction line intensities are observed in the XRD patterns of milled ferrites. Figure 3.5 shows the XRD patterns of $BaFe_{12}O_{19}$ milled for various times.

The average crystallite size of nanostructured materials can be evaluated by the analysis of the angle-dependent broadening of XRD lines [85]. Usually, a characteristic monotonous decrease of the crystallite size, D, with time of the mechanical treatment, t_m, of hexaferrites is observed. The crystallite size of hexaferrites is typically reduced to about 10 nm, as it is shown for $BaFe_{12}O_{19}$ in Fig. 3.6.

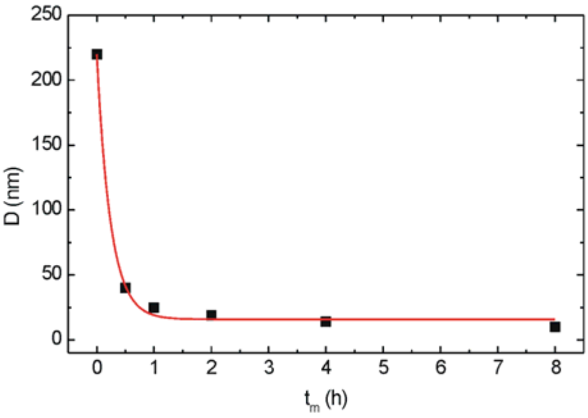

Figure 3.6. Crystallite size (D) of $BaFe_{12}O_{19}$ as a function of milling time (t_m).

The crystallite size, obtained from the XRD line broadening analysis, was checked by transmission electron microscopy. Representative TEM micrographs of mechanically activated hexaferrites are shown in Figure 3.7. They reveal that the milled ferrites consist of crystallites with sizes of about 10 nm which is consistent with the average crystallite size determined by XRD. As shown in Figure 3.7, nanoscale crystallites tend to agglomerate. From the comparison of the morphology of the initial (bulk) and mechanically activated materials (compare Figs. 3.4 and 3.7) it is clear that hexagonal platelets were comminuted into spherical crystallites.

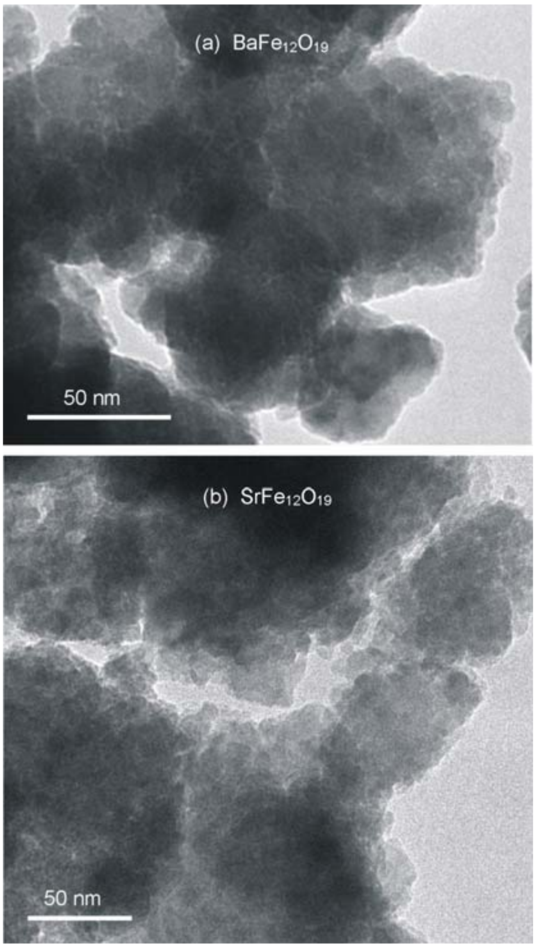

Figure 3.7. TEM images of (a) $BaFe_{12}O_{19}$ and (b) $SrFe_{12}O_{19}$ mechanically activated for $t_m = 4$ h.

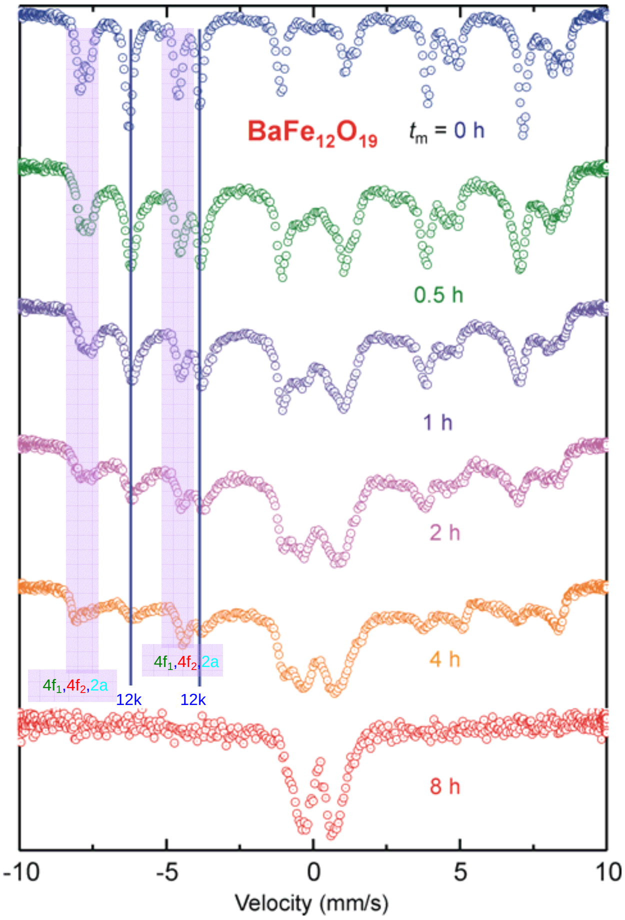

Figure 3.8. Room-temperature ^{57}Fe Mössbauer spectra of $BaFe_{12}O_{19}$ milled for various times. The positions of $4f_1$, $4f_2$, 2a and 12k are indicated by pink and blue, respectively (see Fig. 3.2 (a)). The milling times are shown in the figure.

To determine the nature of the mechanically induced structural disordering in $BaFe_{12}O_{19}$ and $SrFe_{12}O_{19}$ on the local atomic scale, we performed room-temperature ^{57}Fe Mössbauer measurements. It is observed that, with increasing milling time of hexaferrites, the sextets corresponding to Fe^{3+} ions located on the five sublattices become asymmetric towards the inside of each line. This is the only effect of the milling on the Mössbauer spectra of $SrFe_{12}O_{19}$ (see below). In the case of $BaFe_{12}O_{19}$, the prolonged milling additionally leads to the collapse of the broadened sextets, which are gradually replaced by a broad central doublet with isomer shift characteristic of Fe^{3+} ions [82], see Fig. 3.8.

An important result derived from the present Mössbauer measurements is that mechanical activation is accompanied by changes in the relative intensities of the subspectra (Fig. 3.6). It is clearly visible that the relative intensity of the 12k subspectrum (I_{12k}) decreases with increasing milling time. For the bulk $BaFe_{12}O_{19}$, the intensity ratio $I_{12k}/(I_{4f1} + I_{4f2} + I_{2a})$ is 6/5, whereas it takes a value of about 3/5 for the material milled for 4 h. This structural variation has important implications for macroscopic magnetic properties of hexaferrite, and it has to be taken into consideration to account for the magnetic behavior of nanostructured hexaferrite particles (see Section 3.3).

To elucidate the origin of the central doublet in the room-temperature spectra, it should be recalled that the high-energy milling of $BaFe_{12}O_{19}$ is accompanied by the reduction of the crystallite size to the nanometer range (~ 10 nm), see Fig. 3.7. Thus, the crystallite sizes in the milled ferrite are so small that thermally induced energy fluctuations (k_BT) can overcome the magnetic anisotropy energy (KV) and change the direction of the magnetization of a particle from one easy axis to another, i.e., *superparamagnetic relaxation* occures.

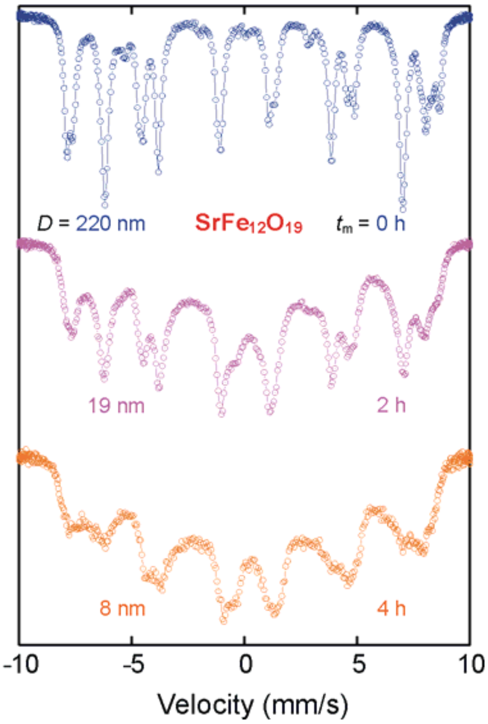

Figure 3.9. Room-temperature ^{57}Fe Mössbauer spectra of $SrFe_{12}O_{19}$ milled for various milling times. The milling times and corresponding crystallite sizes are also shown in the figure.

The presence of only broadened sextets in the Mössbauer spectra of $SrFe_{12}O_{19}$ (see Fig. 3.9) reflects longer relaxation times τ of $SrFe_{12}O_{19}$ crystallites in comparison with those of $BaFe_{12}O_{19}$. Taking into account the similar volumes of crystallites (V) in both milled $BaFe_{12}O_{19}$ and $SrFe_{12}O_{19}$, the absence of the central superparamagnetic doublet in the spectrum of the milled $SrFe_{12}O_{19}$ indicates a different value for the magnetic anisotropy constants (K) in the materials. From the equation given above, it is clear that a longer relaxation time τ implies a lower K value. Thus, from the Mössbauer measurements of the mechanically activated hexaferrites it can be concluded that $SrFe_{12}O_{19}$ possesses the lower value of the magnetic anisotropy constant in comparison with that of $BaFe_{12}O_{19}$. The exact K values for both studied ferrites will be calculated in the following Section.

3.3 Particle Size-Dependent Magnetic Properties of $BaFe_{12}O_{19}$ and $SrFe_{12}O_{19}$ Hexaferrites

It is well recognized that at the nanoscale the fundamental properties of materials depend on their size and shape [86]. Size-dependent properties are the reason for nanoscale objects having the potential to significantly impact both science and industry. Examples of size-dependent properties include, for example, catalytic properties, electrochemical properties, melting point, magnetic properties, optical properties [87]. It is difficult to predict below which size a particular material will exhibit size-dependent properties. This threshold is different for each material and each property. For example, nanoscale gold will have different colours throughout the nanoscale size range, but the size-dependent catalytic properties do not dramatically change until sizes becomes smaller than five nanometers [87].

In this Section, the particle size-dependent magnetic properties of $BaFe_{12}O_{19}$ and $SrFe_{12}O_{19}$ hexaferrites prepared by homogeneous mechanochemical reactions are presented. In addition to the already mentioned relaxation effects of *superparamagnetism*, several interesting features dealing with the magnetism of ferrimagnetic nanoparticles are encountered in the Section, e.g., *reduced saturation magnetization*, *enhanced or reduced coercivity*, and the *spin canting effect*.

Figure 3.10 compares the hysteresis loops measured at 5 K of bulk and mechanically activated $BaFe_{12}O_{19}$ and $SrFe_{12}O_{19}$. An interesting observation is that the saturation magnetization (M_s) decreases with increasing t_m (i.e., with decreasing D) for both $BaFe_{12}O_{19}$ and $SrFe_{12}O_{19}$. As can be seen, the magnetization of the nanoscale samples does not saturate even at the maximum field attainable ($H_{ext} = 5$ T). This is in contrast to the magnetic behavior of the bulk $BaFe_{12}O_{19}$ and $SrFe_{12}O_{19}$, whose M_s reach the values of 97.30 emu/g and 103.19 emu/g, respectively. By extrapolating the high-field region of the $M(1/H_{ext})$ curves to infinite field, we estimated the M_s values of hexaferrites with various particle sizes, see Fig. 3.10. The determined M_s values span a wide range; the minimum M_s values were found to be 37.52 emu/g and 48.55 emu/g for nanostructured $BaFe_{12}O_{19}$ ($D = 14$ nm) and $SrFe_{12}O_{19}$ ($D = 8$ nm), respectively. These values are about 61% and 53% lower than corresponding ones for bulk $BaFe_{12}O_{19}$ and $SrFe_{12}O_{19}$, respectively.

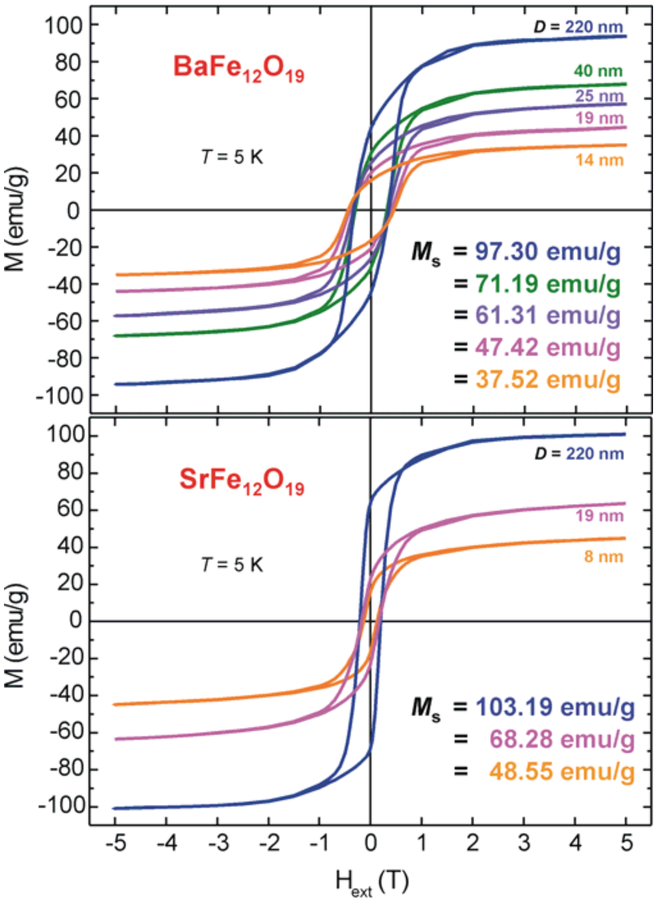

Figure 3.10. Magnetization hysteresis loops for bulk and nanoscale mechanically activated $BaFe_{12}O_{19}$ (top) and $SrFe_{12}O_{19}$ (bottom). Hysteresis loops were measured at 5 K after field cooling at $H_{ext} = 5$ T. The values of the saturation magnetizations and corresponding crystallite sizes are also shown in the figure. Commonly H stands for magnetic field strength (units of A/m). In case of our hysteresis plots we are using H_{ext} for the externally applied magnetic field (units of Tesla).

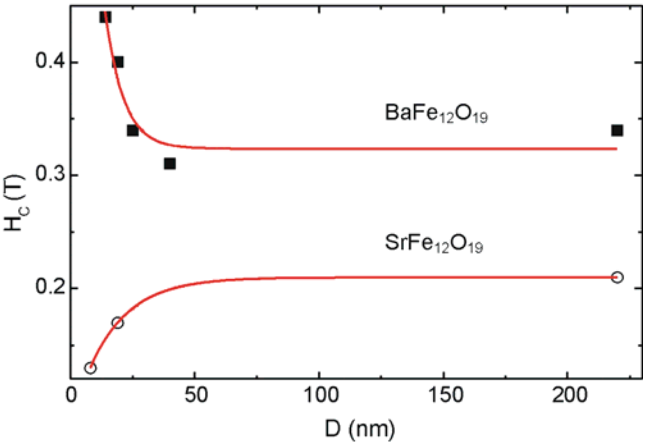

Figure 3.11. The coercive fields of $BaFe_{12}O_{19}$ and $SrFe_{12}O_{19}$ as function of the crystallite diameter.

It is also found that the nanoscale mechanically activated $BaFe_{12}O_{19}$ and $SrFe_{12}O_{19}$ hexaferrites exhibit enhanced and reduced magnetic hardness, respectively. In other words, starting from about $D = 50$ nm, the coercive field (H_C) of $BaFe_{12}O_{19}$ increases with decreasing particle size, whereas this physical quantity decreases with decreasing D for $SrFe_{12}O_{19}$, see Fig. 3.11. According to Refs.[69,88], the coercivity of nanoparticles in the frame work of the

Stoner-Wohlfarth theory is determined by the magnetocrystalline anisotropy constant K and the saturation magnetization M_s:

$H_\mathrm{C} = 2K/\mu_0 M_\mathrm{s}$,

where μ_0 is the permeability of free space, $4\pi \times 10^{-7}$ H/m. Thus, the magnetocrystalline anisotropy constant K can be calculated combining the results of H_C and M_s. The variation of M_s, H_C, and K with average crystallite size is given in Table 3.4.

Thus, the SQUID measurements reveal that the magnetic anisotropy constant of the bulk $SrFe_{12}O_{19}$ ($K = 1.711 \times 10^{-3}$) is lower than that of the $BaFe_{12}O_{19}$ sample ($K = 2.612 \times 10^{-3}$). This finding is in agreement with the result derived from Mössbauer measurements (see Section 3.2). Both, enhancement and reduction of the coercive field of $BaFe_{12}O_{19}$ and $SrFe_{12}O_{19}$, respectively, can be explained by a decrease of the magnetic anisotropy constant with decreasing particle size, see Fig. 3.12. This is in accordance with literature data emphasizing a strong dependence of K on the particle size [89]. Moreover, the anisotropy is also influenced by other effects such as particle shape. It was found, for example, that the corecivity of nanocubes is lower than that of nanospheres having the same volume [88]. It was explained by a larger value of anisotropy constant for spherical nanoparticles [86]. Since the cation distribution in nanostructured complex oxides is a function of the particle size [90], the altered K may also be attributed to the high volume of the grain boundaries with a nonequilibrium cation distribution and spin canting.

Table 3.4. Average crystallite size (D), saturation magnetization (M_s); coercivity (H_C), and magnetic anisotropy constant (K) derived from the hysteresis loops measured at 5 K for bulk and subsequently mechanically activated $BaFe_{12}O_{19}$ and $SrFe_{12}O_{19}$.

Sample	D (nm)	M_s (emu/g)	H_C (T)[a]	K (HA^2/kg)
$BaFe_{12}O_{19}$	220	97.30	0.34	2.612×10^{-3}
	40	71.19	0.31	1.742×10^{-3}
	25	61.31	0.34	1.646×10^{-3}
	19	47.42	0.40	1.498×10^{-3}
	14	37.52	0.44	1.303×10^{-3}
$SrFe_{12}O_{19}$	220	103.19	0.21	1.711×10^{-3}
	19	68.28	0.17	0.916×10^{-3}
	8	48.55	0.13	0.498×10^{-3}

[a] Values of the saturation magnetization were obtained by linear extrapolation of the high-field region ($H_\mathrm{ext} > 3.5$ T) of the $M(1/H_\mathrm{ext})$ curves to infinite field.

Some authors claim that K in hexaferrites depends on the occupation of the 12k positions by Fe^{3+} ions [91]. According to Ref. [91], the contribution of Fe^{3+} ions in the 12k positions to the anisotropy energy constant comprises more than one-half of the experimental K value. As shown in the previous Section 3.2 (see page 26), the mechanically induced particle size reduction of hexaferrites is accompanied by the decrease of the relative intensity of the 12k subspectrum. Thus, taking into account this result together with the theoretical findings reported in [91], the decrease of the magnetic anisotropy constant with decreasing D can mainly be explained by the lowering the occupation factor of Fe^{3+} ions in the 12k positions of $BaFe_{12}O_{19}$ and $SrFe_{12}O_{19}$ hexaferrites.

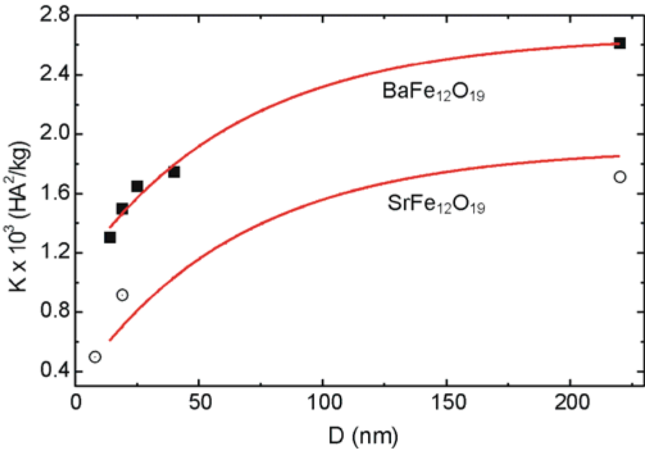

Figure 3.12. The dependence of the magnetic anisotropy constant of $BaFe_{12}O_{19}$ and $SrFe_{12}O_{19}$ on the crystallite diameter at 5K.

In addition to the coercive field, a particle size-dependent behavior is also observed for other parameters of the investigated hexaferrites such as the saturation magnetization (M_s) which is normally assumed to be a material constant, see Fig 3.10. The size-dependent character of M_s cannot be explained in a trivial way. Although several researchers have investigated the causes for the observed reduction in saturation magnetization with decreasing size of hexaferrite nanoparticles using a variety of techniques, the present knowledge which has been collected is not enough to provide a clear-cut mechanism for this phenomenon.

Although different hypotheses conflict and remain debatable, two generally accepted views on the size-dependent character of saturation magnetization can be found in the literature, namely effects of the so-called “dead” layer and of chemical instability of hexaferrite nanoparticles. In the former case, the “dead” layer (characterized by the magnetization $M = 0$) is caused by an asymmetric environment effect of the surface atoms, and it leads to a deterioration of magnetic properties of a material [92-96]. The origin of the magnetically inactive surface layers is associated with the change in spin configuration and/or crystal structure of the near-surface regions of nanoparticles. Kodama et al. [97,98] have proposed a core–shell exchange-coupled model of the spin distribution within nanoscale ferrite particles, where a ferrimagnetic core is surrounded by a surface layer of canted (noncollinear) spins due to broken exchange bonds. Recently, Šepelák et al. [99,100] have modified the core–shell model of ferrimagnetic nanoparticles. In this model, a competition between the effects of spin canting and site exchange of cations in the interface/surface shell of nanoparticles plays a decisive role. These authors have concluded that a reduction of magnetic moment is observed only in the case when the effect of spin canting in the shell dominates over the effect of cation disorder. Otherwise the unusual phenomenon of magnetization enhancement may be expected. Some authors attribute the reduction of magnetization of nanoparticles to their amorphous nature [101]. Another way to explain the degradation of magnetic properties of hexaferrites with decreasing particle size is via their chemical instability in the nanoscale state. In this case, the reduced saturation magnetization of a material is associated with the partial decomposition of the ferrite into simple oxides MeO (Me = Ba, Sr) and Fe_2O_3 (with lower M_s in comparison to that of ferrite). In this case, a linear dependence of the saturation magnetization on the particle size is expected [102].

The quantitative information on the decrease of the relative intensities of the 12k subspectrum, obtained from the analysis of Mössbauer spectra, is very helpful in the interpretation of the reduced magnetization of nanocrystalline hexaferrites. Because Ba^{2+} and Sr^{2+} ions possess no magnetic moment, the total magnetic moment μ in $BaFe_{12}O_{19}$ and $SrFe_{12}O_{19}$ is entirely due to the uncompensated magnetic moments of ferric ions. Thus, taking into account both the number of iron cations located on available cation sublattices, estimated from the relative intensities of the corresponding Mössbauer subspectra (see Table 3.3), as well as the orientation of spins in hexaferrites [77,103], we can calculate the effective magnetic moment (per formula unit) of $BaFe_{12}O_{19}$ and $SrFe_{12}O_{19}$. Assuming that 1 Fe^{3+} cation possesses the magnetic moment of 5 μ_B (μ_B is Bohr magneton, $\mu_B = 9.27408 \times 10^{-21}$ emu) and that the alignment of spins is collinear, the resulting magnetic moment for bulk $BaFe_{12}O_{19}$ and $SrFe_{12}O_{19}$ materials is calculated to be 20 μ_B/f.u. (see Table 3.5). The saturation magnetization per 1 gram of hexaferrite can be expressed as

$$M_s = N_A \mu / M,$$

where N_A is Avogadro's constant ($N_A = 6.02214 \times 10^{23}$ mol^{-1}), and M is the molar mass of the material ($M_{BaFe12O19} = 1111.5$ g/mol, $M_{SrFe12O19} = 1059.8$ g/mol). The calculated M_s values of 100.5 emu/g and 105.4 emu/g for $BaFe_{12}O_{19}$ and $SrFe_{12}O_{19}$, respectively, are in agreement with those from the SQUID measurements ($M_s = 97.30$ emu/g, $M_s = 103.19$ emu/g), see also Table 3.4. These values are in reasonable agreement with those previously reported for hexaferrites ($M_s = 99.1(2)$) emu/g [104].

Table 3.5. The calculated effective magnetic moment of bulk $BaFe_{12}O_{19}$ and $SrFe_{12}O_{19}$ materials.

Sublattice	**Coordination of Fe^{3+} ions**	**Number of Fe^{3+}/f.u.**	**Spin orientation**	**Magnetic moment per formula unit**
$4f_2$	octahedral	2	↓	$\mu = -2 \times 5\ \mu_B + 6 \times 5\ \mu_B + 1 \times 5\ \mu_B - 2 \times 5\ \mu_B + 1 \times 5\ \mu_B = = 4 \times 5\ \mu_B = = \mathbf{20\ \mu_B}$
12k	octahedral	6	↑	
2a	octahedral	1	↑	
$4f_1$	tetrahedral	2	↓	
2b	bi-pyramidal	1	↑	

As mentioned in Section 3.2, the mechanically induced particle size reduction of hexaferrites is accompanied by the decrease of the relative intensity of the 12k subspectrum from $I_{12k}/(I_{4f1} + I_{4f2} + I_{2a}) = 6/5$ to about 3/5 (for the material milled for 4 h). This variation can be explained by a decrease of the occupation factor of Fe^{3+} ions in the 12k positions. Similar spectral changes (redistribution of Mössbauer or NMR spectral intensities) have been observed, for example, in nanocrystalline spinels and explained in terms of the mechanically induced cation redistribution over the cation spinel sublattices of tetrahedral and octahedral coordination [60,105-108]. Taking into account that in the magnetoplumbite structure, all the regular sites are occupied by the cations, the decrease of the relative intensity of the 12k subspectrum can be associated with the transition of some of the Fe^{3+} cations from 12k sites into interstitial positions in the hexagonal structure.

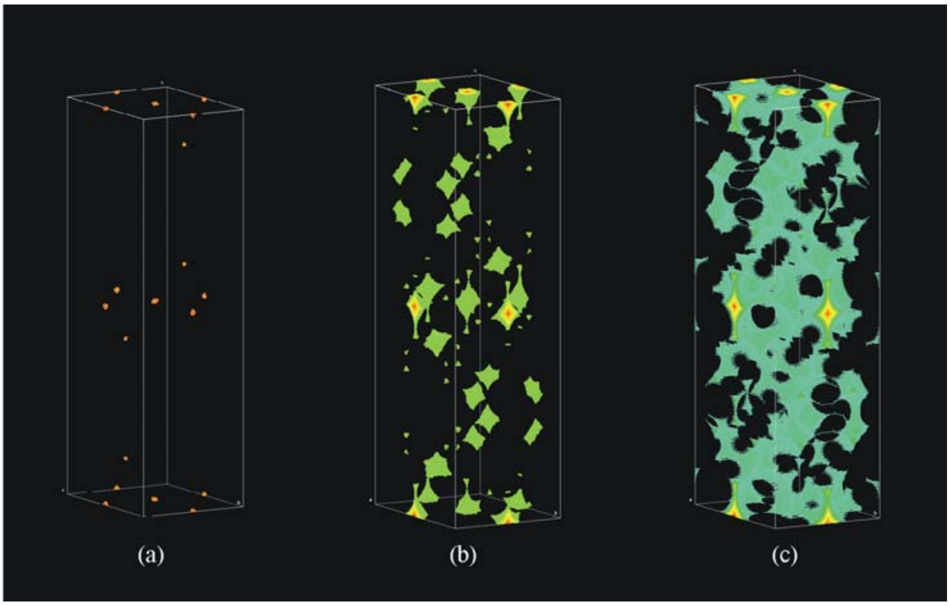

Figure 3.13. Visualization of interstitial spherical cavities (holes) with radii of (a) 0.8 Å, (b) 0.5 Å, and (c) 0.4 Å in the magnetoplumbite structure.

The JSV program [109] enables us to visualize interstitial spherical cavities (holes) with various radii in the magnetoplumbite structure, where the Fe^{3+} cations could be located. Figure 3.13 illustrates the cavities of various radii for $BaFe_{12}O_{19}$, assuming the crystal radii of O^{2-}, Fe^{3+}, and Ba^{2+} ions to be $r_O = 1.24$ Å, $r_{Fe} = 0.785$ Å, and $r_{Ba} = 1.56$ Å, respectively. The largest hole in the lattice was found to have a radius of $r = 0.881$ Å that is larger than the crystal radius of Fe^{3+} cations (0.785 Å). This provides evidence that, from the geometrical point of view, the above-mentioned structural transition of Fe^{3+} cations in the hexagonal lattice is generally possible, resulting in a nonequilibrium cation distribution. An interesting observation is that the interstitial holes form some ordered arrays, which can serve as possible diffusion paths in the structure of hexaferrites (see Fig. 3.13 (c)).

Taking into account the decrease of the relative intensity of the 12k subspectrum from $I_{12k}/(I_{4f1} + I_{4f2} + I_{2a}) = 6/5$ to about 3/5, it can be assumed that 3 of 6 Fe^{3+} cations per formula unit pass from 12k sites to the interstitial sites in the hexagonal structure of ferrites. This structural change leads to the considerable reduction of the effective magnetic moment of hexaferrites from 20 μ_B/f.u. to $\mu = (-2 + 3 + 1 - 2 + 1) \times 5\ \mu_B = 5\ \mu_B$/f.u. (collinear spin alignment is considered). It should be noted, however, that the presence of nonequilibrium cation distributions in ferrites effects their spin arrangement and results in the formation of *canted* magnetic structures [110-112]. In other words, the spins of Fe^{3+} cations in nanocrystalline milled $BaFe_{12}O_{19}$ and $SrFe_{12}O_{19}$ materials may not be collinear anymore, leading to further reductions of μ. In this case, the magnetic moment of each sublattice μ_i depends not only on the occupation factors of Fe^{3+} cations in the given sublattice but also on the average spin canting angles Ψ_i (i = $4f_2$, 12k, 2a, $4f_1$, 2b). The effective magnetic moment of noncollinear magnetic structures can be expressed as $\mu = \Sigma\mu_i\cos\Psi_i$. Spins located on the ferrite sublattices may behave differently and the resulting spin canting effect generally tends to reduce the total μ [96,100,113-115]. Consequently, both nonequilibrium cation distribution and spin canting present in nanocrystalline $BaFe_{12}O_{19}$ and $SrFe_{12}O_{19}$ can lead to the formation of "dead" regions with $\mu \approx 0$.

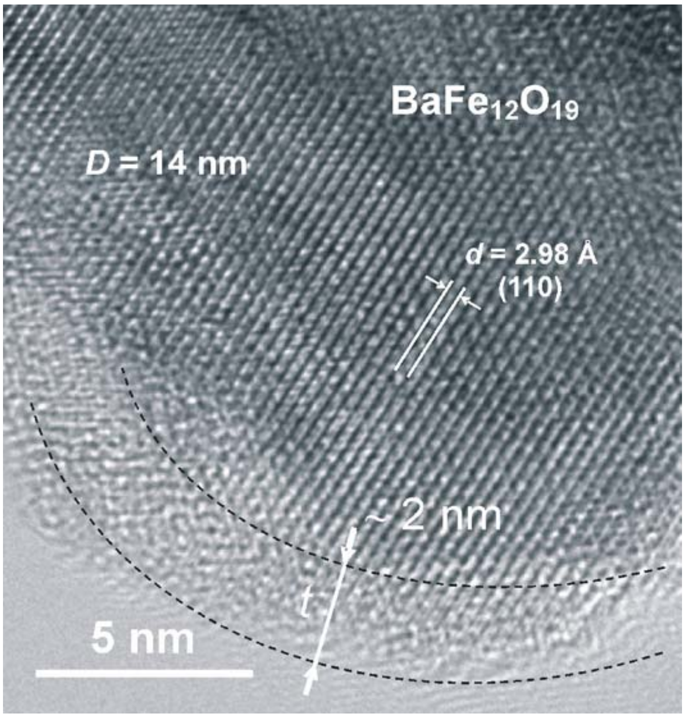

Figure 3.14. High-resolution TEM image of nanocrystalline $BaFe_{12}O_{19}$. The core–shell configuration of nanoparticles with the thickness of the surface shell of about 2 nm is evident.

A representative high-resolution TEM micrograph of nanocrystalline $BaFe_{12}O_{19}$ (t_m = 4 h) at high magnification is shown in Fig. 3.14. It reveals the spherical shape of a nanoparticle with D = 14 nm, consistent with the average crystallite size determined by XRD. As seen, the ferrite nanoparticle possesses the core–shell structure consisting of an ordered inner core surrounded by a disordered surface shell region. The HR-TEM image shows lattice fringes corresponding to the crystallographic plane (110) (d = 2.98 Å) of the $BaFe_{12}O_{19}$ phase (JCPDS PDF 27-1029) [42]. The lattice fringes cross the whole particle core demonstrating its single-crystalline character. The thickness of the disordered surface shell (t) estimated from HR-TEM was found to be about 2 nm (see Fig. 3.14).

Taking into account the core–shell configuration of hexaferrite nanoparticles prepared by mechanochemical method, it can be assumed that both nonequilibrium cation distribution and spin canting are located in the surface shell regions of the nanomaterial. This assumption is consistent with recent work on spinel ferrites [96,100,116]. Furthermore, a nonequilibrium cation distribution was also found in the near-surface layers of nonmagnetic spinel ($MgAl_2O_4$) nanoparticles [117], where, apart from the tetrahedral and octahedral cation coordinations, the presence of additional five- and threefold coordinated cations has been observed. Moreover, in some cases, the surface shell regions of nanooxides were found to be even amorphous [118-120]. Also in our case, the surface shell of hexaferrite nanoparticles seems to be amorphous (see Fig. 3.14). It may be mentioned in this respect that the appearance of some of the Fe^{3+} cations in interstitial positions of the hexagonal lattice can result in a local distortion of the structure. In the same way as Fe ions, the relatively large Ba or Sr cations can also be displaced from their regular positions, and can additionally modify the local structure, leading to the formation of an amorphous state. Similar disordering effects have already been observed, for example, in mechanochemically prepared spinels, where the formation of nonequilibrium cation distribution was found to be accompanied by deformation of polyhedron geometry and/or by the appearance of an amorphous shell [121,122].

Assuming a spherical shape of hexaferrite nanoparticles prepared by mechanochemical method and taking both their average diameter (D = 14 nm) and the thickness of their surface shell (t = 2 nm) as determined experimentally by XRD and TEM, one can easily deduce quantitative information on the volume fraction of surface shell regions to the volume of whole particles ($w = V_{\mathrm{shell}}/(V_{\mathrm{core}} + V_{\mathrm{shell}})$) in the nanomaterial; $w = [1 - (1 - 2t/D)^3]$. The estimated value of w = 0.636 indicates that about 64% of atoms in the milled ferrite are in a structurally and magnetically disordered state located in the surface shell of nanoparticles. A nonuniform core–shell structure of nanoparticles with a relatively large volume fraction of surface shell regions (~50%) has recently been reported for mechanosynthesized $NiFe_2O_4$ [96], $MgFe_2O_4$ [100], and ball-milled nanocrystalline $LiNbO_3$ [118].

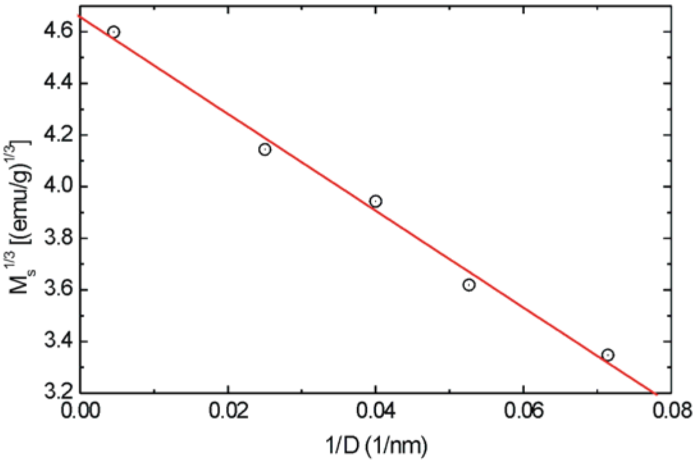

Figure 3.15. $M_{\mathrm{s}}^{1/3}$ vs $1/D$ plot, where M_{s} is the saturation magnetization and D is the diameter of $BaFe_{12}O_{19}$ nanoparticles.

In the following, we will estimate the shell thickness using the experimentally determined D and M_{s} values of $BaFe_{12}O_{19}$ milled for various times (see Table 3.4). Assuming that t is independent of D and that the shell is magnetically "dead", the variation of M_{s} with D will then be described by

$$M_{\mathrm{s}} = M_{\mathrm{core}}(D-2t)^3/D^3, \text{ or } M_{\mathrm{s}}^{1/3} = M_{\mathrm{core}}^{1/3}(1-2t/D),$$

where M_{core} is the saturation magnetization of the core of $BaFe_{12}O_{19}$ particles. As can be seen in Fig. 3.15, the present experimental data of $M_{\mathrm{s}}^{1/3}$ and $1/D$ indeed show a good linear relationship. Note that the intercept at $1/D = 0$ and the slope of the straight line correspond to $M_{\mathrm{core}}^{1/3}$ and $2tM_{\mathrm{core}}^{1/3}$, respectively. From a linear fit to the data points, the saturation magnetization of the particle core and the thickness of the shell were estimated to be $M_{\mathrm{core}} \approx 101.0$ emu/g and $t \approx 2.0$ nm, respectively. M_{core} thus obtained is close to the value of the saturation magnetization measured for bulk $BaFe_{12}O_{19}$, 97.3 emu/g. The value of the shell thickness obtained is in agreement with that estimated directly from HR-TEM experiments (2 nm). The shell thickness observed in the present case for nanocrystalline $BaFe_{12}O_{19}$ is comparable to that reported for other nanosized mechanochemically prepared complex oxides [96,100,118-120,123-125].

4 Heterogeneous Mechanochemical Reactions

In this Chapter we will point out that, despite the physical nature of the high-energy milling process, chemical changes can be detected in mechanically treated solids, i.e., so-called heterogeneous chemical reactions can be induced by mechanochemical processing. It will be demonstrated that various types of *heterogeneous mechanochemical reactions* such as *formation reactions*, *redox reactions*, and *decomposition reactions* of compounds can be initiated by mechanical action.

4.1 Local Structure and Magnetic Behavior of Nanocrystalline MnZn Spinel Ferrite Prepared by a One-Step Mechanochemical Route

Mechanically induced formation reactions represent one of the major fields of mechanochemistry [126,127]. The preparation of metastable products with unusual properties provides a major source of motivation for *mechanochemical synthesis* (mechanosynthesis) [128]. In this Section, the one-step synthesis of $Mn_{0.5}Zn_{0.5}Fe_2O_4$ via high-energy milling of the mixture of two single phase ferrites, $MnFe_2O_4$ and $ZnFe_2O_4$, is reported. Moreover, the local structure and the magnetic properties of the as-prepared material are highlighted. To the best of our knowledge, the single-step mechanosynthesis of MnZn ferrite from the mixture of two *ternary oxides* has only been reported in Ref. [129]. In previous studies [130,131], MnZn ferrites were prepared via mechanochemical processing of *binary oxide* precursors (MnO, ZnO, Fe_2O_3). In some cases, complete formation of the mixed MnZn spinel ferrite was obtained only after milling followed by annealing at elevated temperature, i.e., by employing two processing steps [132,133].

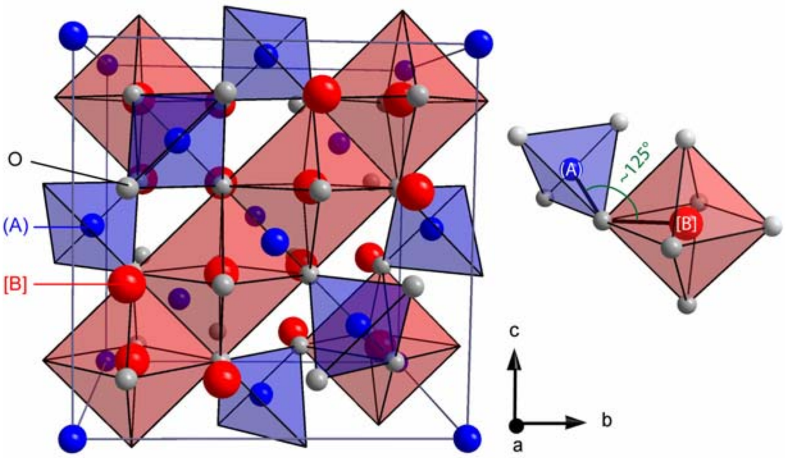

Figure 4.1. The cubic unit cell of spinel oxides consists of 56 ions: 32 anions (O^{2-}) and 24 cations. In ternary spinel ferrites, MFe_2O_4, M and Fe cations are distributed over the sites of tetrahedral (A) and octahedral [B] coordination.

MnZn ferrite, as a soft magnetic material, is an important member of the spinel ferrite family with the general formula MFe_2O_4 (M is a divalent metal cation such as Mn and Zn). Ferrites with the *spinel structure* are commercially important materials because of their excellent electrical and magnetic properties as well as of their chemical and thermal stability

[134,135]. These ferrites have been widely used in electronic applications such as transformers, choke coils, noise filters, recording heads, etc. [135]. The spinel structure of oxides is shown in Fig. 4.1.

A whole range of distributions of *M* and Fe cations is possible in ferrites, whose crystal chemical formula can be generally represented by $(M^{2+}_{1-\lambda}\mathrm{Fe}^{3+}_{\lambda})[M^{2+}_{\lambda}\mathrm{Fe}^{3+}_{2-\lambda}]\mathrm{O}_4$, where the round and square brackets denote cation sites of tetrahedral (A) and octahedral [B] coordination, respectively [136]. λ represents the so-called degree of inversion defined as the fraction of the (A) sites occupied by Fe^{3+} cations. The cation arrangement can vary between two extreme cases. One is the normal spinel ($\lambda = 0$), where all the divalent *M* cations occupy (A) sites and all the trivalent Fe cations occupy [B] sites. The other one is the inverse spinel ($\lambda = 1$), where all the divalent ions occupy [B] sites and trivalent cations are equally distributed between (A) and [B] sites. Spinels with the cation distribution intermediate between normal and inverse (i.e., partially inverse spinels; $0 < \lambda < 1$) are also very frequent. The value of $\lambda_s = 2/3$ corresponds to the random arrangement of cations in spinels. The properties of spinel ferrites are highly sensitive to the cation distribution which in turn depends on the procedure of preparation [137].

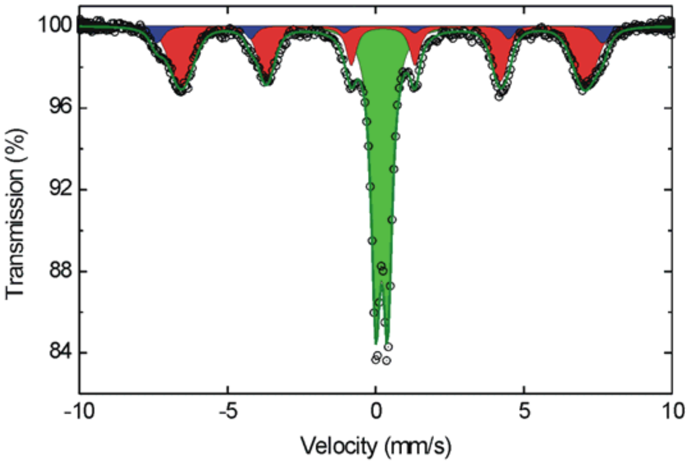

Figure 4.2. Room-temperature ^{57}Fe Mössbauer spectrum of the initial $\mathrm{MnFe_2O_4/ZnFe_2O_4}$ mixture. Blue, red, and green colors denote subspectra corresponding to Fe^{3+} cations in (A) and [B] sites of $\mathrm{MnFe_2O_4}$ as well as in the [B] sublattice of $\mathrm{ZnFe_2O_4}$, respectively.

Figure 4.2 presents the Mössbauer spectrum of the initial $\mathrm{MnFe_2O_4/ZnFe_2O_4}$ mixture that can be well fitted by a superposition of a paramagnetic doublet (IS = 0.201(2) mm/s, QS = 0.403(4) mm/s, $I = 47.43(1)\%$) and two sextets ($\mathrm{IS_{(A)}}$ = 0.133(3) mm/s, $H_{(A)}$ = 46.61(4) T, $I_{(A)}$ = 8.02(2)%; $\mathrm{IS_{[B]}}$ = 0.254(5) mm/s, $H_{[B]}$ = 42.23(4) T, $I_{[B]}$ = 44.63(4)%). The hyperfine parameters of the doublet component are typical for octahedrally coordinated Fe^{3+} cations in the normal spinel $\mathrm{ZnFe_2O_4}$ phase with the structural formula of $\mathrm{(Zn)[Fe_2]O_4}$ [61,82]. The hyperfine parameters of the two sextets are characteristic of the magnetically ordered (ferrimagnetic) $\mathrm{MnFe_2O_4}$, where both the Fe^{3+} and Mn^{2+} cations occupy the (A) and [B] spinel sublattices. The degree of inversion of $\mathrm{MnFe_2O_4}$ was calculated to be $\lambda \approx 0.30$ ($I_{(A)}/(I_{[B]} = f_{(A)}/f_{[B]} \times \lambda/(2 - \lambda)$), i.e., its structural formula can therefore be written as $\mathrm{(Mn_{0.70}Fe_{0.30})[Mn_{0.30}Fe_{1.70}]O_4}$. For the calculation, it was assumed that the ratio of the recoilless fractions is $f_{[B]}/f_{(A)} = 1$.

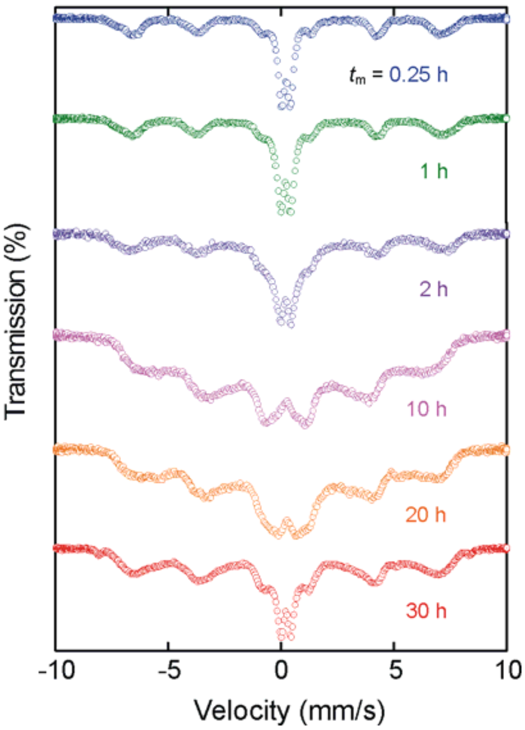

Figure 4.3. Room-temperature ^{57}Fe Mössbauer spectra of the $MnFe_2O_4/ZnFe_2O_4$ mixture milled for various times.

The room-temperature ^{57}Fe Mössbauer spectra of the $MnFe_2O_4/ZnFe_2O_4$ mixture milled for various times are shown in Fig. 4.3. As can be seen, with increasing milling time up to 2 h, only a broadening of the spectral components takes place due to the introduction of defects into both materials. For milling times from 2 to 20 h, the following qualitative changes of the spectra are observed: in addition to the very broad spectral lineshape, the spectra exhibit the “sagging” background typical for a nanomaterial [138,139]. This indicates that in this stage of milling, the milled sample consists of nanosized particles. The spectrum of the sample milled for 30 h shows a doublet and the broad sextet structure. A small amount (about 2 wt %) of Fe_2O_3 (small sextet with $H \approx 51$ T) is also present in the mechanosynthesized sample. It should be noted that the average hyperfine field of the broad sextet is slightly reduced, indicating the different phase composition of the milled sample in comparison with that of the initial mixture of ferrites. The second point indicating the formation of a new phase is that the spectral intensity corresponding to the magnetically ordered phase (sextet) increased after 30 h of milling to a value of $I_m = 82.22(3)\%$ (compared to $I = 52.65(6)\%$ at the beginning of the milling process). Additionally, the third point indicating the progress of a mechanically induced formation reaction is that the quadrupole splitting of the central doublet ($QS_{doublet}$) possesses the same value as that reported for $Mn_{0.5}Zn_{0.5}Fe_2O_4$ in the superparamagnetic state, QS = 0.44 mm/s [140,141]. Thus, there are several indications for the formation of mixed Mn-Zn spinel ferrite, whose spectral components (see Mössbauer spectrum of the sample milled for 30 h in Fig. 4.3) can be understood to arise from Fe^{3+} in $Mn_{0.5}Zn_{0.5}Fe_2O_4$ particles with larger size (sextet) and smaller size exhibiting superparamagnetic relaxation (doublet). It should be noted that similar spectra consisting of the superposition of sextet and doublet have also been reported for other mechanosynthesized spinel ferrites [97,100]. Based on the analysis of the present room-temperature ^{57}Fe Mössbauer spectra of the milled

$MnFe_2O_4$/$ZnFe_2O_4$ mixture, it can be presumed that the following mechanochemical reaction took place: $MnFe_2O_4 + ZnFe_2O_4 \rightarrow 2\ Mn_{0.5}Zn_{0.5}Fe_2O_4$.

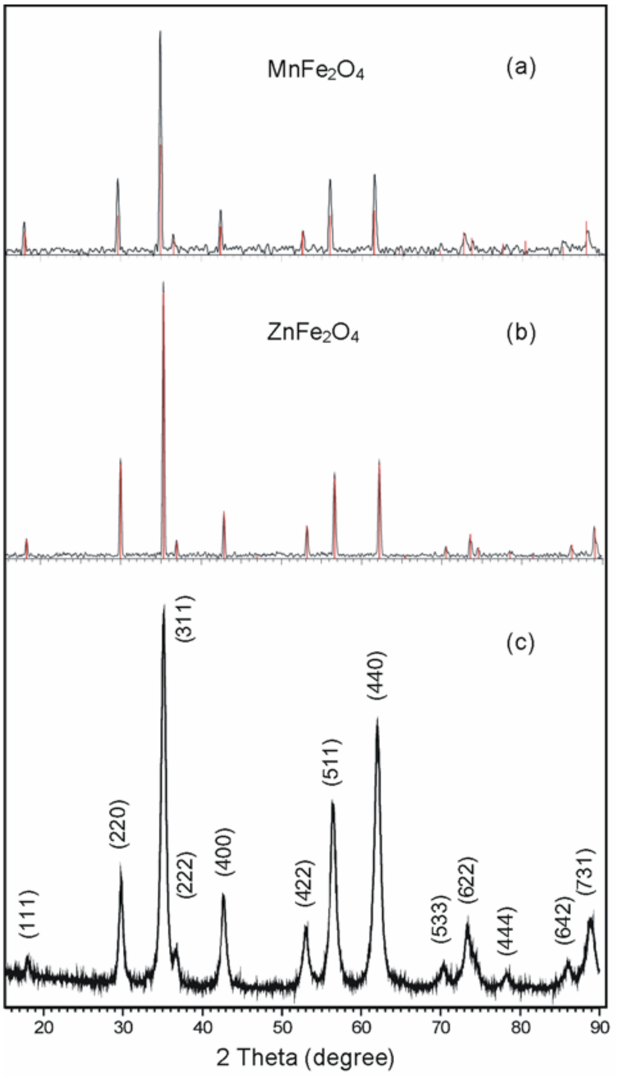

Figure 4.4. XRD patterns of (a) $MnFe_2O_4$, (b) $ZnFe_2O_4$ and (c) the product of the mechanochemical reaction, t_{mill} = 30 h. All the XRD patterns are dominated by typical diffraction peaks of the cubic spinel structure denoted by Miller indices.

To determine the nature of the mechanochemical transformation of the $MnFe_2O_4$/$ZnFe_2O_4$ mixture, we performed an XRD study, magnetization experiments, and low-temperature ^{57}Fe Mössbauer measurements in conjunction with large external magnetic fields. Figures 4.4 (a) and (b) show XRD patterns of the single phases $MnFe_2O_4$ and $ZnFe_2O_4$ prepared by the conventional ceramic technique, which served as precursors in the present mechanochemical reaction. As seen, the XRD patterns of the starting materials are characterized by sharp diffraction peaks corresponding to crystalline $MnFe_2O_4$ (JCPDS PDF 10-0319) and $ZnFe_2O_4$ (JCPDS PDF 22-1012) [42]. The patterns are almost identical because of the cubic spinel structure of both phases with the similar lattice constants ($a_{MnFe2O4}$ = 8.499 Å, $a_{ZnFe2O4}$ = 8.441 Å). For comparison, the XRD pattern of the mixture milled for 30 h (product of the mechanochemical reaction) is also depicted in Fig. 4.4 (c). Taking into account the same crystal structure of both precursors and the possible mechanosynthesized product and the broad XRD lines of the milled oxide, it is obvious that the XRD technique loses its power to resolve the presence of the $Mn_{0.5}Zn_{0.5}Fe_2O_4$ phase in the milled powder.

Nevertheless, this technique revealed the nanocrystalline character of the milled powder with an average crystallite size of about 14 nm.

The results of the magnetization measurements presented below that have already been published [142], unambiguously show that milling of the $MnFe_2O_4/ZnFe_2O_4$ mixture leads to the disappearance of the educt phases, i.e., they indirectly confirmed that mechanosynthesis of the Mn-Zn ferrite takes place. The field-cooled (FC) magnetization curves of the $MnFe_2O_4/ZnFe_2O_4$ mixtures milled for various times are shown in Fig. 4.5. As can be seen, the FC curves of the mixture milled for 15 min and 20 h exhibit a single maximum at about 8 K (see Figs. 4.5 (a) and (b)), which can be associated with the Néel temperature (T_N) of $ZnFe_2O_4$ [143,144], i.e., with the presence of $ZnFe_2O_4$ in the milled powder. This is in contrast to the magnetic behavior of the sample milled for 30 h, whose magnetization monotonically decreases with increasing temperature (see Fig. 4.5 (c)). Thus, the presence of the local maximum in the FC curve indicates that the sample milled for 20 h still contains $ZnFe_2O_4$. The absence of the local maximum in the FC curve of the $MnFe_2O_4/ZnFe_2O_4$ mixture milled for 30 h (Fig. 4.5. (c)) confirms that the mechanochemical synthesis of $Mn_{0.5}Zn_{0.5}Fe_2O_4$ is complete (no $ZnFe_2O_4$ is present in the milled powder).

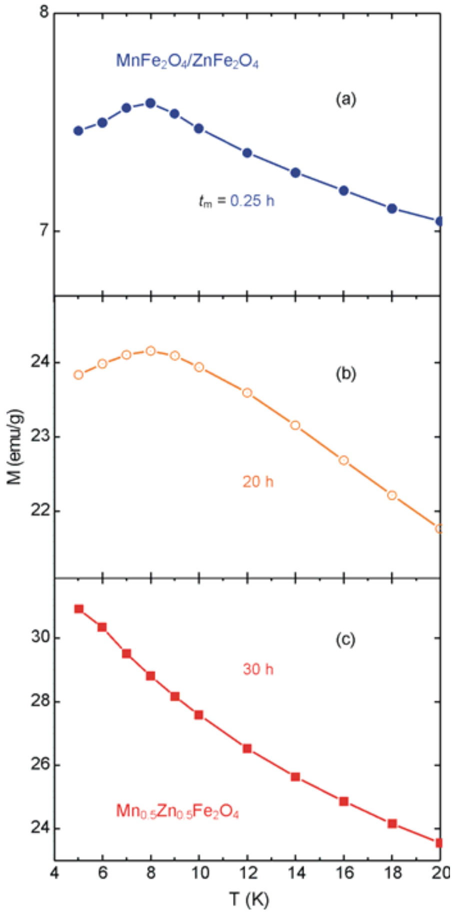

Figure 4.5. The FC magnetization curves (taken at $H_{ext} = 0.01$ T) for the $MnFe_2O_4/ZnFe_2O_4$ mixtures milled for (a) 0.25 h, (b) 20 h, and (c) 30 h.

Figure 4.6 compares the low-temperature (10 K) magnetization hysteresis loops of $MnFe_2O_4/ZnFe_2O_4$ mixtures milled for 15 min and 30 h. As can be seen, the hysteresis loop of the sample milled for 15 min does not saturate even at maximum attainable field ($H_{ext} = 5$ T).

That the magnetization of this sample increases linearly with the applied field in the field range from about 1 to 5 T indicates the presence of a paramagnetic phase ($ZnFe_2O_4$). Thus, the low-temperature hysteresis loop of the initial sample is a superposition of ferrimagnetic and paramagnetic parts, corresponding to $MnFe_2O_4$ and $ZnFe_2O_4$, respectively. On the contrary, the magnetization of the $MnFe_2O_4/ZnFe_2O_4$ mixture milled for 30 h does not increase linearly in the high-field region due to the absence of the paramagnetic phase. Thus, from the results of the magnetic measurements presented above, it is concluded that the complete formation of the $Mn_{0.5}Zn_{0.5}Fe_2O_4$ spinel is obtained after 30 h of high-energy milling.

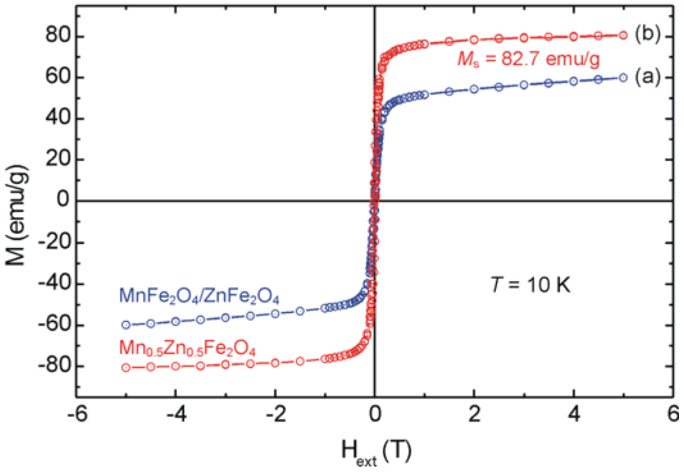

Figure 4.6. Magnetization hysteresis loops for (a) $MnFe_2O_4/ZnFe_2O_4$ mixtures milled for 0.25 h and (b) mechanosynthesized $Mn_{0.5}Zn_{0.5}Fe_2O_4$ (t_m = 30 h). The loops were measured at 10 K after field cooling with H_{ext} = 5 T.

It is interesting to mention that the magnetization of the mechanosynthesized $Mn_{0.5}Zn_{0.5}Fe_2O_4$ does not saturate even at the maximum attainable field (H_{ext} = 5 T); see the M-H_{ext} loop shown in Fig. 4.6 (b). This behavior is typical for ferrite systems with canted spins and a nonequilibrium cation distribution in the surface shell of the nanoparticles [96,100]. By plotting M vesus $1/H_{ext}$, we estimated the value of the saturation magnetization of mechanosynthesized $Mn_{0.5}Zn_{0.5}Fe_2O_4$ to be approximately 82.7 emu/g, which is about 41% lower than the value reported for bulk $Mn_{0.5}Zn_{0.5}Fe_2O_4$ (140 emu/g) [134]. It should be noted that a reduced saturation magnetization (M_s = 92 emu/g at 5 K) has already been reported for $Mn_{0.5}Zn_{0.5}Fe_2O_4$ nanoparticles [145]. The structural origin of the reduced saturation magnetization of mechanosynthesized $Mn_{0.5}Zn_{0.5}Fe_2O_4$ will be explained below.

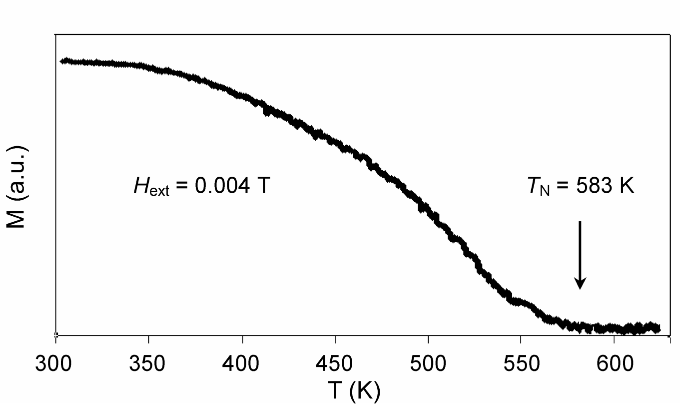

Figure 4.7. The variation of magnetization with temperature for mechanosynthesized $Mn_{0.5}Zn_{0.5}Fe_2O_4$ revealing its enhanced Néel temperature of $T_N \approx 583$ K. The magnetization data taken at $H_{ext} = 0.004$ T.

The second important observation is that the mechanosynthesized $Mn_{0.5}Zn_{0.5}Fe_2O_4$ exhibits an enhanced Néel temperature. Figure 4.7 shows the magnetization variation of the ferrite sample with temperature, measured in a magnetic field of 0.004 T. As expected, the magnetization decreases with increasing temperature; at 543 K there is an inflection point on the $M(T)$ curve and finally, the magnetization falls to zero at around 583 K, forming a cusp. This type of unusual variation of magnetization with temperature has already been reported for magnetic nanopowders [146,147]. Thus, from the M-T curve the Néel temperature of $Mn_{0.5}Zn_{0.5}Fe_2O_4$ nanoparticles is estimated to be about 583 K. This value is considerably higher than that reported for bulk $Mn_{0.5}Zn_{0.5}Fe_2O_4$ (413 K) [134].

To elucidate the origin of both the reduced saturation magnetization and the enhanced Néel temperature of mechanosynthesized $Mn_{0.5}Zn_{0.5}Fe_2O_4$, we performed *low-temperature in-field* ^{57}Fe Mössbauer measurements. These experiments enable us to determine both ionic configuration and spin arrangement in the mechanosynthesized ferrite nanoparticles. The low-temperature (4.2 K) Mössbauer spectra of mechanosynthesized $Mn_{0.5}Zn_{0.5}Fe_2O_4$, taken in zero applied magnetic field and in a magnetic field of 7 T applied parallel to the γ-ray direction, are compared in Fig. 4.8. As clearly seen, the thermal fluctuations are suppressed at 4.2 K, and the Mössbauer spectrum of nanocrystalline $Mn_{0.5}Zn_{0.5}Fe_2O_4$ consists of sextets only. Although the influence of superparamagnetic relaxation is counteracted, a determination of the cation distribution in $Mn_{0.5}Zn_{0.5}Fe_2O_4$ nanoparticles is impossible to make from the low-temperature spectrum at $H_{ext} = 0$ T (Fig. 4.8 (a)) because it is difficult to resolve the subspectra to assign them to the respective lattice sites. In the presence of an external magnetic field of $H_{ext} = 7$ T, the effective magnetization of the individual particles is aligned along the field. As a consequence of the antiparallel alignment of the spins of Fe^{3+} cations at (A) and [B] sites in spinel ferrites, the external field adds to the magnetic hyperfine field at (A) sites and subtracts from the hyperfine field at [B] sites [148]. Because of this fact, the high-field Mössbauer spectrum of nanosized mechanosynthesized $Mn_{0.5}Zn_{0.5}Fe_2O_4$ exhibits the completely resolved (A) and [B] subspectra (see Fig. 4.8 (b)). Thus, the use of the large external magnetic fields creates an effective separation of the subpatterns, thereby allowing for an accurate determination of the cation distribution. The hyperfine parameters of (A)- and [B]-site ferric ions resulting from the least-squares fitting of the spectrum of nanosized

$Mn_{0.5}Zn_{0.5}Fe_2O_4$ are presented in Table 4.1. The degree of inversion of the mechanosynthesized $Mn_{0.5}Zn_{0.5}Fe_2O_4$ was found to be $\lambda = 0.555(4)$.

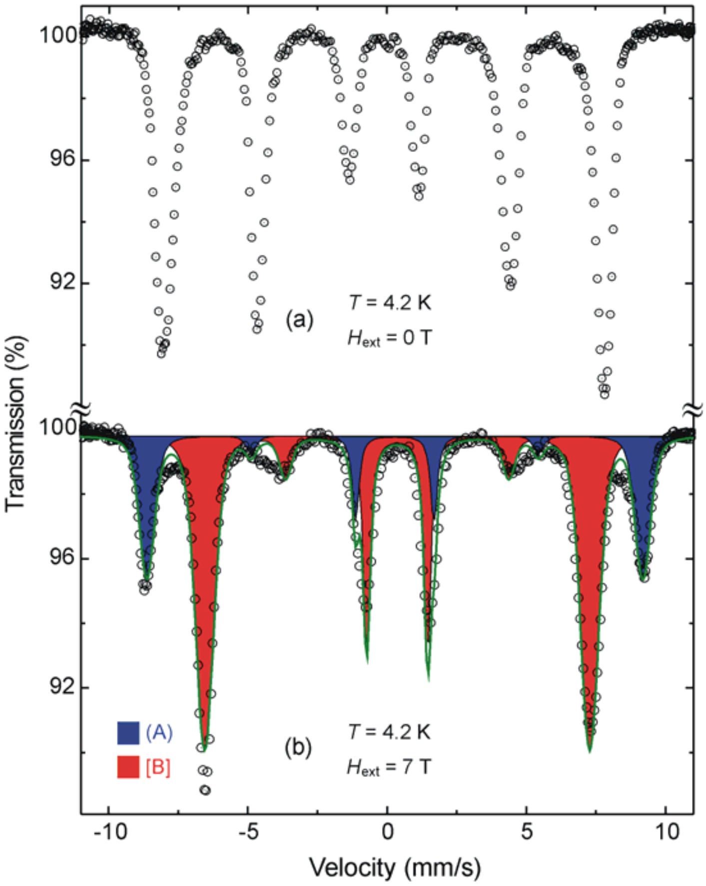

Figure 4.8. Low-temperature (4.2 K) Mössbauer spectra of nanosized mechanosynthesized $Mn_{0.5}Zn_{0.5}Fe_2O_4$ taken (a) in zero applied magnetic field and (b) in external magnetic field of 7 T applied parallel to the γ-ray direction. Blue and red subspectra correspond to Fe^{3+} cations in tetrahedral (A) and octahedral [B] coordination of oxygen ions, respectively.

If the external magnetic field H_{ext} is applied parallel to the γ-ray direction, the second and fifth lines of the six-line Mössbauer spectrum vanish for fully collinear magnetic structures [149]. However, Fig. 4.8 (b) indicates that in the present study the intensity ratio of the second (or fifth) line to the first (or sixth) line, $I_{2,5}/I_{1,6}$, takes small values for both (A) and [B] subspectra. This implies that Fe-spins in the (A) and [B] sites of the mechanosynthesized material are strongly canted under the applied field. The obtained intensity ratios $I_{2,5}/I_{1,6}$ for each subspectrum are also listed in Table 4.1. The average canting angle, Ψ, can be calculated from this intensity ratio according to $\Psi = \arcsin\{[3(I_{2,5}/I_{1,6})/2]/[1 + 3(I_{2,5}/I_{1,6})/4]\}^{1/2}$ [94]. The average canting angles, characterizing noncollinear spin arrangement of Fe^{3+} ions on (A) and [B] sites in the mechanosynthesized ferrite, were found to be $\Psi_{(A)} = 22.6(5)$ and $\Psi_{[B]} = 24.0(7)°$, respectively. Thus, the spins located on the two sublattices in the mechanosynthesized material are found to behave slightly different in the external field of 7 T. This result is also consistent with previous work, where different spin canting in the (A) and [B] sublattices of spinel nanostructures was observed [112-115].

Table 4.1. Hyperfine parameters (IS – isomer shift, H_{eff} – effective magnetic field, I – relative intensity, $I_{2,5}/I_{1,6}$ – intensity ratio of the second (or fifth) line to the first (or sixth) line, Ψ – average spin canting angle, H – magnetic hyperfine field) obtained by fitting the low-temperature in-field Mössbauer spectrum of nanocrystalline mechanosynthesized $Mn_{0.5}Zn_{0.5}Fe_2O_4$.

Parameter	**Fe^{3+} (A)**	**Fe^{3+} [B]**
IS (mm/s)	0.262(1)	0.369(5)
I (%)	27.77(7)	72.23(7)
$I_{2,5}/I_{1,6}$	0.106(9)	0.120(8)
Ψ (°)	22.6(5)	24.0(7)
H_{eff} (T)	55.30(4)	42.90(1)
H (T)	48.91(2)	49.37(7)

The effective magnetic fields $H_{\mathrm{eff(A)}}$ and $H_{\mathrm{eff[B]}}$ observed at the ^{57}Fe nuclei in (A) and (B) sites of mechanosynthesized $Mn_{0.5}Zn_{0.5}Fe_2O_4$, respectively, are listed in Table 4.1. Note that the effective magnetic field is the vector sum of the magnetic hyperfine field (H) and the applied field H_{ext} [150]. The values of the magnetic hyperfine field (listed in Table 4.1) were estimated from those of the effective magnetic field and external magnetic field using the relationship $\mathrm{H}^2 = \mathrm{H}_{eff}^2 + \mathrm{H}_{ext}^2 \mp 2\mathrm{H}_{eff}\mathrm{H}_{ext}\cos\Psi$ [113], where – and + are for (A) and [B] spectral components, respectively. It is found that the magnetic hyperfine fields experienced by Fe^{3+} ions located in the (A) and [B] sites of the mechanosynthesized material are very similar ($H_{\mathrm{(A)}}$ = 48.91(2) T and $H_{\mathrm{[B]}}$ = 49.37(7) T); thus, it would be impossible to resolve the (A) and [B] subspectra even at low temperatures without application of an external magnetic field (see also Fig. 4.8 (a)).

Based on the quantitative results of the low-temperature in-field ^{57}Fe Mössbauer measurements, it can be stated that the atomic and spin configurations in the mechanosynthesized $Mn_{0.5}Zn_{0.5}Fe_2O_4$ are characterized by a nonequilibrium cation distribution and noncollinear spin alignment, respectively. Taking into account that Zn^{2+} ions have a strong preference for (A) sites in spinels [151], the crystal chemical formula of the mechanosynthesized ferrite can therefore be written as $(Zn_{0.44}Fe_{0.56}\searrow)[Zn_{0.06}Mn_{0.50}Fe_{1.44}\nearrow]O_4$. In analogy with the core–shell configuration of mechanosynthesized complex oxides [96,100,152], it can be assumed that both nonequilibrium cation distribution and canted spins are located in the surface shell regions of the $Mn_{0.5}Zn_{0.5}Fe_2O_4$ nanoparticles. Note that the cation distribution in the bulk Mn-Zn ferrite can be described by the following crystal chemical formula: $(Zn_{0.50}Mn_{0.5})[Fe_2\uparrow]O_4$ [153].

The quantitative information on the ion configuration and the spin structure, obtained from the analysis of Mössbauer spectra, is very helpful in the interpretation of both the reduced saturation magnetization M_{s} and the enhanced Néel temperature T_{N} of mechanosynthesized $Mn_{0.5}Zn_{0.5}Fe_2O_4$. Since Zn^{2+} ions possess no magnetic moment, the total magnetic moment μ in $Mn_{0.5}Zn_{0.5}Fe_2O_4 \equiv (Zn_xMn_yFe_\lambda)[Zn_{0.5-x}Mn_{0.5-y}Fe_{2-\lambda}]O_4$ is entirely due to the uncompensated magnetic moments of Fe^{3+} and Mn^{2+} ions. Thus, from the λ and Ψ values, the effective magnetic moment (per formula unit) of $Mn_{0.5}Zn_{0.5}Fe_2O_4$ can be calculated as:

$\mu = \mu_{[\mathrm{B}]} - \mu_{(\mathrm{A})} = [(2-\lambda)\,\mu_{\mathrm{Fe}}\cos\Psi_{[\mathrm{B}]} + (0.5-y)\,\mu_{\mathrm{Mn}}\cos\Psi_{[\mathrm{B}]\mathrm{Mn}}] - (\lambda\,\mu_{\mathrm{Fe}}\cos\Psi_{(\mathrm{A})} + y\,\mu_{\mathrm{Mn}}\cos\Psi_{(\mathrm{A})\mathrm{Mn}})$, where μ_{Fe} and μ_{Mn} are magnetic moments of Fe^{3+} and Mn^{2+} ions, respectively: $\mu_{\mathrm{Fe}} = \mu_{\mathrm{Mn}} = 5$ μ_{B}. The values $\lambda = 0$, $x = 0.5$, $y = 0.5$, and $\Psi_{(\mathrm{A})} = \Psi_{[\mathrm{B}]} = 0°$, characteristic of the bulk Mn-Zn ferrite [153], result in the magnetic moment $\mu_{\mathrm{bulk}} = 7.50$ μ_{B}/f.u.. On the other hand, the values $\lambda = 0.56$, $x = 0.44$, $y = 0$, and $\Psi_{(\mathrm{A})} = 22.6°$, $\Psi_{[\mathrm{B}]} = \Psi_{[\mathrm{B}]\mathrm{Mn}} = 24.0°$ (the same canting angles are assumed for Fe^{3+} and Mn^{2+} spins in [B] sites), characteristic of the mechanosynthesized material, lead to the effective magnetic moment $\mu_{\mathrm{nano}} = 6.28$ μ_{B}/f.u.. Thus, the disordered cation and spin configurations theoretically lead to the M_{s} value that is approximately 1.2 times smaller than that of the ordered bulk material. This is in reasonable agreement with the results of magnetization measurements, which demonstrate that M_{s} of mechanosynthesized $Mn_{0.5}Zn_{0.5}Fe_2O_4$ is about 1.7 times smaller than that calculated for the bulk material. Thus, the theoretical considerations presented above clearly demonstrate that the origin of the reduced M_{s} of mechanosynhtesized Mn-Zn ferrite lies in both nonequilibrium cation distribution and spin disorder. In analogy with other mechanosynthesized spinel ferrites, the magnetic degradation observed in the present case can be attributed to the nonequilibrium cation and noncollinear spin effects in the surface shell of $Mn_{0.5}Zn_{0.5}Fe_2O_4$ nanoparticles [96,100].

Taking into account the crystal chemical formulas of $(Zn_{0.50}Mn_{0.5})[Fe_2]O_4$ and $(Zn_{0.44}Fe_{0.56})[Zn_{0.06}Mn_{0.50}Fe_{1.44}]O_4$, characteristic of bulk and nanocrystalline Mn-Zn ferrites, respectively, it is evident that the mechanosynthesized ferrite possesses a larger number of the (A)-O-[B] exchange paths. This is directly related to the Néel temperature of the ferrite system [112]. The enhanced T_{N} observed for the mechanosynthesized material can therefore be attributed to the strengthening of the (A)-O-[B] superexchange interaction due to an increase of the magnetic ion concentration in the (A) site [154-155].

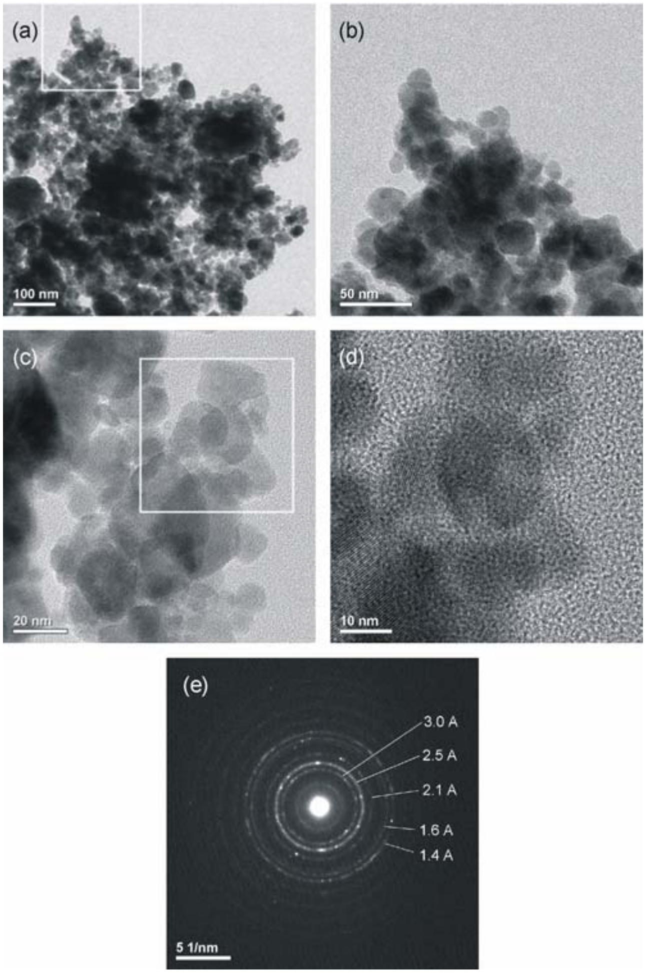

Figure 4.9. (a) TEM bright-field image of nanoscale mechanosynthesized $Mn_{0.5}Zn_{0.5}Fe_2O_4$. (b) Nanoparticles exhibit strong tendency for agglomeration. (c) TEM micrographs of $Mn_{0.5}Zn_{0.5}Fe_2O_4$ nanocrystals at (c) low and (d) high magnification. (e) SAED pattern of $Mn_{0.5}Zn_{0.5}Fe_2O_4$ nanoparticles.

The shape, size and morphology of mechanosynthesized $Mn_{0.5}Zn_{0.5}Fe_2O_4$ particles were examined by direct observation via TEM. Bright-field TEM images (Figs. 4.9 (a) and (b)) illustrate the nanoscale nature of the ferrite particles mostly in the 10-30 nm size range. The shape of the majority of the nanoparticles appears spherical. TEM micrographs of nanocrystalline mechanosynthesized $Mn_{0.5}Zn_{0.5}Fe_2O_4$ at low and high magnification are shown in Figs. 4.9 (c) and (d). The crystalline nature of nanosized particles is also visible (Fig. 4.9 (d)). Corresponding selected area electron diffraction (SAED) pattern, displayed in Fig. 4.9 (e).

4.2 Mechanosynthesis of Nanocrystalline $CaFe_2O_4$ with Orthorhombic Structure

In this Section, we will report on the single-step synthesis of $CaFe_2O_4$ with the orthorhombic structure via high-energy milling of two different mixtures of precursors: simple oxides (CaO and α-Fe_2O_3) and elemental metal and oxide powders (Ca and α-Fe_2O_3). The study also demonstrates that the yield of the mechanochemical formation reaction strongly depends on the choice of the reactants used.

The system Ca-Fe-O has for several decades been the subject of a great number of studies because of its applications as oxidation catalysts, high-temperature sensors, gas absorbers, etc. [156,157]. Nowadays, Ca-Fe-O complex oxides are promising materials for high-temperature electrochemical devices, such as ceramic membranes and electrodes of solid oxide fuel cells [158]. The phase diagram of CaO-Fe_2O_3 shows the existence of two compounds: $CaFe_2O_4$ with orthorhombic structure and $Ca_2Fe_2O_5$ with the brownmillerite one. $CaFe_2O_4$ is used as pigment [159] or as anode in lithium batteries [160] and as photocathodic material. $Ca_2Fe_2O_5$ is mostly employed as catalytic material [161].

Many methods have been employed to synthesize Ca-Fe-O complex oxides using simple oxides, carbonates, organic precursors, hydroxides, and also using solution chemistry. $CaFe_2O_4$ for example has been synthesized using the ceramic method by annealing a mixture of $CaCO_3/Fe_2O_3$ for 24 h at 1453 K [160]. This demonstrates that the conventional solid-state synthesis of $CaFe_2O_4$ proceeds very slowly and requires prolonged exposure at considerably elevated temperatures. Also the Pechini process has been used to prepare crystalline $CaFe_2O_4$ at 1073 K [162] and the coprecipitation process has been successfully employed as well [163]. A novel synthesis procedure of both calcium ferrites ($CaFe_2O_4$ and $Ca_2Fe_2O_5$) was proposed in [164], starting from mechanically activated mixtures of organic precursors (calcium citrate tetrahydrate and iron(III) oxalate hexahydrate). It was shown that the mechanically pre-activated mixtures yield, after an 18 h anneal at 1073 K (or 1023 K), $Ca_2Fe_2O_5$ (or $CaFe_2O_4$). In comparison, the same compounds could be obtained, when starting from the nonactivated mixtures, only by performing thermal treatments (for $t > 18$ h) at 1453 K ($Ca_2Fe_2O_5$) or 1373 K ($CaFe_2O_4$). Thus, mechanical pre-activation of the solid organic reactants considerably reduced the temperature and duration of the formation of the ferrite product during subsequent thermal treatment. Moreover, $Ca_2Fe_2O_5$ has been prepared by subjecting to mechanical activation a mixture of $Ca(OH)_2/\alpha$-FeOOH and by heating the activated mixture between 673 and 1273 K [165]. The synthesis of $Ca_2Fe_2O_5$ has also been performed by thermal decomposition of $Ca[Fe(CN)_5NO]\cdot 4H_2O$ [166].

The above-given analysis of the literature procedures shows that various precursors have been employed for the synthesis of Ca-ferrites. It should be emphasized that the use of a metal/oxide precursor system has not been tested yet. The following paragraphs clearly demonstrate that the yield of the mechanochemical reaction, leading to nanocrystalline $CaFe_2O_4$, is considerably higher if the Ca/α-Fe_2O_3 mixture is used instead of the CaO/α-Fe_2O_3 precursor system (at the same preparation conditions). To the best of our knowledge, the single-step mechanosynthesis of nanosized $CaFe_2O_4$ particles has not been reported before.

The mechanically induced evolution of the Ca/α-Fe_2O_3 and CaO/α-Fe_2O_3 mixtures submitted to high-energy milling was followed by ^{57}Fe Mössbauer spectroscopy (see Fig. 4.10). The spectra of both starting mixtures (Ca/α-Fe_2O_3 and CaO/α-Fe_2O_3) show a sextet with a magnetic hyperfine field of 51.6(4) T corresponding to α-Fe_2O_3 (see Fig. 4.10, top). With increasing milling time, the sextet becomes asymmetric toward the inside of each line, slowly collapses, and is gradually replaced by a central doublet. This spectral component can be assigned to the mechanosynthesized $CaFe_2O_4$ product [157]. Note that the Mössbauer spectrum of α-Fe_2O_3 exhibits only a broadened sextet even if the particles size of the material reaches the nanoscale range; i.e., it does not display a superparamagnetic doublet (see Fig. 4.30 on page 60). The fact that the spectral components, corresponding to educt (α-Fe_2O_3) and product ($CaFe_2O_4$) phases, are clearly resolved in the spectra, gives evidence that ^{57}Fe Mössbauer spectroscopy provides a very sensitive probe for the estimation of the yield of this mechanochemical reaction.

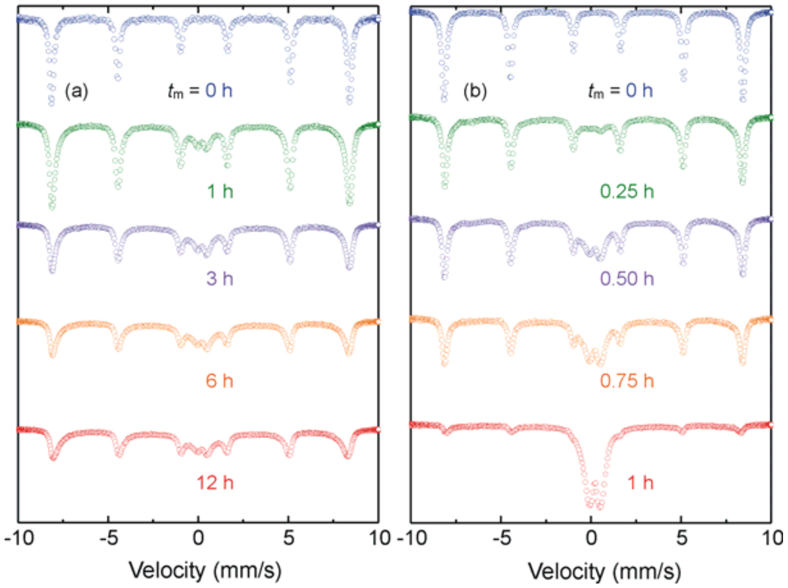

Figure 4.10. Room-temperature ^{57}Fe Mössbauer spectra of (a) the CaO/α-Fe_2O_3 mixtures and (b) the Ca/α-Fe_2O_3 powders milled for various times (t_m).

The decrease in the intensity of the Mössbauer sextet corresponding to α-Fe_2O_3, I_{sext}, relative to the total spectral intensity, I_{tot}, reflects a gradual conversion of the reactants to the ferrite phase during milling (see Fig. 4.11). As can be seen, the mechanosynthesis of $CaFe_2O_4$ from the metal/oxide system proceeds very rapidly; after only 1 h of the mechanochemical treatment, the synthesis of the complex oxide is almost completed. This is in strong contrast to the mechanochemical processing of the oxide/oxide precursor system; even after 12 h of the high-energy milling, the yield of the reaction reaches only about 23%.

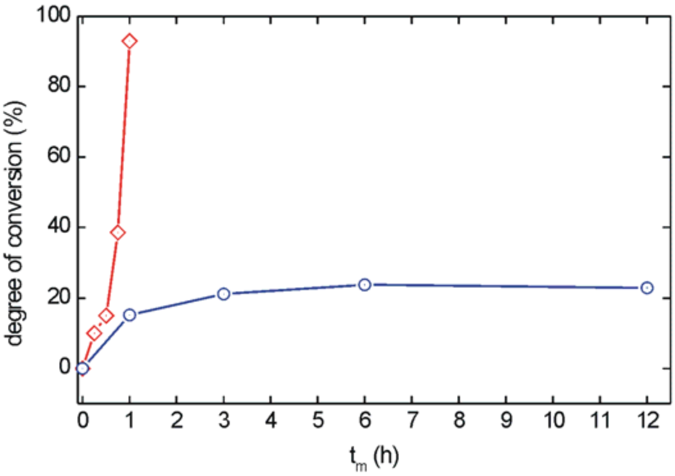

Figure 4.11. Variation of the degree of conversion of the mechanosynthesis of $CaFe_2O_4$ with milling time. Red and blue lines correspond to the mechanosynthesis starting from the Ca/α-Fe_2O_3 and CaO/α-Fe_2O_3 mixtures, respectively. The degree of conversion was calculated from the relative intensity of the Mössbauer sextet corresponding to α-Fe_2O_3, I_{sext}, relative to the total spectral intensity, I_{tot}, according to $(1 - I_{sext}/I_{tot})\times 100$.

The reason for the different behaviour of the metal/oxide and oxide/oxide precursor systems during the processing may lie in both the different chemical affinity and mechanical properties of Ca and CaO (the metal is more ductile than the oxide). Generally, the following factors are primarily responsible for a favorable effect of mechanochemical activation on the synthesis: dispersion and defect formation in starting reactants; the formation of fresh surfaces, which accelerates chemical interaction between reactants; and the mixing of components on a molecular level [167]. Nevertheless, the exact mechanism of the very rapid mechanosynthesis of $CaFe_2O_4$ from the metal/oxide system is not clear. In the last few years, the synthesis of complex oxide systems based on the acid-base interaction in the co-activation of hydroxides - mild mechanochemical synthesis (the so-called soft mechanosynthesis [168]) - has been developed. Calcium and iron hydroxides can be considered as such components of different basicity [165].

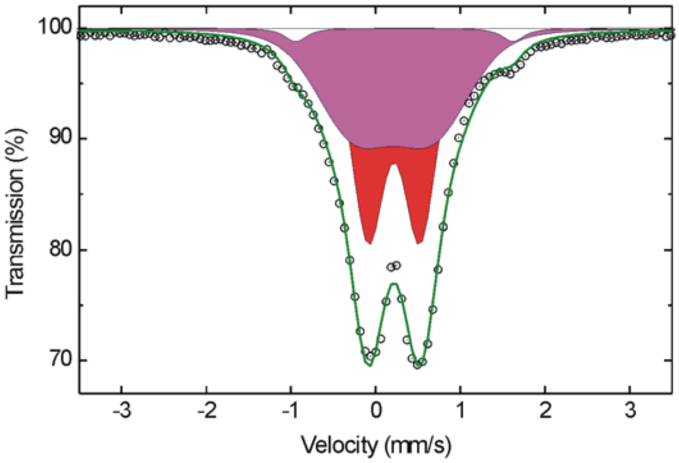

Figure 4.12. The central part of the room-temperature ^{57}Fe Mössbauer spectrum of mechanosynthesized $CaFe_2O_4$. Red and magenta subspectra correspond to Fe^{3+} cations in nonequivalent octahedral sites in the orthorhombic structure of the ferrite. The minor (~10%) white subspectrum is associated with Fe^{3+} ions in the unreacted α-Fe_2O_3 phase.

In addition to the yield of the reaction, ^{57}Fe Mössbauer spectroscopy provided information on the charge states, the local symmetry and the magnetic state of iron ions in the mechanosynthesized material. The slightly asymmetrical central doublet in the spectrum of mechanosynthesized ferrite (see Fig. 4.12) indicates the presence of at least two crystallographically nonequivalent iron positions in the structure. This spectrum is hence fitted by using two quadrupole spectral components corresponding to the ferrite and one sextet associated with the unreacted α-Fe_2O_3 phase. The estimated isomer shift values (IS_1 = 0.216(7) mm/s, IS_2 = 0.210(1) mm/s) of the doublet components are both typical for ferric ions in octahedral coordination [82]. The quadrupole splittings of the spectral components (QS_1 = 0.613(7) mm/s, QS_2 = 0.924(2) mm/s) reflect different values of the electric field gradients acting on Fe^{3+} nuclei in the two nonequivalent octahedral positions of the mechanosynthesized material. These values are larger than those reported for the conventionally synthesized (bulk) $CaFe_2O_4$ (QS_1 = 0.30 mm/s, QS_2 = 0.75 mm/s) [158,169]. Note that larger electric field gradients are typically observed for mechanosynthesized complex oxides [137] which are produced by an asymmetric electronic charge distribution around the iron ions due to the distortion of polyhedra. For both octahedra, the relative intensities of the spectral components are almost equal, reflecting the same occupation factor of iron cations within these structural units. Thus, the crystal chemical formula of the mechanosynthesized material can be written as follows: $Ca[Fe]_{oct1}[Fe]_{oct2}O_4$, where brackets enclose Fe^{3+} cations in nonequivalent distorted octahedra.

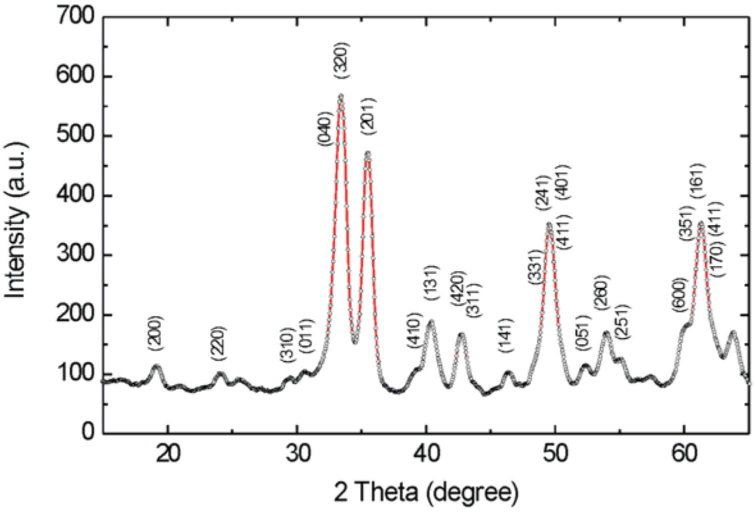

Figure 4.13. XRD pattern of the mechanosynthesized complex oxide $CaFe_2O_4$. Diffraction lines of the mechanosynthesized product are denoted by Miller indices.

To determine the phase evolution of the Ca/α-Fe_2O_3 and CaO/α-Fe_2O_3 mixtures during high-energy milling by an independently supporting method, both mechanochemical routes to $CaFe_2O_4$ were also followed by XRD. Figure 4.13 shows the XRD pattern of the mechanosynthesized $CaFe_2O_4$ product obtained after 1 h of milling of the Ca/α-Fe_2O_3 mixture. Based on the analysis of XRD data, the crystal structure of the product is found to be orthorhombic (JCPDS PDF 32-0168) [42]. The structure of $CaFe_2O_4$ with two distinct iron sites is composed by the corner- and edge-shared FeO_6 octahedra, see Fig. 4.14. This finding is in agreement with the present Mössbauer results, confirming the presence of two nonequivalent iron sites in $CaFe_2O_4$. The FeO_6 octahedra form pseudo-triangular tunnels where eightfold-coordinated Ca^{2+} cations are located. The Rietveld analysis of the XRD data of the mechanosynthesized material has revealed both an average crystallite size of about 28 nm and the presence of mean strains of 3×10^{-3} in the produced ferrite.

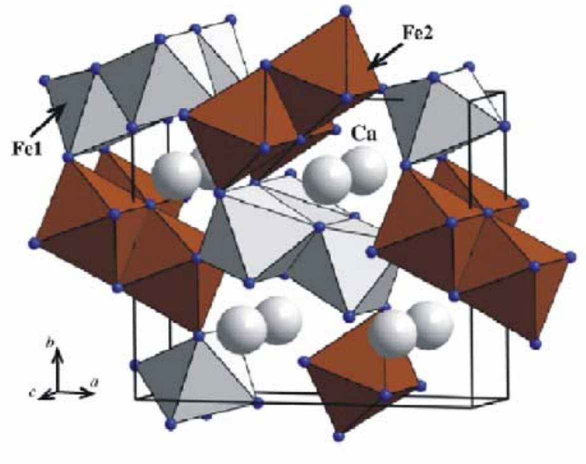

Figure 4.14. The crystal structure of mechanosynthesized $CaFe_2O_4$.

Representative TEM micrographs of nanocrystalline mechanosynthesized $CaFe_2O_4$ at high magnification are shown in Fig. 4.15. TEM reveals the presence of nanoparticles of irregular shape with a relatively broad size distribution ranging from about 8 nm to 30 nm (the average particle size is about 15 nm). Similarly as in the case of nanocrystalline $BaFe_{12}O_{19}$ and $SrFe_{12}O_{19}$ prepared by mechanochemical method (see Fig. 3.14), the mechanosynthesized $CaFe_2O_4$ nanoparticles also possess the core–shell structure consisting of an ordered inner core surrounded by a disordered surface shell region. The thickness of the surface shell was found to be about 1.9 nm (Fig. 4.15 (b)). The high-resolution TEM images show lattice fringes corresponding to the crystallographic plane (220) (d = 3.5 Å) of the $CaFe_2O_4$ phase. The lattice fringes cross the whole particle core demonstrating its single-crystalline character.

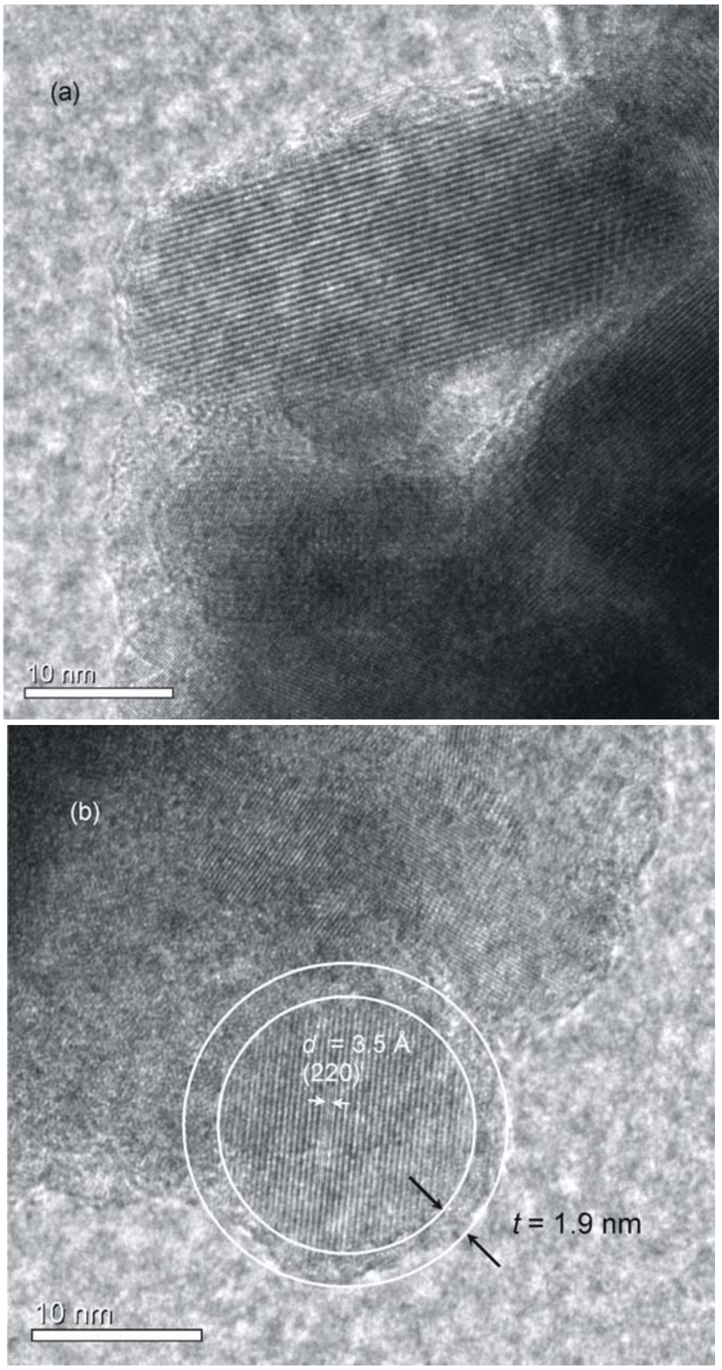

Figure 4.15. (a) High-resolution TEM image demonstrating the presence of $CaFe_2O_4$ nanoparticles of irregular shape with a relatively broad size distribution ranging from about 8 nm to 30 nm. (b) The core–shell configuration of mechanosynthesized nanoparticles with the thickness of the surface shell of about 1.9 nm is evident. The lattice fringes correspond to the crystallographic plane (220) (d = 3.5 Å) of the $CaFe_2O_4$ phase (JCPDS PDF 32-0168).

Assuming a spherical shape of mechanosynthesized $CaFe_2O_4$ nanoparticles with $D = 15$ nm and $t = 1.9$ nm, the volume fraction of surface shell regions was calculated to be $w = 0.584$. This indicates that about 58% of atoms in the mechanosynthesized ferrite are in a structurally disordered state located in the surface shell of the nanoparticles. It should be assumed that distorted octahedra, evidenced by Mössbauer spectroscopy, are located in the surface shell of nanoparticles.

4.3 Mechanosynthesis of Nanosized $(Fe_{1-x}Mg_x)_2SiO_4$ ($x = 0, 0.5, 1$) with Olivine Structure

Olivines of the type M_2SiO_4 (M is a divalent metal cation) are important rock-forming silicates, as they belong to the most abundant phases of the Earth's crust and upper mantle. In particular, the Fe-end member fayalite, Fe_2SiO_4, the Mg-end member forsterite, Mg_2SiO_4, as well as the Mg-Fe-olivine solid solution series, $(Fe_{1-x}Mg_x)_2SiO_4$, have been the subject of many experimental studies on crystallographic, thermodynamic and spectroscopic properties [170,171]. Silicates $(Fe_{1-x}Mg_x)_2SiO_4$ possess an orthorhombic crystal structure (see Fig. 4.16), in which four formula units are contained in the unit cell [170]. In the crystal, Si^{4+} cations are coordinated by four O^{2-} ions to form SiO_4 tetrahedra, which are linked together by the Fe atoms lying between them. Divalent cations in the olivine crystal structure occupy two nonequivalent octahedral sites, M1 and M2 of equal number. These two sites are different in size and site symmetry due to the different distortion from the regular octahedron. As shown in Fig. 4.16, layers of M1 and M2 sites are alternately arranged along the [010] direction and M1 chains are parallel to [001]. The internal cation distribution state of $(Fe_{1-x}Mg_x)_2SiO_4$ determines its structure, and its physical and chemical properties. A cation redistribution over M1 and M2 sites in olivine can be induced, for example, by temperature changes [172]. The cation intersite exchange processes in complex solids are fundamental steps for the attainment of internal thermodynamic equilibrium as well as for cation diffusion [173].

In this Section, we will report the first synthesis of nanocrystalline silicates $(Fe_{1-x}Mg_x)_2SiO_4$ ($x = 0$, 0.5 and 1) via mechanochemical processing of α-Fe_2O_3/Fe/MgO/SiO_2 mixtures at room temperature. Due to the ability of ^{57}Fe Mössbauer spectroscopy to discriminate between probe nuclei on nonequivalent crystallographic sites provided by the olivine structure, valuable insight into the local cation disorder in mechanosynthesized silicate is obtained. Quantitative microstructural information on the disordered cation arrangement provided by Mössbauer spectroscopy is complemented by XRD and TEM investigations revealing the nanoscale nature of the mechanosynthesized materials.

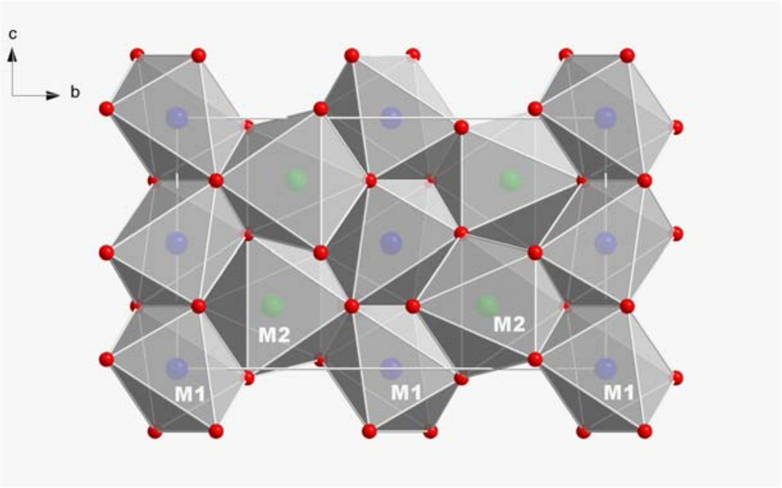

Figure 4.16. Schematic presentation of olivine structure. Octahedrally coordinated M1 and M2 sites are indicated.

Figures 4.17-4.19 show XRD patterns of the high-energy milled α-Fe_2O_3/Fe/MgO/SiO_2 mixtures with the stoichiometry required for the compositions $(Fe_{1-x}Mg_x)_2SiO_4$ with $x = 0$, 0.5, and 1, respectively. The XRD patterns of the starting powders are characterized by sharp diffraction peaks corresponding to the crystalline phases of α-Fe_2O_3 (JCPDS PDF 33-0664), Fe (JCPDS PDF 6-0696), MgO (JCPDS PDF 45-0946), and SiO_2 (JCPDS PDF 46-1045) [42]. Already after 0.5 h of milling, qualitative changes are observed in the XRD patterns of the milled samples. Intensities of the Bragg peaks of the individual educts decrease, and clear evidence is observed of diffraction features that correspond to the olivine (031) and (211) diffraction peaks.

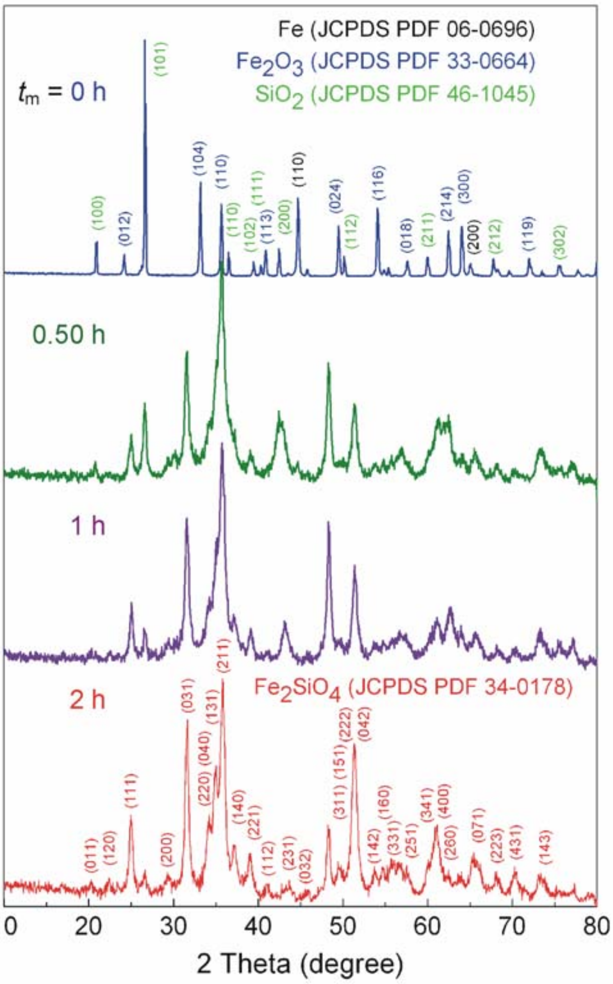

Figure 4.17. The mechanochemical route to nanocrystalline Fe_2SiO_4 followed by XRD. Diffraction lines of the reaction precursors and of the mechanosynthesized product are denoted by Miller indices. The milling times are also shown in the figure.

As seen in Fig. 4.17, after 2 h of high-energy milling, all XRD peaks detected above the background are due to the Fe_2SiO_4 phase (JCPDS PDF 34-0178). The broad shape of the XRD lines corresponding to fayalite indicates its nanoscale nature. Thus, nanocrystalline iron silicate is the product of the following mechanochemical reaction: 2 α-Fe_2O_3 + 2 Fe + 3 SiO_2 → 3 Fe_2SiO_4. The exact particle size of the mechanosynthesized complex nanooxide is analyzed concurrently using HR-TEM (see below).

The mechanosynthesis of $(Fe_{1-x}Mg_x)_2SiO_4$ with $x = 0.5$ and 1 was found to be complete after 3 h of milling. Figures 4.18 and 4.19 compare the XRD patterns of the initial mixtures with those of mechanosynthesized products.

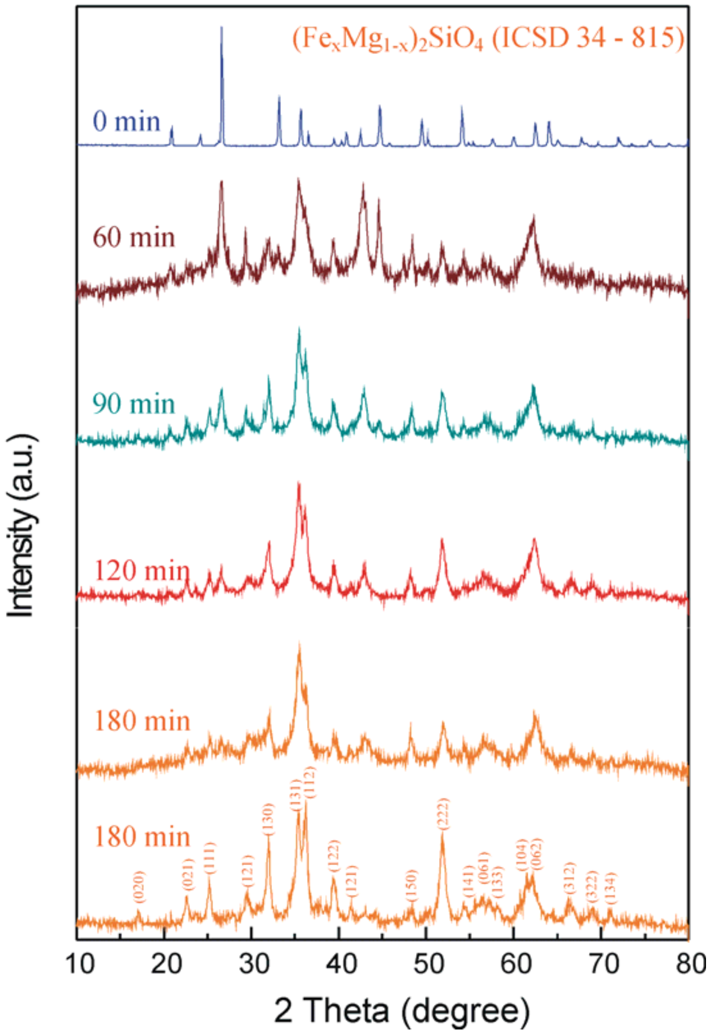

Figure 4.18. The comparison of the XRD patterns of the initial α-Fe_2O_3/Fe/MgO/SiO_2 mixture and of the mechanosynthesized $FeMgSiO_4$, at x = 0.5. Diffraction lines of the reaction precursors and of the mechanosynthesized product are denoted by Miller indices.

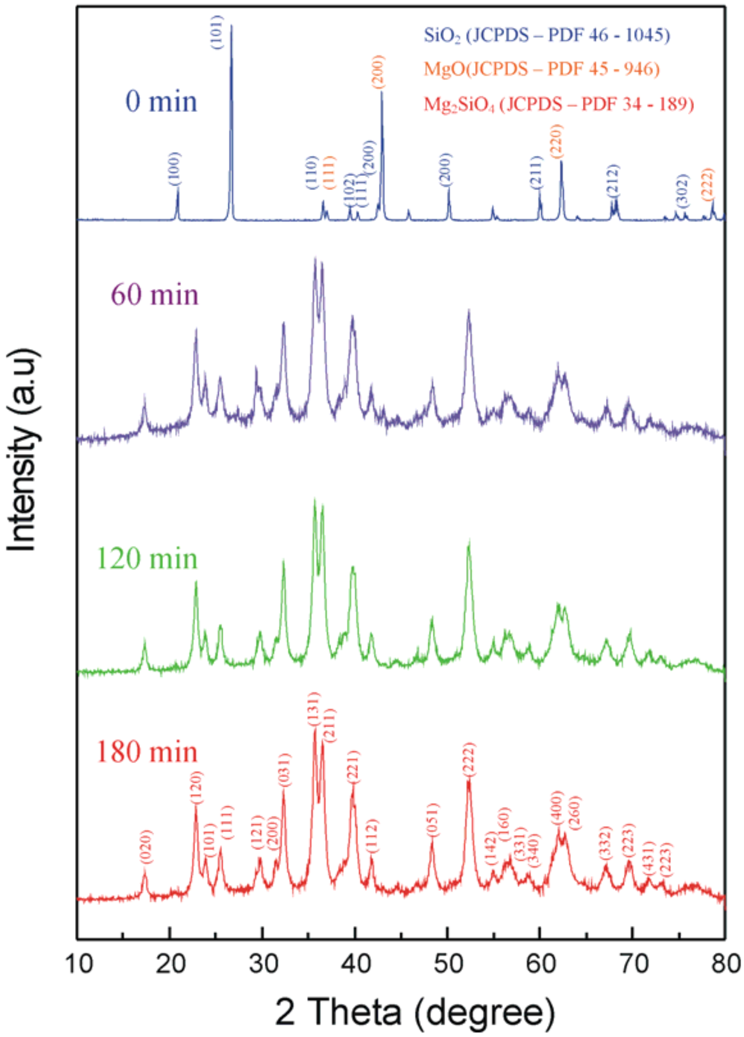

Figure 4.19. The comparison of the XRD patterns of the initial $2MgO/SiO_2$ mixture and of the mechanosynthesized Mg_2SiO_4. Diffraction lines of the reaction precursors and of the mechanosynthesized product are denoted by Miller indices.

The heterogeneous process of the mechanochemical formation reaction of the $(Fe_{1-x}Mg_x)_2SiO_4$ phases with $x = 0$ and 0.5 was also studied by ^{57}Fe Mössbauer spectroscopy. This is documented in the case of the mechanosynthesis of Fe_2SiO_4 in Fig. 4.20. As seen, with increasing milling time, sextets corresponding to α-Fe_2O_3 and Fe become asymmetric towards the inside of each line, slowly collapse, and are gradually replaced by a central doublet characteristic for Fe^{2+} ions.

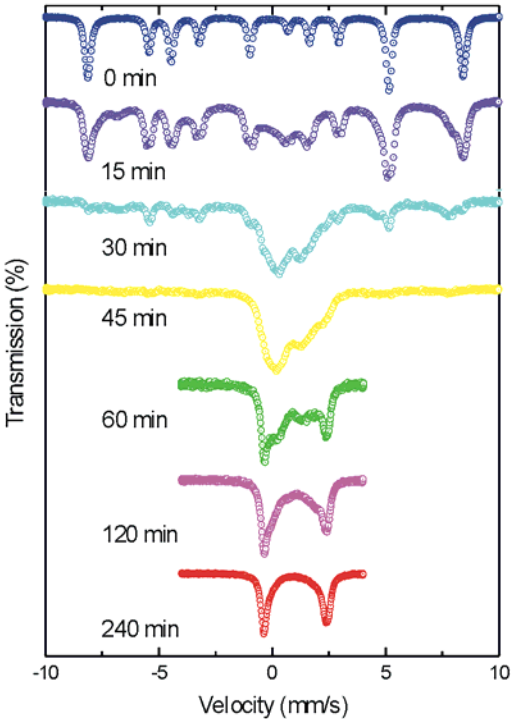

Figure 4.20. The room-temperature ^{57}Fe Mössbauer spectra illustrating the mechanosynthesis of Fe_2SiO_4 from the α-Fe_2O_3/Fe/SiO_2 mixture. The milling times are also shown in the figure.

It should be noted that the Mössbauer spectrum of the bulk (natural) Fe_2SiO_4 exhibits an asymmetric doublet indicating the presence of more than one subspectrum (see Fig 4.21). The spectrum is well fitted by the superposition of two doublet components with the hyperfine parameters: $IS_{M1} = 0.99(5)$ mm/s, $IS_{M2} = 1.02(8)$ mm/s; $QS_{M1} = 2.91(4)$ mm/s, $QS_{M2} = 3.02(1)$ mm/s; Gaussian widths $\sigma_{M1} = \sigma_{M2} \sim 0.04$ mm/s; and relative intensities of $I_{M1} \approx I_{M2} \approx 50\%$. These parameters are characteristic of Fe^{2+} ions in the olivine structure. The relative intensities of the subspectra indicate that the occupation factors of Fe^{2+} cations are equal for both sites. This is in agreement with previously published Mössbauer data on fayalite [173,174] and with the crystal structure. The structural formula emphasizing the cation site occupancy at the atomic level in the bulk Fe_2SiO_4 can therefore be written as $[Fe]_{M1}[Fe]_{M2}SiO_4$.

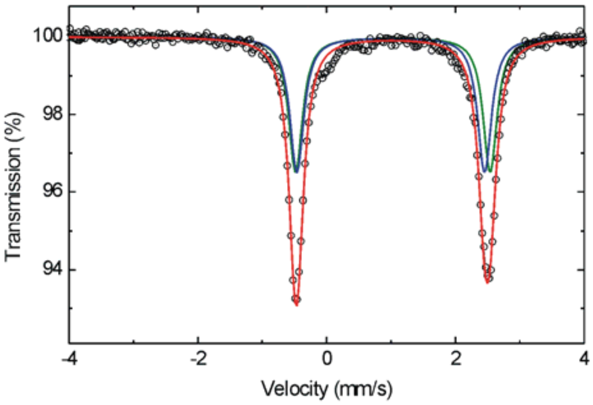

Figure 4.21. The room-temperature ^{57}Fe Mössbauer spectrum of bulk (natural) Fe_2SiO_4 (Peru). Blue and green colours indicate Fe^{2+} cations in M1 and M2 octahedral sites of olivine structure, respectively.

Taking into account the core-shell morphology of the nanoscale mechanosynthesized Fe_2SiO_4 (see below) its Mössbauer spectrum is fitted by a superposition of four subspectra (Fig. 4.22); two accounting for Fe^{2+} nuclei in the well-crystalline core of Fe_2SiO_4 nanoparticles (IS_{M1c} = 1.00(1) mm/s, IS_{M2c} = 1.04(5) mm/s, QS_{M1c} = 2.69(6) mm/s, QS_{M2c} = 2.89(1) mm/s, $\sigma_{M1c} = \sigma_{M2c}$ = 0.04 mm/s, $I_{M1c} = I_{M2c}$ = 30%) and two associated with Fe^{2+} ions in the surface shell/interface regions of nanoparticles (IS_{M1s} = 0.86(3) mm/s, IS_{M2s} = 1.03(3) mm/s, QS_{M1s} = 1.86(5) mm/s, QS_{M2s} = 2.41(8) mm/s, σ_{M1s} = 0.77(2) mm/s, σ_{M2s} = 0.40(1) mm/s, $I_{M1s} = I_{M2s}$ = 20%). The relatively broad shape of the Mössbauer spectral lines associated with surfaces/interfaces in comparison with that of the lines corresponding to the core of mechanosynthesized Fe_2SiO_4 nanoparticles (compare σ_{M1c}, σ_{M2c}, $\sigma_{M1s,}$ σ_{M2s}) provides clear evidence of a wide distribution of electric field gradients acting at the Fe^{2+} nuclei in the near-surface layers/interface regions of the mechanosynthesized material. Similarly as in the case of the mechanosynthesized $CaFe_2O_4$, this phenomenon reflects the presence of distorted M1 and M2 octahedra in the surface/interface regions of the mechanosynthesized Fe_2SiO_4 nanomaterial. The relative intensities of the spectral components $I_{M1s} = I_{M2s}$ = 20% indicate that the volume fraction of the surface/interface regions in this materials is w = 40%.

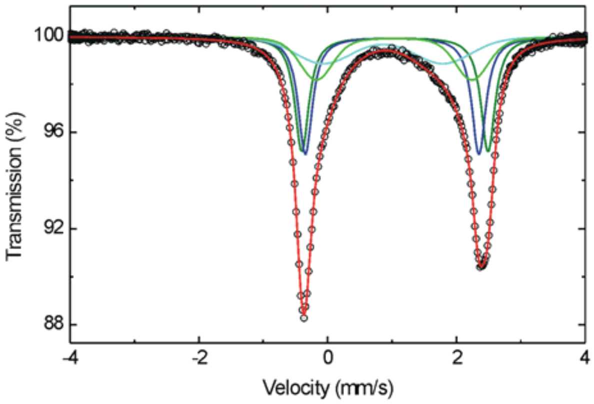

Figure 4.22. The room-temperature ^{57}Fe Mössbauer spectrum of nanoscale mechanosynthesized Fe_2SiO_4. Dark and light (blue and green) colours correspond to Fe^{2+} ions in the core and surface/interface regions of Fe_2SiO_4 nanoparticles, respectively.

To obtain a better resolution of the subspectra corresponding to Fe^{2+} cations in M1 and M2 sites the Mössbauer spectrum of the mechanosynthesized Fe_2SiO_4 nanomaterial was also measured in-situ at moderate temperatures under argon atmosphere (to prevent both the crystal growth and oxidation). The mössbauer spectrum of mechanosynthesized Fe_2SiO_4 collected at 573 K is shown in Fig. 4.23. As clearly seen, even through argon atmosphere was used a substantial part of Fe^{2+} cations was oxidized to Fe^{3+} (orange subspectrum in Fig. 4.23 with the following parameters: IS = 0.05 mm/s, QS = 1.03(5) mm/s, σ = 0.51(4) mm/s, I = 39.3(6)%). This may be related to a high reactivity of the nanomaterial caused by both its large surface/interface area (small particle size) and metastable (distorted) geometry of the surface/interface M1 and M2 octahedrons. The thermal treatment of the material also influenced the hyperfine parameters of the subspectra; the following parameters were derived: IS_{M1c} = 0.80(7) mm/s, IS_{M2c} = 0.86(6) mm/s, QS_{M1c} = 2.16(1) mm/s, QS_{M2c} = 2.48(5) mm/s,

σ_{M1c} = 0.08(2) mm/s, σ_{M2c} = 0.06(5) mm/s, $I_{M1c} = I_{M2c}$ = 20.2(3)%; IS_{M1s} = 0.81(1) mm/s, IS_{M2s} = 0.81(9) mm/s, QS_{M1s} = 1.01(6) mm/s, QS_{M2s} = 1.77(4) mm/s, σ_{M1s} = 0.55(5) mm/s, σ_{M2s} = 0.16(2) mm/s, $I_{M1s} = I_{M2s}$ = 9.9(4)%). As expected, the IS values of all the spectral components shifted to the left-hand side due to the second-order Doppler effect [82]. Generally, the QS value of the components decreases due to the increasing population of higher electronic energy levels of the Fe^{2+} ions with rising temperature.

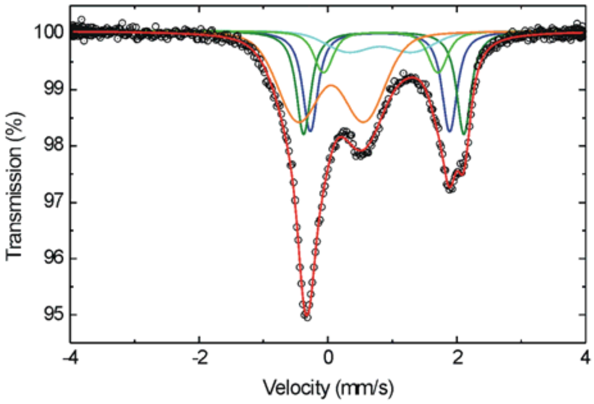

Figure 4.23. In-situ ^{57}Fe Mössbauer spectrum of nanoscale mechanosynthesized Fe_2SiO_4 taken at 573 K under an argon atmosphere. For the assignment of the spectral components, see Fig. 4.22 and the text above.

A representative TEM micrograph of the nanocrystalline mechanosynthesized $(Fe_{1-x}Mg_x)_2SiO_4$ phase with $x = 0.5$ at high magnification is shown in Fig. 4.24. TEM reveals the presence of nanoparticles of almost spherical shape with the average size D = 13 nm. The core–shell structure consisting of an ordered inner particle core surrounded by a disordered surface shell region is also visible. The volume fraction of the surface/interface regions estimated from HR-TEM (using the formula $w = 1 - (1 - 2t/D)^3$) was found to be about w = 0.544. This value is in reasonable agreement with the volume fraction of surfaces/interfaces derived from Mössbauer spectra (40%).

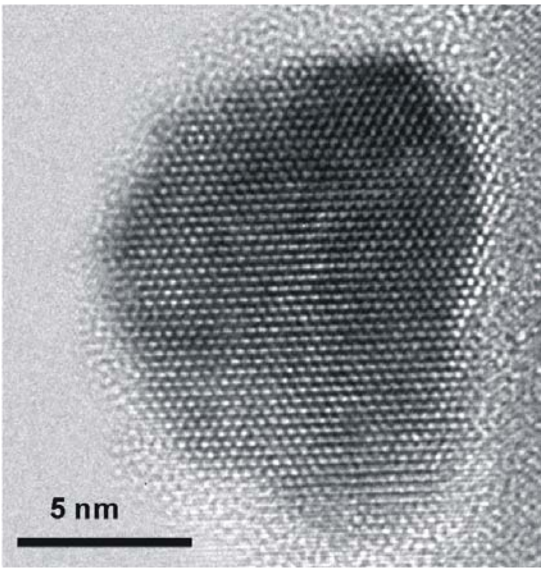

Figure 4.24. High-resolution TEM image of mechanosynthesized $FeMgSiO_4$. The presence of an almost spherical $FeMgSiO_4$ nanoparticle (D = 13 nm) with the core–shell configuration (t = 1.5 nm) is evident.

4.4 Mechanochemical Redox and Decomposition Reactions in Oxides

Chemical reduction and decomposition processes induced by mechanical treatment represent an important class of solid-state reactions. Many examples have been reported where reduction of simple binary oxides by a more reactive metal occurs during milling [175-179]. In ball-milling experiments involving α-Fe_2O_3 in air, reduction of α-Fe_2O_3 to Fe_3O_4 [180-183] and subsequently, to the $Fe_{1-x}O$ phase [184] has been observed to occur in a closed stainless steel container after prolonged milling. Depending upon the value of the adiabatic temperature of the redox reaction and milling conditions, the reaction may occur either in a steady-state manner during milling or by unstable thermal combustion of the reactants [185]. In addition to simple oxides, there have also been reports on the reduction of chlorides during high-energy milling [186].

While the mechanically induced redox reactions involving simple binary oxides are discussed extensively in the literature, the mechanochemical reduction of higher complex oxides is treated only to a limited extent. In this context, the mechanically induced reduction of ilmenite ($FeTiO_3$) and scheelite ($CaWO_4$) may be mentioned [187,188]. Similarly, there have been reports on the reduction on the mechanochemical reduction of spinels such as Fe_3O_4 [189,190], $NiFe_2O_4$ [139,191], $CuFe_2O_4$ [192], and $MgFe_2O_4$ [193].

The mechanochemical decomposition reactions are the most rarely studied heterogeneous processes in mechanochemistry. From available literature data, the following two cases can be mentioned: Goya *et al.* [192] followed the phase evolution of $CuFe_2O_4$ during high-energy milling. They showed that the final product of the mechanical treatment of copper ferrite is a two-phase mixture consisting of Fe_3O_4 and a spinel solid solution ($Cu_xFe_{3-x}O_4$). Joseyphus *et al.* [194] reported the decomposition of the $Gd_3Fe_5O_{12}$ garnet phase into Gd-orthoferrite ($GdFeO_3$) and Gd_2O_3 on milling. These two examples indicate that the high-energy milling of a solid generates a complex series of solid-state transformations, including reduction and mechanochemical decomposition.

In this Section, the study of the mechanically induced evolution of α-Fe_2O_3/SnO mixtures submitted to high-energy milling revealed the formation of FeO-SnO_2 nanocomposites, i.e., a mechanochemical redox process took place. Moreover, two examples are presented on the mechanochemical decomposition reactions of nanocrystalline hexaferrite ($SrFe_{12}O_{19}$) and olivine (Fe_2SiO_4) phases. To the best of our knowledge, these mechanochemical reactions have not been reported before.

The mechanically induced evolution of the α-Fe_2O_3/SnO mixtures was followed by ^{57}Fe and ^{119}Sn Mössbauer spectroscopy, see Fig. 4.25.

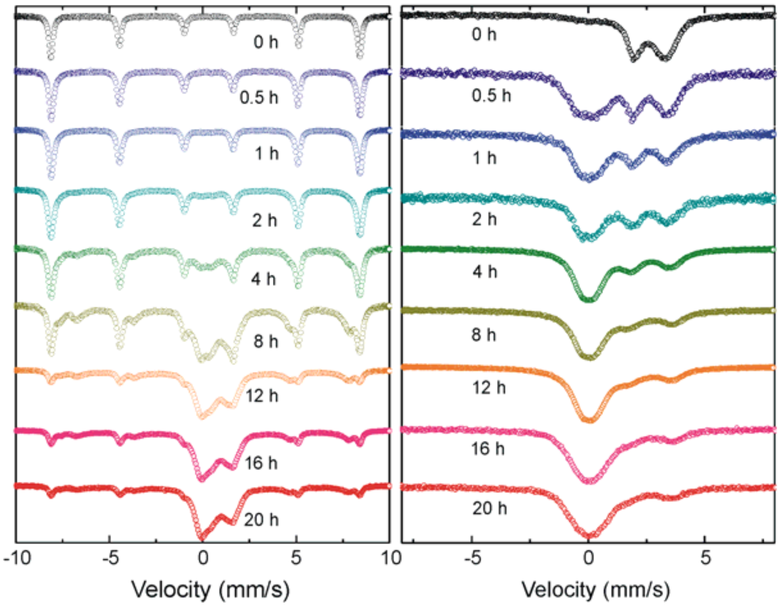

Fig. 4.25. ^{57}Fe (left) and ^{119}Sn (right) Mössbauer spectra of the Fe_2O_3/SnO mixtures milled for various times.

The ^{57}Fe Mössbauer spectrum of the starting α-Fe_2O_3/SnO mixture shows a sextet with a magnetic hyperfine field of 51.6(4) T corresponding to α-Fe_2O_3. With increasing milling time, the sextet becomes asymmetric toward the inside of each line, slowly collapses, and is gradually replaced by a central doublet. The fitting of the spectrum of the α-Fe_2O_3/SnO mixture milled for 20 h (see Fig. 4.26) reveals that the milled sample contains wüstite (FeO) (47.2 %), magnetite (Fe_3O_4) in magnetically ordered (21.6 %) and superparamagnetic (18.9 %) states, and hematite (α-Fe_2O_3) (12.2 %). The hyperfine parameters of the corresponding iron-containing phases are listed in Table 4.2.

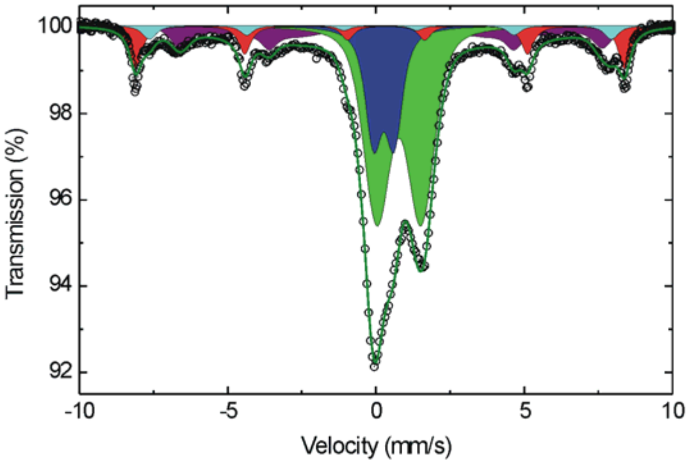

Fig. 4.26. ^{57}Fe Mössbauer spectrum of the Fe_2O_3/SnO mixture milled for 20 h. Green, dark blue, light blue, violet, and red colors denote Fe^{2+} in FeO, iron cations in superparamagnetic state in Fe_3O_4, iron cations in tetrahedral sites of Fe_3O_4, iron cations in octahedral sites of Fe_3O_4, and Fe^{3+} in α-Fe_2O_3, respectively.

Thus, ^{57}Fe Mössbauer spectroscopy indicates that mechanical treatment of the Fe_2O_3/SnO mixture leads to the reduction of Fe^{3+} cations, i.e., the following reduction reaction related to the iron-containing phases takes place: α-$Fe_2O_3 \rightarrow Fe_3O_4 \rightarrow$ FeO. Formation of magnetite (phase containing both Fe^{3+} and Fe^{2+} cations) as an intermediate product is clearly visible in the spectra of the samples milled for times $t_m \geq 4$ h (see Fig. 4.25, left). Its appearance in superparamagnetic and ferrimagnetic states corresponds to the formation of smaller and larger magnetite crystals, respectively. After milling for 20 h, the amount of magnetite in the mechanically treated mixture is about 40.6 %. The mechanochemical reduction of α-Fe_2O_3 is not completed after 20 h of milling: the mixture milled for 20 h contains about 12.2 % of hematite. In the present mechanochemical reaction, the final reduction (Fe-containing) product is wüstite phase (FeO) containing ferrous (Fe^{2+}) cations.

Table 4.2. Hyperfine parameters (IS – isomer shift, QS – quadrupole splitting, *B* – average magnetic hyperfine field, *I* – relative intensity) obtained by fitting the room-temperature Mössbauer spectrum of the Fe_2O_3/SnO mixture milled for 20 h. A Lorentzian line width Γ = 0.252(1) mm/s resulted from the fit of the spectrum.

Phase / Paramater	IS (mm/s)	QS (mm/s)	*H* (T)	*I* (%)
FeO	0.774(2)	1.499(1)	-	47.20(71)
Superparamagnetic Fe_3O_4	0.265(3)	0.691(9)	-	18.95(63)
Tetrahedral (A) site in Fe_3O_4	0.151(2)	0	48.3(3)	8.64(34)
Octahedral [B] site in Fe_3O_4	0.523(2)	0	37.2(3)	12.97(54)
α-Fe_2O_3	0.242(1)	-0.100(2)	51.0(8)	12.24(48)

The ^{119}Sn Mössbauer spectrum of the starting α-Fe_2O_3/SnO mixture (Fig. 4.25, right) is dominated by a doublet characteristic of Sn^{2+} cations (IS = 2.480(5) mm/s, QS = 2.184(4) mm/s, Γ = 0.407(4) mm/s). With increasing milling time, the relative intensity of the doublet decreases, and a new spectral component appears that corresponds to Sn^{4+} cations in SnO_2 (IS = -0.021(4) mm/s, QS = 0.922(7) mm/s). The fitting of the spectrum of the α-Fe_2O_3/SnO mixture milled for 20 h (see Fig. 4.27) reveals that the relative intensity of the new spectral components is about 74.1%. Thus, ^{119}Sn Mössbauer spectroscopy indicates that mechanical treatment of the Fe_2O_3/SnO mixture leads to the oxidation of Sn^{2+} cations to Sn^{4+}.

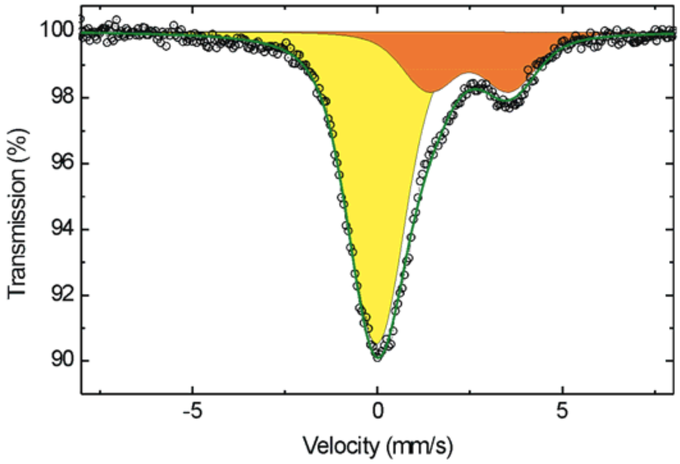

Fig. 4.27. ^{119}Sn Mössbauer spectrum of the Fe_2O_3/SnO mixture milled for 20 h. Orange and yellow colors denote subspectra due to Sn^{2+} and Sn^{4+} cations, respectively.

Taking into account the results of both ^{57}Fe and ^{119}Sn Mössbauer spectroscopic measurements, it can be stated that milling of the Fe_2O_3/SnO mixture initiates a *reduction-*

oxidation (the so-called *redox*) reaction, resulting in the *formation of composites* containing FeO, Fe_3O_4, Fe_2O_3, SnO_2, and SnO phases. In ideal case, the redox reaction between Fe_2O_3 and SnO could be described in the following manner: $Fe_2O_3 + SnO \rightarrow 2\,FeO + SnO_2$.

The results of Mössbauer measurements were supported by an XRD phase analysis of the Fe_2O_3/SnO mixtures milled for 0 and 20 h, see Fig. 4.28. In agreement with the above spectroscopic results, the initial mixture contains only two phases: SnO (JCPDS # 6-395) and α-Fe_2O_3 (JCPDS # 33-664). The mixture milled for 20 h is found to contain the following five phases: SnO (JCPDS # 06-0395), α-Fe_2O_3 (JCPDS # 33-0664), Fe_3O_4 (JCPDS # 19-0629), FeO (JCPDS # 46-1312), and SnO_2 (JCPDS # 41-1445).

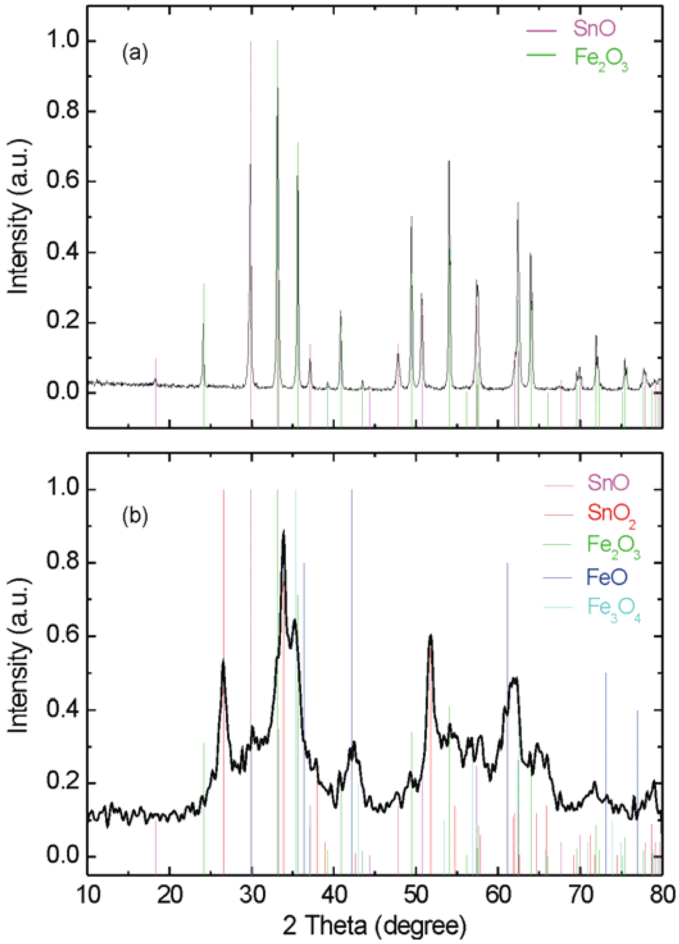

Fig. 4.28. XRD patterns of (a) the initial Fe_2O_3/SnO mixture and (b) the composite prepared by mechanochemical redox reaction.

The broad shape of the XRD lines corresponding to the composite indicates its nanoscale nature, i.e., a so-called *nanocomposite* is formed by mechanochemical redox reaction. The particle size of the nanocomposite was analyzed by HR-TEM, see Fig. 4.29. It was revealed that the average particles size of nanocomposite is below 10 nm.

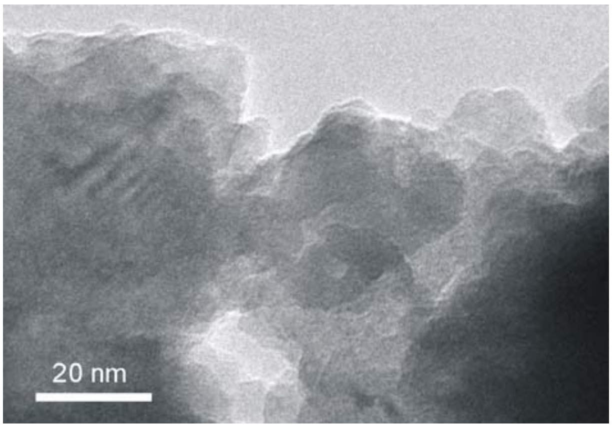

Figure 4.29. TEM image demonstrating the nanoscale nature of the Sn-oxide/Fe-oxide composite prepared by mechanochemical redox reaction (t_m = 20 h).

In the following, mechanochemical decomposition reactions of nanohexaferrite ($SrFe_{12}O_{19}$) and olivine (Fe_2SiO_4) phases are presented. It was observed that the prolonged high-energy milling ($t_m > 4$ h) of nanocrystalline ($D = 8$ nm) $SrFe_{12}O_{19}$, that was previously prepared by homogeneous mechanochemical reaction (see Fig. 3.9), leads to its decomposition into the simple nanooxides α-Fe_2O_3 and SrO with an average particle size of 8 nm, see Figs. 4.30 and 4.31. Thus, the following mechanochemical decomposition reaction takes place: $SrFe_{12}O_{19} \rightarrow 6\ \alpha\text{-}Fe_2O_3 + SrO$. Note that although the formed α-Fe_2O_3 particles are in the nanoscale range, similarly as in the case of $SrFe_{12}O_{19}$, the corresponding room-temperature ^{57}Fe Mössbauer spectra of both nanomaterials do not show a superparamagnetic doublet. As already mention in the Section 3.3, this is due to a relatively low value of the magnetic anisotropy constant, which determines the relaxation time of the superparamagnetic phenomenon.

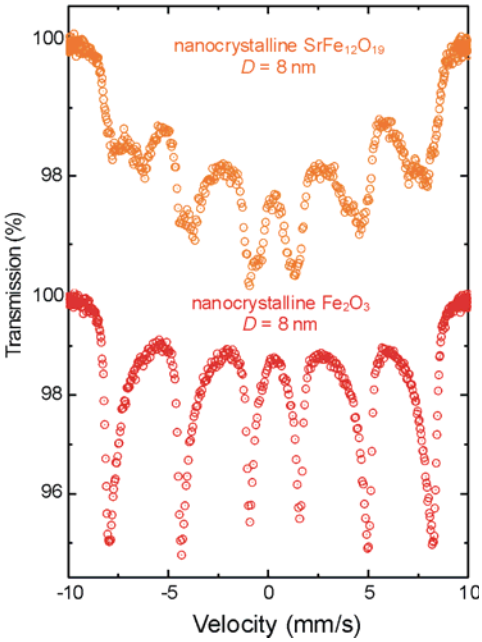

Figure 4.30. The room-temperature Mössbauer spectra of (top, t_m = 4 h) nanocrystalline $SrFe_{12}O_{19}$ and (bottom, t_m = 6 h) the products of its mechanochemical decomposition.

Figure 4.31 shows the morphology of both nanocrystalline $SrFe_{12}O_{19}$ and one of the products (α-Fe_2O_3) of its mechanochemical decomposition. As seen, the lattice fringes cross the whole Fe_2O_3 nanoparticle, demonstrating its single-crystalline character. The corresponding SAED patterns (see Fig. 4.32) confirm the presence of pure $SrFe_{12}O_{19}$ phase (JCPDS # 33-1340) and of α-Fe_2O_3 (JCPDS # 33-0664) in the initial and final stages of the present mechanochemical decomposition reaction, respectively.

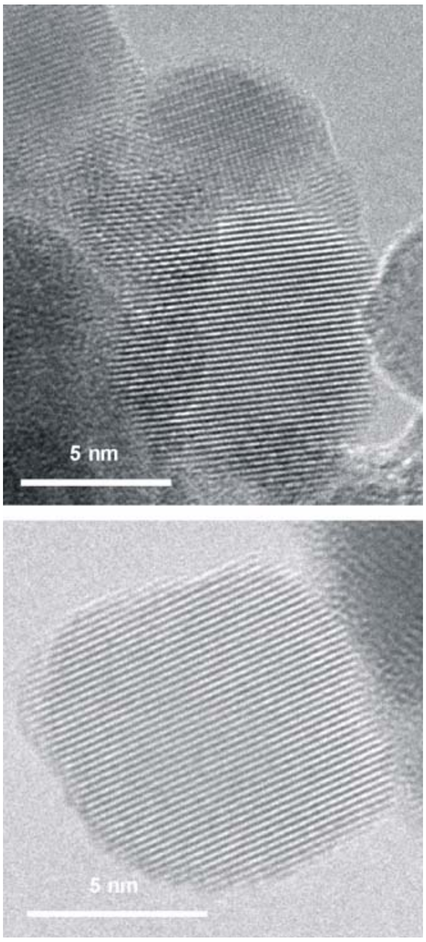

Figure 4.31. HR-TEM images of (top, $t_m = 4$ h) nanocrystalline $SrFe_{12}O_{19}$ and (bottom, $t_m = 6$ h) one of the products (Fe_2O_3) of its mechanochemical decomposition.

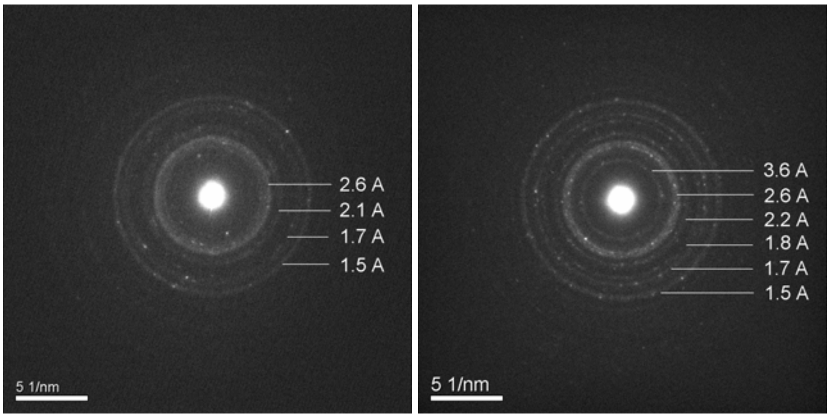

Figure 4.32. SAED patterns of (left) nanocrystalline $SrFe_{12}O_{19}$ and (right) one of the products (Fe_2O_3) of its mechanochemical decomposition.

The mechanically induced phase evolution of nanocrystalline Fe_2SiO_4, that was previously prepared by heterogeneous mechanochemical formation reaction (see Figs. 4.17 and 4.20), was followed by XRD and Mössbauer spectroscopy. Figures 4.33 and 4.34 clearly demonstrate that prolonged milling of nanocrystalline Fe_2SiO_4 leads to its chemical decomposition with the formation of α-Fe_2O_3. Since no other phase was detected in the final powdered product of the reaction by XRD (see Fig. 4.33), it can be assumed that some Si-containing phase (e.g., SiO_2) is in an amorphous state and/or in the form of thin layers covering the α-Fe_2O_3 nanoparticles. Similar morphology has already been observed in [195-197], where the processing of SiO_2 and Fe_2O_3 resulted in the formation of SiO_2-Fe_2O_3 nanocomposite where Fe_2O_3 nanoparticles are surrounded by an amorphous SiO_2 matrix.

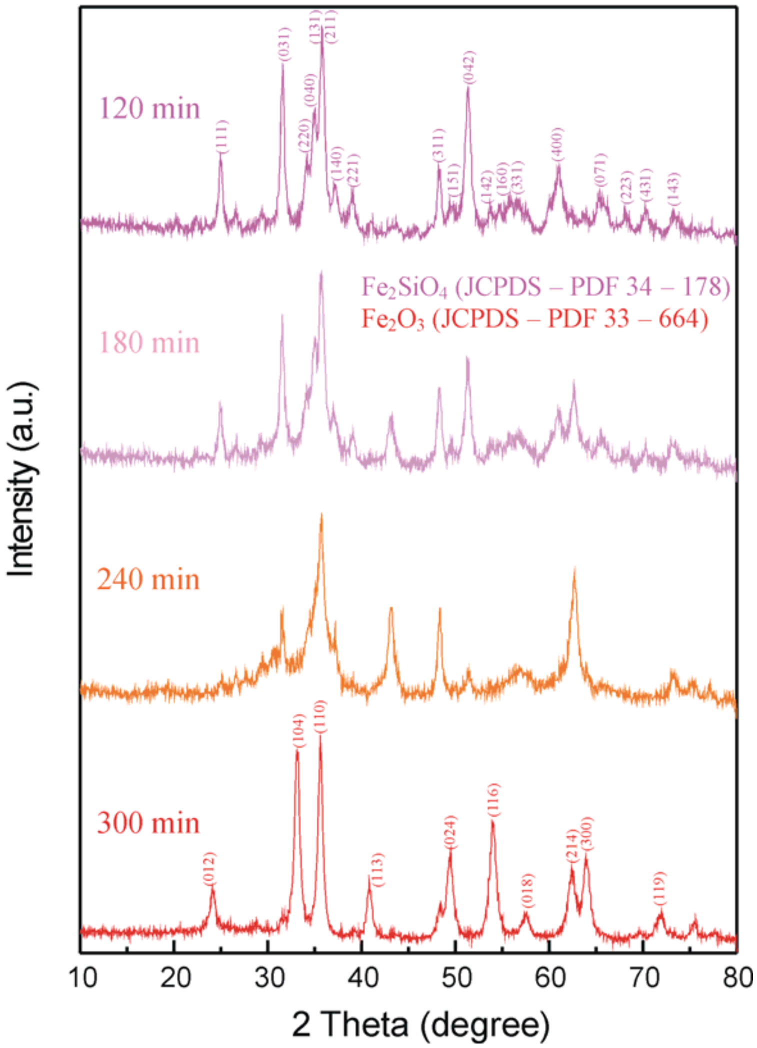

Figure 4.33. XRD patterns illustrating the progress of the mechanochemical decomposition of nanocrystalline Fe_2SiO_4. The milling times are indicated in the figure. Miller indices of the initial Fe_2SiO_4 phase and of the final Fe_2O_3 product are also shown.

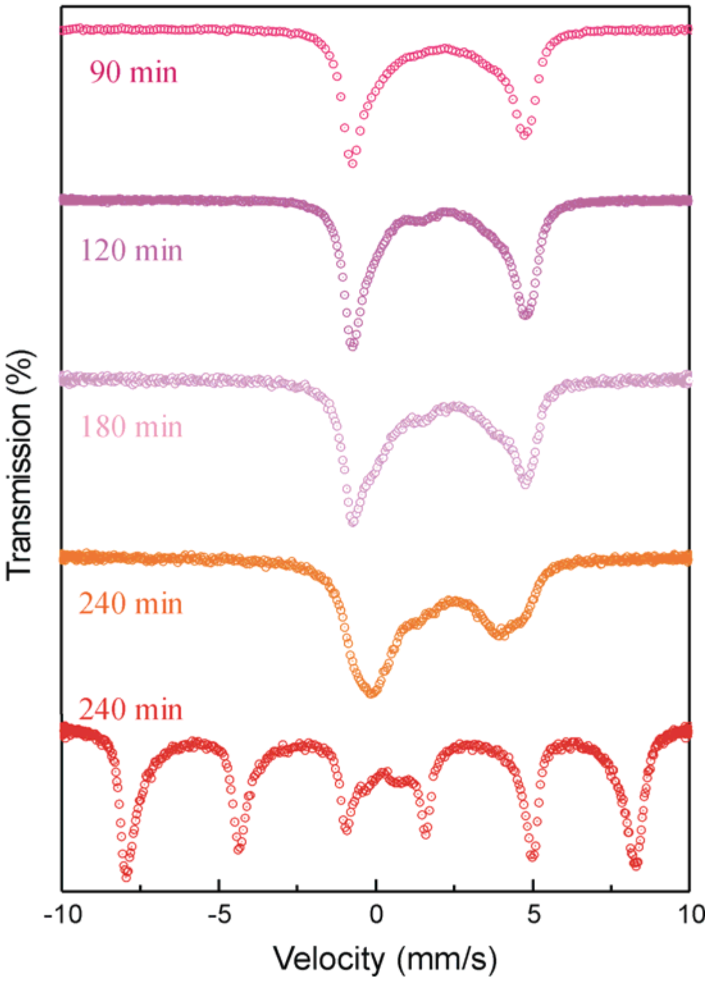

Figure 4.34. Room-temperature Mössbauer spectra illustrating the progress of the mechanochemical decomposition of nanocrystalline Fe_2SiO_4. The milling times are indicated in the figure.

It should be noted that the reason for the instability of the hexagonal ferrite and olivine nanophases under prolonged mechanochemical treatment is not understood at present. To conclude, the identification of the factors representing the main driving force for mechanically induced redox and decomposition processes, the elucidation of the microscopic mechanism(s), and the determination of rate determining steps of mechanochemical reactions represent major challenges for fundamental research and require further efforts.

5. Summary

The preparation of nanocrystalline complex oxides based on mechanochemical methods is a rapidly expanding area of solid state science. Taking into account that the conventional solid-state (ceramic) route to oxides requires a number of steps, including homogenization of the powder precursors, compaction of the reactants, and finally prolonged heat treatment at considerably elevated temperatures under controlled oxygen fugacity, the nonconventional one-step mechanochemical route can be considered as a powerful, simple and energy-saving method for the production of nanooxides. The mechanochemical processing provides an opportunity to fabricate novel nanomaterials with anomalous properties different from those of bulk samples prepared by the conventional ceramic processing. The Thesis deals with nanocrystalline complex oxides prepared by mechanochemical reactions. In accord with the aims of the Thesis given on page 6, the results obtained can be summarized as follows:

- Nanocrystalline oxides ($BaFe_{12}O_{19}$, $SrFe_{12}O_{19}$, $Mn_{0.5}Zn_{0.5}Fe_2O_4$, $CaFe_2O_4$, Fe_2SiO_4, $FeMgSiO_4$, Mg_2SiO_4, FeO-SnO_2 composites) were prepared via one-step homogeneous and heterogeneous mechanochemical reactions. It was demonstrated that various types of reactions can be induced by mechanical treatment, including mechanochemical formation reactions, mechanochemical redox reactions, and mechanochemical decomposition reactions.
- In the context of homogeneous mechanochemical processes, the structures of the initial (bulk) *M*-type hexaferrites $BaFe_{12}O_{19}$ and $SrFe_{12}O_{19}$ were refined. On the basis of Rietveld analysis the exact coordinates of atoms, the unit cell dimensions as well as the interatomic distances and angles in $BaFe_{12}O_{19}$ and $SrFe_{12}O_{19}$ were determined. ^{57}Fe Mössbauer spectroscopy provided detailed insight into the local atomic structure of the hexaferrites, including quantitative information on their hyperfine parameters.
  - The mechanochemical processing of the hexaferrites leads to a decrease of their average crystallite size from 220 nm to the lower nanometer range (~ 10 nm). The ferrite nanoparticles possess the core–shell configuration consisting of an ordered inner core surrounded by a disordered interface/surface shell region with a thickness of about 2 nm. It was shown that the crystallite size reduction of the hexaferrites is accompanied by a transition of Fe^{3+} cations from 12k sites into interstitial positions.
  - The nonequilibrium cation distribution in hexaferrites effects their spin arrangement and results in the formation of canted magnetic structures. Taking into account the core–shell configuration of hexaferrite nanoparticles, it can be assumed that both nonequilibrium cation distribution and spin canting are located in the interface/surface shell regions of the nanomaterials. These mechanically induced changes in the atomic and spin structures lead to a considerable reduction of the effective magnetic moment of hexaferrites, i.e., to the formation of magnetically “dead” regions. It was shown that the volume fraction of the interface/surface shell regions reaches up to 64%. Consequently, it was demonstrated that the saturation magnetization of the hexaferrites decreases with decreasing crystallite size.

Moreover, the nanoscale mechanically activated $BaFe_{12}O_{19}$ and $SrFe_{12}O_{19}$ hexaferrites exhibit enhanced and reduced magnetic hardness, respectively. This behavior is explained by a decrease of the magnetic anisotropy constant of the materials with decreasing particle size, which in turn changes with the decreasing occupation of Fe^{3+} ions in the 12k positions of hexaferrites.

- In respect to heterogeneous mechanochemical processes, the single-step mechanosynthesis of nanocrystalline $Mn_{0.5}Zn_{0.5}Fe_2O_4$ with the spinel structure, of $CaFe_2O_4$ with the orthorhombic structure as well as of $(Fe_{1-x}Mg_x)_2SiO_4$ ($x = 0$, 0.5 and 1) with the olivine structure is reported. Furthermore, it is demonstrated that oxide-oxide nanocomposites (FeO-SnO_2, SrO-Fe_2O_3, SiO_2-Fe_2O_3) can be produced by mechanochemical redox and decomposition reactions.
  - Low-temperature in-field ^{57}Fe Mössbauer measurements revealed that atomic and spin configurations in the mechanosynthesized $Mn_{0.5}Zn_{0.5}Fe_2O_4$ spinel (with an average crystallite size of about 14 nm) are characterized by a nonequilibrium cation distribution of the type $(Zn_{0.44}Fe_{0.56}\searrow)[Zn_{0.06}Mn_{0.50}Fe_{1.44}\nearrow]O_4$ as well as by a noncollinear spin alignment ($\Psi_{(A)} = 22.6°$, $\Psi_{[B]} = 24.0°$), respectively. The enhanced Néel temperature (583 K) observed for the mechanosynthesized material, in comparison with that of bulk $Mn_{0.5}Zn_{0.5}Fe_2O_4$ (413 K), is attributed to the strengthening of the (A)-O-[B] superexchange interaction due to a higher concentration of magnetic ions on (A) sites. The saturation magnetization of mechanosynthesized $Mn_{0.5}Zn_{0.5}Fe_2O_4$ is about 1.7 times smaller than that of the bulk material. This magnetic degradation is attributed to both the nonequilibrium cation distribution and the noncollinear spin effects in the surface shell of $Mn_{0.5}Zn_{0.5}Fe_2O_4$ nanoparticles.
  - Based on the results of both Mössbauer spectroscopic measurements and Rietveld analysis of XRD data, the crystal chemical formula of the nanocrystalline mechanosynthesized $CaFe_2O_4$ with orthorhombic structure and of $(Fe_{1-x}Mg_x)_2SiO_4$ ($x = 0$, 0.5 and 1) with olivine structure, can be written as $Ca[Fe]_{oct1}[Fe]_{oct2}O_4$ and $[Fe_{(1-x)/2}Mg_{x/2}]_{M1}[Fe_{(1-x)/2}Mg_{x/2}]_{M2}SiO_4$, respectively. Here, the brackets enclose Fe cations in crystallographically nonequivalent octahedra. In the case of the silicate system, a comparative Mössbauer study of bulk and nanosized Fe_2SiO_4 enabled us both to separate the surface effects from the bulk effects in mechanosynthesized nanoparticles and to reveal the presence of distorted octahedra. Taking into account the core–shell configuration of the mechanosynthesized $CaFe_2O_4$ and $(Fe_{1-x}Mg_x)_2SiO_4$ nanoparticles, evidenced by HRTEM, it can be assumed that distorted octahedra are located in the interface/surface regions of nanoparticles.
  - The mechanochemical processing of a Fe_2O_3/SnO mixture initiates a reduction-oxidation reaction, resulting in the formation of FeO-SnO_2 nanocomposite with an average crystallite size of about 10 nm. The prolonged mechanical treatment of both nanocrystalline $SrFe_{12}O_{19}$ and Fe_2SiO_4 leads to their chemical decomposition with the formation of SrO-Fe_2O_3 and SiO_2-Fe_2O_3 nanocomposites, respectively. In the latter case, it can be assumed that SiO_2 is in an amorphous state and/or that it forms thin layers covering the α-Fe_2O_3 nanoparticles.

References

[1] Published later: P. R. Feynman, *Miniaturization*. Reinhold, New York, 1961.

[2] S. H. Cohen, M. L. Lightbody, *Atomic Force Microscopy/Scanning Tunneling Microscopy 2.* Kluwer Academic/Plenum Publishers, Dordrecht, 1997.

[3] G. D. Stucky, J. E. Mac Dougall, Quantum confinement and host/guest chemistry: Probing a new dimension. *Science* 247 (1990) 669.

[4] National Science Foundation Homepage at http://www.nsf.gov/nano/

[5] A. S. Edelstein, R. C. Cammarata (Eds.), *Nanomaterials: synthesis, properties and applications.* IOP Publishing Ltd., London, 2002.

[6] J. A. Rodríguez, M. Fernández-García (Eds.), *Synthesis, properties, and applications of oxide nanomaterials.* John Wiley & Sohns, Hoboken, New Jersey, 2007.

[7] E. G. Avvakumov, *Fundamental bases of mechanical activation, mechanosynthesis and mechanochemical technologies.* Publishing House of the Siberian Branch of the Russian Academy of Sciences, Novosibirsk, 2009 (in Russian).

[8] Proceedings of the 14th International Symposium on Metastable and Nano-Materials, August 26-30, 2007, Corfu, Greece.

[9] H. Gleiter, In: *Deformation of Polycrystals: Mechanism and Microstructures*, N. Hansen *et al.* (Eds.), Risø National Laboratory, Roskilde, 1981, p. 15.

[10] C. Suryanarayana, Nanocrystalline materials. *Int. Mater. Rev.* 40 (1995) 41.

[11] V. Šepelák, K. D. Becker, Z. A. Munir (Eds.), *Mechanochemistry and Mechanical Alloying 2003.* Kluwer Academic Publishers, Boston, 2004 [in: *J. Mater. Sci.* 39 (2004) pp. 4983-5530].

[12] http://www.fritsch.de.

[13] L. Takacs, M. Carey Lea, the first mechanochemist. *J. Mater. Sci.* 39 (2004) 4987.

[14] W. Ostwald, *Handbuch der Allgemeinen Chemie.* Akademische Verlagsgesellschaft, Leipzig, 1919, p.70.

[15] G. Heinicke, *Tribochemistry.* Akademie-Verlag, Berlin, 1984.

[16] A. Smékal, Ritzvorgang und molekulare Festigkeit. *Naturwissenschaften* 30 (1942) 224.

[17] K**.** Tkáčová, *Mechanical Activation of Minerals.* Elsevier, Amsterdam, 1989.

[18] G. S. Khodakov, Sorption mechanochemistry of solid inorganic materials. *Colloid Journal* 56 (1994) 113 (in Russian).

[19] J. S. Benjamin, Dispersion strengthened superalloys by mechanical alloying. *Metall. Trans.* 1 (1970) 2943.

[20] J. S. Benjamin, In: *Advances in Powder Metallurgy and Particulate Materials*, E. D. Capus, R. M. German (Eds.), Metal Powder Industries Federation, Princeton, 1970, Vol. 7, p. 155.

[21] C. Suryanarayana, F. H. Froes, Nanocrystalline titanium-magnesium alloys through mechanical alloying. *J. Mater. Res.* 5 (1990) 1880.

[22] V. Šepelák, I. Bergmann, S. Kipp, K. D. Becker, Nanocrystalline ferrites prepared by mechanical activation and mechanosynthesis. *Z. Anorg. Allg. Chem.* 631 (2005) 993.

[23] V. Šepelák, K. D. Becker, I. Bergmann, S. Suzuki, S. Indris, A. Feldhoff, P. Heitjans, C. P. Grey, A one-step mechanochemical route to core-shell Ca_2SnO_4 nanoparticles followed by ^{119}Sn MAS NMR and ^{119}Sn Mössbauer spectroscopy. *Chem. Mater.* 21 (2009) 2518.

[24] M. Radwan, M. M. Rashad, M. M. Hessien, Synthesis and characterization of barium hexaferrite nanoparticles. *J. Mater. Process. Tech.* 181 (2007) 106.

[25] H. Schmalzried, *Solid State Reactions.* Verlag Chemie, Weinheim, 1981.

[26] V. V. Boldyrev, In: *Proceedings of the First International Conference on Mechanochemistry. Part 1.* K. Tkáčová (Ed.), Cambridge International Science Publishing, Cambridge, 1994, p. 18.

[27] E. M. Gutman, *Mechanochemistry of Materials.* Cambridge International Science Publishing, Cambridge, 1998.

[28] P. Baláž, *Extractive Metallurgy of Activated Minerals.* Elsevier, Amsterdam, 2000.

[29] S. J. Campbell, W. A. Kaczmarek, In: *Mössbauer Spectroscopy Applied to Magnetism and Materials Science. Vol. 2.* G. J. Long, F. Grandjean (Eds.), Plenum Press, New York, 1996, p. 273.

[30] A. N. Streletskii, In: *Proceedings of the 2nd International Conference on the Structural Applications of Mechanical Alloying.* J. J. de Barbadillo, F. H. Froes, R. Schwarz (Eds), ASM, Materials Park, Ohio, 1993, p. 51.

[31] L. Takacs, V. Šepelák, Quantitative comparison of the efficiency of mechanochemical reactors. *J. Mater. Sci.* 39 (2004) 5487.

[32] G. A. Sawatzky, F. Van Der Woude, A. H. Morrish, Mössbauer study of several ferrimagnetic spinels. *Phys. Rev.* 187 (1969) 747.

[33] M. Eibschütz, S. Shtrikman, Restoration of motionally narrowed hyperfine splitting in superparamagnetic particles by magnetic field. *J. Appl. Phys.* 39 (1968) 997.

[34] K. Lagarec, D. G. Rancourt, *Recoil - Mössbauer Spectral Analysis Software for Windows, version 1.02*; Department of Physics, University of Ottawa: Ottawa, 1998.

[35] G. A. Sawatzky, F. Van Der Woude, A. H. Morrish, Recoilless-fraction ratios for Fe^{57} in octahedral and tetrahedral sites of a spinel and a garnet. *Phys. Rev.* 183 (1969) 383.

[36] M. P. Morales, S. J. Serna, F. Bødker, S. Mørup, Spin canting due to structural disorder

in maghemite. *J. Phys. Condens. Matter* 9 (1997) 5461.

[37] R. A. Young, *The Rietveld Method.* Oxford University Press, Oxford, 1993.

[38] H. M. Rietveld, Profile refinement method for nuclear and magnetic structures. *J. Appl. Crystallogr.* 2 (1969) 65.

[39] G. Malmros, J. O. Thomas, Least-squares structure refinement based on profile analysis of powder film intensity data measured on an automatic microdensitomer. *J. Appl. Crystallogr.* 10 (1977) 7.

[40] The database *"Structure Determination from Powder Diffraction"* is accessible on http://www.cristal.org/iniref.html

[41] W. Kraus, G. Nolze, *PowderCell for Windows, version 2.4*; Federal Institute for Materials Research and Testing: Berlin, 2000.

[42] Joint Committee on Powder Diffraction Standards (JCPDS) Powder Diffraction File (PDF), PDF-2, Sets 1-47, International Centre for Diffraction Data, USA, 2004.

[43] R. A. Young, D. B. Wiles, Profile shape functions in Rietveld refinements. *J. Appl. Cryst.* 15 (1982) 430.

[44] L. Néel, Magnetic properties of ferrites: ferromagnetism and antiferromagnetism. *Ann. Phys*. 3 (1948) 137.

[45] C. G. Shull, E. O. Wollan, W. C. Koehler, Neutron Scattering and Polarization by Ferromagnetic Materials. *Phys. Rev.* 84 (1951) 912.

[46] R. Valenzuela, In: *Magnetic Ceramics.* Cambridge University Press, Cambridge, 1994.

[47] P. W. Anderson, In: *Magnetism,* G. T. Rado, H. Suhl (Ed.), Academic Press, New York (1963) 29.

[48] I. S. Jacobs, C. P. Bean, In: *Magnetism.* G. T. Rado, H. Suhl (Ed.), Academic Press, New York (1963) 271.

[49] S. Mørup, In: *Mössbauer Spectroscopy Applied to Inorganic Chemistry*, G. J. Long (Ed.), Plenum Press, New York, 1987, Vol. 2, p. 89.

[50] R. H. Kodama, A. E. Berkowitz, Atomic-scale magnetic modeling of oxide nanoparticles. *Phys. Rev. B* 59 (1999) 6321.

[51] J. L. Dormann, The phenomenon of superparamagnetism. *Rev. Phys. Appl.* 16 (1981) 275.

[52] A. H. Morrish, K. Haneda, Surface magnetic properties of fine particles. *J. Magn. Magn. Mater.* 35 (1983) 105.

[53] F. Bødker, M. F. Hansen, C. B. Koch, K. Lefmann, S. Mørup, Magnetic properties of hematite nanoparticles. *Phys. Rev. B* 61 (2000) 6826.

[54] W. J. Schuele, S. Shtrikman, D. Treves, Observation of superparamagnetism by the Mössbauer effect. *J. Appl. Phys.* 36 (1965) 1010.

[55] M. Eibschütz, S. Shtrikman, Restoration of motionally narrowed hyperfine splitting in superparamagnetic particles by magnetic field. *J. Appl. Phys.* 39(1968) 997.

[56] W. F. Brown, Jr., Thermal fluctuations of a single-domain particle. *Phys. Rev.* 130 (1963) 1677.

[57] I. Eisenstein and A. Aharoni, Asymptotic superparamagnetic time constants for cubic anisotropy. I. Positive anisotropy *Phys. Rev. B* 16 (1977) 1278.

[58] G. S. Agarwal, S. Dattagupta, K. P. Murthy, Relaxation behaviour of single-domain magnetic particles *J. Phys. C* 17 (1984) 6869.

[59] V. Šepelák and K. D. Becker, Mechanically induced disorder in magnesium ferrite. *J. Metastable Nanocryst. Mater.* 8 (2000) 332.

[60] V. Šepelák, K. Tkáčová, V. V. Boldyrev, S. Wißmann, K. D. Becker, Mechanically induced cation redistribution in $ZnFe_2O_4$ and its thermal stability. *Physica B* 234-236 (1997) 617.

[61] V. Šepelák, S. Wißmann, K. D. Becker, A temperature-dependent Mössbauer study of mechanically activated and non-activated zinc ferrite. *J. Mater. Sci.* 33 (1998) 2845.

[62] S. Mørup, J. A. Dumesic, H. Topsøe, In: *Application of Mössbauer Spectroscopy.* Vol. II. R. L. Cohen (Ed.) Academic Press, New York, 1980, p. 1.

[63] S. Mørup, Magnetic hyperfine splitting in mössbauer spectra of microcrystals. *J. Magn. Magn. Mater.* 37 (1983) 39.

[64] R. E. Vandenberghe, E. De Grave, In: *Mössbauer Spectroscopy Applied to Inorganic Chemistry*, G. J. Long, F. Grandjean (Eds.), Plenum Press, New York, 1989, Vol. 3, p. 59.

[65] D. P. E. Dickson, F. J. Berry, *Mössbauer Spectroscopy.* Cambridge University Press, Cambridge, 1986.

[66] E. Paimozd, A. Ghasemi, A. Jafari, H. Sheikh, Influence of acid catalysts on the structural and magnetic properties of nanocrystalline barium ferrite prepared by sol–gel method. *J. Magn. Magn. Mater.* 320 (2008) L137.

[67] H. M. Lee, S.-Y. Bae, J.-H. Yu, Y.-J. Kim, Preparation of unsintered spherical $BaFe_{12}O_{19}$ nanoparticles via an alcohol-assisted spray-pyrolysis route. *J. Am. Ceram. Soc.* 91 (2008) 2856.

[68] L. P. Ol'khovik, Z. I. Sizova, Investigation of temperature dependence of surface anisotropy field and constant in the system of $BaFe_{12}O_{19}$ nanocrystals. *J. Magn. Magn. Mater.* 320 (2008) 2190.

[69] M. Drofenik, M. Kristl, A. Žnidaršič, D. Hanžel, D. Lisjak, Hydrothermal synthesis of Ba-hexaferrite nanoparticles. *J. Am. Ceram. Soc.* 90 (2007) 2057.

[70] P. Xu, X. Han, M. Wang, Synthesis and magnetic properties of $BaFe_{12}O_{19}$ hexaferrite nanoparticles by a reverse microemulsion technique. *J. Phys. Chem. C* 111 (2007) 5866.

[71] S. V. Ketov, Yu. D. Yagodkin, A. L. Lebed, Yu. V. Chernopyatova, K. Khlopkov, Structure and magnetic properties of nanocrystalline $SrFe_{12}O_{19}$ alloy produced by high-energy ball milling and annealing. *J. Magn. Magn. Mater.* 300 (2006) e479.

[72] J. Wang, C. Zeng, Growth of $SrFe_{12}O_{19}$ nanowires under an induced magnetic field. *J. Cryst. Growth* 270 (2004) 729.

[73] C. M. Fang, F. Kools, R. Metselaar, G. de With, R. A. de Groot, Magnetic and electronic properties of strontium hexaferrite $SrFe_{12}O_{19}$ from first-principles calculations. *J. Phys. Condens. Matter* 15 (2003) 6229.

[74] S. W. Lee, S. Y. An, S. J. Kim, I.-B. Shim, C. S. Kim, The annealing temperature dependence of magnetic properties in Sr-ferrite nanoparticles. *IEEE T. Magn.* 39 (2003) 2899.

[75] V. Berbenni, A. Marini, Solid state synthesis of strontium oxoferrates from the mechanically activated system $SrCO_3$-Fe_2O_3. *Mater. Res. Bull.* 37 (2002) 221.

[76] S. Chaudhury, S. K. Rakshit, S. C. Parida, Z. Singh, K. D. S. Mudher, V. Venugopal, Studies on structural and thermo-chemical behaviour of $MFe_{12}O_{19}(s)$ (M = Sr, Ba and Pb) prepared by citrate–nitrate gel combustion method. *J. Alloy. Compd.* 455 (2008) 25.

[77] Z. F. Zi, Y. P. Sun, X. B. Zhu, Z. R. Yang, J. M. Dai, W. H. Song, Structural and magnetic properties of $SrFe_{12}O_{19}$ hexaferrite synthesized by a modified chemical co-precipitation method. *J. Magn. Magn. Mater.* 320 (2008) 2746.

[78] P. C. A. Brito, R. F. Gomes, J. G. S. Duque, M. A. Macêdo, $SrFe_{12}O_{19}$ prepared by the proteic sol–gel process. *Physica B* 384 (2006) 91.

[79] S. Singhal, K. Chandra, Magnetic and Mössbauer spectral studies of x ($NiFe_2O_4$) + ($1-x$) ($SrFe_{12}O_{19}$), $x = 0, 0.2, 0.4, 0.6, 0.8$ and 1.0 nanocomposites. *Hyperfine Interact.* 183 (2008) 93.

[80] D. Bellušova, T. Alshuth, R. H. Schuster, M. Myndyk, V. Šepelak, I. Hudec, Influence of barium ferrites on the performance of BR-elastomers. *KGK Kautschuk Gummi Kunststoffe* 61 (2008) 118.

[81] (a) R. L. Mössbauer, Nuclear resonance absorption of γ-rays in iridium-191. *Naturwissenschaften* 45 (1958) 538; (b) R. L. Mössbauer, Nuclear resonance absorption of γ-radiation in iridium-191. *Z. Naturforsch.* 14a (1959) 211.

[82] F. Menil, Systematic trends of the 57Fe Mössbauer isomer shifts in (FeO_n) and (FeF_n) polyhedra. Evidence of a new correlation between the isomer shift and the inductive effect of the competing bond T-X (→ Fe) (where X is O or F and T any element with a formal positive charge). *J. Phys. Chem. Solids* 46 (1985) 763.

[83] F.-M. Gao, D.-C. Li, S.-Y. Zhang, Mössbauer spectroscopy and chemical bonds in $BaFe_{12}O_{19}$ hexaferrite. *J. Phys. Condens. Matter* 15 (2003) 5079.

[84] J.-M. Greneche, Grain boundaries in magnetic nanostructured systems. *Czech. J. Phys.* 52 (2002) 139.

[85] H. Bunge, J. Fiala, R. L. Snyder, *Microstructure Analysis by Diffraction.* IUCr/Oxford University Press, Oxford, 1999.

[86] G. Salazar-Alvarez, J. Qin, V. Šepelák, I. Bergmann, M. Vasilakaki, K. N. Trohidou, J. D. Ardisson, W. A. A. Macedo, M. Mikhaylova, M. Muhammed, M. D. Baró, J. Nogués, Cubic versus spherical magnetic nanoparticles: The role of surface anisotropy. *J. Am. Chem. Soc.* 130 (2008) 13234.

[87] G. A. Ozin, A. C. Arsenault, L. Cademartiri, *Nanochemistry, A Chemical Approach to Nanomaterials*. RSC Publishing, Cambridge, 2009.

[88] Q. Song, Z. J. Zhang, Shape control and associated magnetic properties of spinel cobalt ferrite nanocrystals. *J. Am. Chem. Soc.* 126 (2004) 6164.

[89] R. E. Vandenberghe, E. De Grave, In: *Mössbauer Spectroscopy Applied to Inorganic Chemistry*, G. J. Long, F. Grandjean (Eds.), Plenum Press, New York, 1989, Vol. 3, p. 138.

[90] I. Bergmann, V. Šepelák, A. Feldhoff, P. Heitjans, K. D. Becker, Particle size dependent cation distribution in lithium ferrite spinel $LiFe_5O_8$. *Rev. Adv. Mater. Sci.* 18 (2008) 375.

[91] A. A. Bezlepkin, S. P. Kuntsevich, Dipole contribution of Fe^{3+} ions in 12k positions to the anisotropy energy constant of the $BaFe_{12}O_{19}$ hexaferrite. *Phys. Solid State* 43 (2001) 1260.

[92] J. P. J. Groenland, J. H. J. Fluitman, Measurement system for two-dimensional magnetic field distributions, applied to the investigation of recording head fields. *J. Phys. E: Sci. Instrum.* 14 (1981) 503.

[93] N. S. Gajbhiye, G. Balaji, M. Ghafari, Magnetic properties of nanostructured $MnFe_2O_4$ synthesized by precursor technique. *Phys. Status Solidi A* 189 (2002) 357.

[94] A. Pantelouris, H. Modrow, M. Pantelouris, J. Hormes, D. Reinen, The influence of coordination geometry and valency on the Cr K-edge XANES spectra of selected chromium compounds. *Chem. Phys.* 300 (2004) 13.

[95] M. George, A. M. John, S. S. Nair, P. A. Joy, M. R. Anantharaman, Finite size effects on the structural and magnetic properties of sol–gel synthesized $NiFe_2O_4$ powders. *J. Magn. Magn. Mater.* 302 (2006) 190.

[96] V. Šepelák, I. Bergmann, A. Feldhoff, P. Heitjans, F. Krumeich, D. Menzel, F. J. Litterst, S. J. Campbell, K. D. Becker, Nanocrystalline nickel ferrite, $NiFe_2O_4$: mechanosynthesis, nonequilibrium cation distribution, canted spin arrangement, and magnetic behavior. *J. Phys. Chem. C* 111 (2007) 5026.

[97] R. H. Kodama, A. E. Berkowitz, E. J. McNiff, S. Foner, Surface spin disorder in ferrite nanoparticles. *J. Appl. Phys.* 81 (1997) 5552.

[98] R. H. Kodama, A. E. Berkowitz, Atomic-scale magnetic modeling of oxide nanoparticles. *Phys. Rev. B* 59 (1999) 6321.

[99] V. Šepelák, I. Bergmann, D. Menzel, A. Feldhoff, P. Heitjans, F. J. Litterst, K. D. Becker, Magnetization enhancement in nanosized $MgFe_2O_4$ prepared by mechanosynthesis. *J. Magn. Magn. Mater.* 316 (2007) e764.

[100] V. Šepelák, A. Feldhoff, P. Heitjans, F. Krumeich, D. Menzel, F. J. Litterst, I. Bergmann, K. D. Becker, Nonequilibrium cation distribution, canted spin arrangement, and enhanced magnetization in nanosized $MgFe_2O_4$ prepared by a one-step mechanochemical route. *Chem. Mater.* 18 (2006) 3057.

[101] M. P. Morales, M. Andres-Vergés, S. Veintemillas-Verdaguer, M. I. Montero, C. J. Serna, Structural effects on the magnetic properties of γ-Fe2O3 nanoparticles. *J. Magn. Magn. Mater.* 203 (1999) 146.

[102] M. V. Kuznetsov, Q. A. Pankhurst, I. P. Parkin, Novel SHS routes to CoTi-doped M-type ferrites. *J. Mater. Sci.* 12 (2001) 533.

[103] P.A. Mariňo-Castellanos, J. Anglada-Rivera, A. Cruz-Fuentes, R. Lora-Serrano, Magnetic and microstructural properties of the Ti^{4+} - doped Barium hexaferrites. *J. Magn. Magn. Mater* 280 (2004) 214.

[104] X. Batlle, X. Obradors, M. Medarde, J. Rodríguez-Carvajal, M. Pernet, M. Vallet-Regí, Surface spin canting in $BaFe_{12}O_{19}$ fine particles. *J. Magn. Magn. Mater.* 124 (1993) 228.

[105] V. Šepelák, D. Baabe, F. J. Litterst, K. D. Becker, Structural disorder in the high-energy milled magnesium ferrite. *J. Appl. Phys.* 88 (2000) 5884.

[106] V. Šepelák, D. Schultze, F. Krumeich, U. Steinike, K. D. Becker, Mechanically induced cation redistribution in magnesium ferrite and its thermal stability. *Solid State Ionics* 141-142 (2001) 677.

[107] V. Šepelák, D. Baabe, D. Mienert, D. Schultze, F. Krumeich, F. J. Litterst, K. D. Becker, Evolution of structure and magnetic properties with annealing temperature in nanoscale high-energy milled nickel ferrite. *J. Magn. Magn. Mater.* 257 (2003) 377.

[108] V. Šepelák, S. Indris, I. Bergmann, A. Feldhoff, K. D. Becker, P. Heitjans, Nonequilibrium cation distribution in nanocrystalline $MgAl_2O_4$ studied by ^{27}Al magic-angle spinning NMR. *Solid State Ionics* 177 (2006) 2487.

[109] S. Weber, *Java Structure Viewer (JSV), 1.08lite*, 1999. Program is accessible on http://www.jcrystal.com/steffenweber/JAVA/JSV/ jsv.html

[110] V. Šepelák, D. Baabe, K. D. Becker, Mechanically induced cation redistribution and spin canting in nickel ferrite. *Journal of Materials Synthesis and Processing* 8 (2000) 333.

[111] S. Ammar, N. Jouini, F. Fiévet, Z. Beji, L. Smiri, P. Moliné, M. Danot, J.-M. Greneche, Magnetic properties of zinc ferrite nanoparticles synthesized by hydrolysis in a polyol medium. *J. Phys. Condens. Matter* 18 (2006) 9055.

[112] N. Ponpandian, A. Narayanasamy, C. N. Chinnasamy, N. Sivakumar, J.-M. Greneche, K. Chattopadhyay, K. Shinoda, B. Jeyadevan, K. Tohji, Néel temperature enhancement in nanostructured nickel zinc ferrite. *Appl. Phys. Lett.* 86 (2005) 192510.

[113] Ö. Helgason, J.-M. Greneche, F. J. Berry, F. Mosselmans, The influence of ruthenium on the magnetic properties of γ-Fe_2O_3 (maghemite) studied by Mössbauer spectroscopy. *J. Phys. Condens. Matter* 15 (2003) 2907.

[114] R. N. Bhowmik, R. Ranganathan, S. Sarkar, C. Bansal, R. Nagarajan, Magnetic enhancement of $Co_{0.2}Zn_{0.8}Fe_2O_4$ spinel oxide by mechanical milling. *Phys. Rev. B* 68 (2003) 134433.

[115] G. F. Goya, E. R. Leite, Ferrimagnetism and spin canting of $Zn^{57}Fe_2O_4$ nanoparticles embedded in ZnO matrix. *J. Phys. Condens. Matter* 15 (2003) 641.

[116] C. Nordhei, A. L. Ramstad, D. G. Nicholson, Nanophase cobalt, nickel and zinc ferrites: Synchrotron XAS study on the crystallite size dependence of metal distribution. *Phys. Chem. Chem. Phys.* 10 (2008) 1053.

[117] V. Sreeja, T. S. Smitha, D. Nand, T. G. Ajithkumar, P. A. Joy, Size dependent coordination behavior and cation distribution in $MgAl_2O_4$ nanoparticles from ^{27}Al solid state NMR studies. *J. Phys. Chem. C* 112 (2008) 14737.

[118] P. Heitjans, M. Masoud, A. Feldhoff, M. Wilkening, NMR and impedance studies of nanocrystalline and amorphous ion conductors. Lithium niobate as a model system. *Faraday Discuss.* 134 (2007) 67.

[119] P. Heitjans, S. Indris, Diffusion and ionic conduction in nanocrystalline ceramics. *J. Phys. Condens. Matter* 15 (2003) R1257.

[120] P. Heitjans, S. Indris, Fast diffusion in nanocrystalline ceramics prepared by ball milling. *J. Mater. Sci.* 39 (2004) 5091.

[121] V. Šepelák, S. Indris, P. Heitjans, K. D. Becker, Direct determination of the cation disorder in nanoscale spinels by NMR, XPS, and Mössbauer spectroscopy. *J. Alloy. Compd.* 434-435 (2007) 776.

[122] M. H. Mahmoud, A. M. Abdallas, H. H. Hamdeh, W. M. Hikal, S. M. Taher, J. C. Ho, Mössbauer spectroscopic evaluation of high-energy ball-milled $CdFe_2O_4$. *J. Magn. Magn. Mater.* 263 (2003) 269.

[123] M. Muroi, R. Street, P. G. McCormick, J. Amighian, Magnetic properties of ultrafine $MnFe_2O_4$ powders prepared by mechanochemical processing. *Phys. Rev. B* 63 (2001) 184414.

[124] Y. D. Zhang, S. H. Ge, H. Zhang, S. Hui, J. I. Budnick, W. A. Hines, M. J. Yacaman, M. Miki, Effect of spin disorder on magnetic properties of nanostructured Ni-ferrite. *J. Appl. Phys.* 95 (2004) 7130.

[125] K. Haneda, A. H. Morrish, Noncollinear magnetic structure of $CoFe_2O_4$ small particles. *J. Appl. Phys.* 63 (1988) 4258.

[126] V. V. Boldyrev, *Reactivity of Solids: Past, Present and Future.* Blackwell Science, Oxford, 1996.

[127] E. Avvakumov, M. Senna, N. Kosova, *Soft Mechanochemical Synthesis: A Basis for New Chemical Technologies*. Kluwer Academic Publishers, Boston, 2001.

[128] V. V. Boldyrev, Mechanochemistry and mechanical activation of solids. *Russ. Chem. Rev.* 75 (2006) 75.

[129] M. J. N. Isfahani, M. Myndyk, V. Šepelák, J. Amighian, A Mössbauer effect investigation of the formation of MnZn nanoferrite phase. *J. Alloy. Compd.* 470 (2009) 434.

[130] V. G. Harris, D. J. Fatemi, J. O. Cross, E. E. Carpenter, V. M. Browning, J. P. Kirkland, A. Mohan, G. J. Long, One-step processing of spinel ferrites via the high-energy ball milling of binary oxides. *J. Appl. Phys.* 94 (2003) 496.

[131] T. Verdier, V. Nivoix, M. Jean, B. Hannoyer, Characterization of nanocrystalline Mn-Zn ferrites obtained by mechanosynthesis. *J. Mater. Sci.* 39 (2004) 5151.

[132] S. Dasgupta, K. B. Kim, J. Ellrich, J. Eckert, I. Manna, Mechano-chemical synthesis and characterization of microstructure and magnetic properties of nanocrystalline $Mn_{1-x}Zn_xFe_2O_4$. *J. Alloy. Compd.* 424 (2006) 13.

[133] M. Mozaffari, F. Ebrahimi, S. Daneshfozon, J. Amighian, Preparation of Mn-Zn ferrite nanocrystalline powders via mechanochemical processing. *J. Alloy. Compd.* 449 (2008) 65.

[134] J. Smit, H. P. J. Wijn, *Ferrites.* Philips Technical Library, 1959.

[135] M. Sugimoto, The past, present, and future of ferrites. *J. Am. Ceram. Soc.* 82 (1999) 269.

[136] R. W. Grimes, A. B. Anderson, A. H. Heuer, Predictions of cation distributions in AB_2O_4 spinels from normalized ion energies. *J. Am. Chem. Soc.* 111 (1989) 1.

[137] V. Šepelák, K. D. Becker, Mössbauer studies in the mechanochemistry of spinel ferrites. *J. Mater. Synth. Process.* 8 (2000) 155.

[138] S. Mørup, In: *Mössbauer Spectroscopy Applied to Inorganic Chemistry*, G. J. Long (Ed.), Plenum Press, New York, 1987, Vol. 2, p. 89.

[139] M. Menzel, V. Šepelák, K. D. Becker, Mechanochemical reduction of nickel ferrite. *State Ionics* 141-142 (2001) 663.

[140] K. Mandal, S. Chakraverty, S. Pan Mandal, P. Agudo, M. Pal, D. Chakravorty, Size-dependent magnetic properties of $Mn_{0.5}Zn_{0.5}Fe_2O_4$ nanoparticles in SiO_2 matrix. *J. Appl. Phys.* 92 (2002) 501.

[141] K. Mandal, S. Pan Mandal, P. Agudo, M. Pal, A study of nanocrystalline (Mn-Zn) ferrite in SiO_2 matrix. *Appl. Surf. Sci.* 182 (2001) 386.

[142] M. J. N. Isfahani, M. Myndyk, D. Menzel, A. Feldhoff, J. Amighian, V. Šepelák, Magnetic properties of nanostructured MnZn ferrite. *J. Magn. Magn. Mater.* 321 (2009) 152.

[143] F. S. Li, L. Wang, J. B. Wang, Q. G. Zhou, X. Z. Zhou, H. P. Kunkel, G. Williams, Site preference of Fe in nanoparticles of $ZnFe_2O_4$. *J. Magn. Magn. Mater.* 268 (2004) 332.

[144] V. Šepelák, Nanocrystalline materials prepared by homogeneous and heterogeneous mechanochemical reactions. *Ann. Chim. Sci. Mater.* 27 (2002) 61.

[145] K. Parekh, R. V. Upadhyay, L. Belova, K. V. Rao, Ternary monodispersed $Mn_{0.5}Zn_{0.5}Fe_2O_4$ ferrite nanoparticles: Preparation and magnetic characterization. *Nanotechnology* 17 (2006) 5970.

[146] N. S. Gajbhiye, Trends in research on nanostructured magnetic materials. *Met. Mater. Process.* 10 (1998) 247.

[147] W. Wolski, E. Wolska, J. Kaczmarek, P. Piszora, Formation of manganese ferrite by modified hydrothermal method. *Phys. Status Solidi A* 152 (1995) K19.

[148] G. J. Long, *Mössbauer Spectroscopy Applied to Inorganic Chemistry.* Plenum Press, New York, 1987, Vol. 2.

[149] R. E. Vandenberghe, E. De Grave, In: *Mössbauer Spectroscopy Applied to Inorganic Chemistry*, G. J. Long, F. Grandjean (Eds.), Plenum Press, New York, 1989, Vol. 3, p. 115.

[150] E. J. Choi, Y. Ahn, K.-C. Song, Mössbauer study in zinc ferrite nanoparticles. *J. Magn. Magn. Mater.* 301 (2006) 171.

[151] P. Druska, U. Steinike, V. Šepelák, Surface structure of mechanically activated and of mechanosynthesized zinc ferrite. *J. Solid State Chem.* 146 (1999) 13.

[152] V. Šepelák, K. D. Becker, I. Bergmann, S. Suzuki, S. Indris, A. Feldhoff, P. Heitjans, C. P. Grey, A one-step mechanochemical route to core–shell Ca_2SnO_4 nanoparticles followed by ^{119}Sn MAS NMR and ^{119}Sn Mössbauer spectroscopy. *Chem. Mater.* 21 (2009) 2518.

[153] A. H. Morrish, P. E. Clark, High-field Mössbauer study of manganese-zinc ferrites. *Phys. Rev. B* 11 (1975) 278.

[154] A. Yang, C. N. Chinnasamy, J. M. Greneche, Y. Chen, S. D. Yoon, K. Hsu, C. Vittoria, V. G. Harris, Large tunability of Néel temperature by growth-rate-induced cation inversion in Mn-ferrite nanoparticles. *Appl. Phys. Lett.* 94 (2009) 113109.

[155] N. Sivakumar, A. Narayanasamy, N. Ponpandian, J.-M. Greneche, K. Shinoda, B. Jeyadevan, K. Tohji, Effect of mechanical milling on the electrical and magnetic properties of nanostructured $Ni_{0.5}Zn_{0.5}Fe_2O_4$. *J. Phys. D: Appl. Phys.* 39 (2006) 4688.

[156] N.-O. Ikenaga, Y. Ohgaito, T. Suzuki, H_2S absorption behavior of calcium ferrite prepared in the presence of coal. *Energy & Fuels* 19 (2005) 170.

[157] D. Hirabayashi, Y. Sakai, T. Yoshikawa, K. Mochizuki, Y. Kojima, K. Suzuki, K. Ohshita, Y. Watanabe, Mössbauer characterization of calcium–ferrite oxides prepared by calcining Fe_2O_3 and CaO. *Hyperfine Interact.* 176 (2006) 809.

[158] E. V. Tsipis, Y. V. Pivak, J. C. Waerenborgh, V. A. Kolotygin, A. P. Viskup, V. V. Kharton, Oxygen ionic conductivity, Mössbauer spectra and thermal expansion of $CaFe_2O_{4-\delta}$. *Solid State Ionics* 178 (2007) 1428.

[159] S. B. Hana, F. F. Abdel-Mohsen, H. S. Emira, Preparation and characterization of magnesium and calcium ferrite pigments. *Interceram* 56 (2007) 1.

[160] N. Sharma, K. M. Shaju, G. V. Subba Rao, B. V. R. Chowdari, Iron-tin oxides with $CaFe_2O_4$ structure as anodes for Li-ion batteries. *J. Power Sources* 124 (2003) 204.

[161] D. Hirabayashi, T. Yoshikawa, K. Mochizuki, K. Suzuki, Y. Sakai, Formation of brownmillerite type calcium ferrite ($Ca_2Fe_2O_5$) and catalytic properties in propylene combustion. *Catal. Lett.* 110 (2006) 269.

[162] R. A. Candeia, M. I. B. Bernardi, E. Longo, I. M. G. Santos, A. G. Souza, Synthesis and characterization of spinel pigment $CaFe_2O_4$ obtained by the polymeric precursor method. *Mater. Lett.* 58 (2004) 569.

[163] X. Ma, M. Zheng, W. Liu, Y. Qian, B. Zhang, W. Liu, Dechlorination of hexachlorobenzene using ultrafine Ca-Fe composite oxides. *J. Hazard. Mater.* 127 (2005) 156.

[164] V. Berbenni, A. Marini, G. Bruni, C. Milanese, Solid state formation of calcium ferrites from thermal decomposition of mixtures $Ca_3(C_6H_5O_7)_2{\cdot}4H_2O–Fe_2(C_2O_4)_3{\cdot}6H_2O$: The role of mechanical activation on the mechanism of the thermal decomposition and the temperature of the ferrites formation. *J. Anal. Appl. Pyrolysis* 82 (2008) 255.

[165] L. A. Isupova, S.V. Tsibulya, G. N. Kryukova, A. A. Budneva, E. A. Paukshtis, G. S. Litvak, V. P. Ivanov, V. N. Kolumuchuk, Yu. T. Pavlyukhin, V. A. Sadykov, Mechanochemical synthesis and catalytic properties of the calcium ferrite $Ca_2Fe_2O_5$. *Kinet. Catal.* 43 (2002) 122.

[166] M. I. Gomez, I. A. de Moran, R. E. Carbonio, P. J. Aymonino, Synthesis of $A\mathrm{FeO}_{2.5+x}$ ($0 \leq x \leq 0.5$; A = Sr, Ca) mixed oxides from the oxidative thermal decomposition of $A[\mathrm{Fe(CN)_5NO}]{\cdot}4H_2O$. *J. Solid State Chem.* 142 (1999) 138.

[167] E. G. Avvakumov, *Mechanical Methods of Activating Chemical Processes.* Nauka, Novosibirsk, 1986 (in Russian).

[168] E. Avvakumov, M. Senna, N. Kosova, *Soft Mechanochemical Synthesis: A Basis for New Chemical Technologies.* Kluwer Academic Publishers, Boston, 2001.

[169] A. Hudson, H. J. Whitfield, Mössbauer effect studies on calcium ferrites. Part I. Temperatures above the Néel point. *J. Chem. Soc. A* (1967) 376.

[170] S. Chatterjee, S. Sengupta, T. Saha-Dasgupta, Site preference of Fe atoms in $FeMgSiO_4$ and $FeMg(SiO_3)_2$ studied by density functional calculations. *Phys. Rev. B* 79 (2009) 115103.

[171] M. N. Taran, M. Koch-Müller, Octahedral cation ordering in Mg, Fe^{2+}- olivine: an optical absorption spectroscopic study. *Phys. Chem. Minerals* 33 (2006) 511.

[172] N. Aikaw, M. Kumazawa, M. Tokonami, Temperature dependence of intersite distribution of Mg and Fe in olivine and the associated change of lattice parameters. *Phys. Chem. Minerals* 12 (1985) 1.

[173] K. D. Becker, In situ spectroscopy in solid state chemistry, *Solid State Ionics* 141-142 (2001) 21.

[174] W. Lottermoser, K. Steiner, M. Grodzicki, K. Jiang, G. Scharfetter, J. W. Bats, G. Redhammer, W. Treutmann, S. Hosoya, G. Amthauer, The electric field gradient in synthetic fayalite α-Fe_2SiO_4 at moderate temperatures. *Phys. Chem. Minerals* 29 (2002) 112.

[175] L. Takacs, Metal-metal oxide systems for nanocomposite formation by reaction milling. *Nanostruct. Mater.* 2 (1993) 241.

[176] D. Basset, P. Matteazzi, F. Miani, G. Le Caër, Kinetic effects in the mechanically activated solid-state reduction of haematite. *Hyperfine Interact.* 95 (1994) 2235.

[177] K. Tokomitsu, Reduction of metal oxides by mechanical alloying method. *Solid State Ionics* 101-103 (1997) 25.

[178] A. Kerr, N. J. Welham, P. E. Willis, Low temperature mechanochemical formation of titanium carbonitride. *Nanostruct. Mater.* 11 (1999) 233.

[179] G. F. Goya, H. R. Rechenberg, Mechanosynthesis of intermetallic $Fe_{100-x}Al_x$ obtained by reduction of Al/Fe_2O_3 composite. *J. Phys. Condens. Matter* 12 (2000) 10579.

[180] T. Kosmac, T. H. Courtney, Milling and mechanical alloying of inorganic nonmetallics. *J. Mater. Res.* 7 (1992) 1519.

[181] W. A. Kaczmarek, B. W. Ninham, Preparation of Fe_3O_4 and γ-Fe_2O_3 powders by magnetomechanical activation of hematite. *IEEE Trans. Magn.* 30 (1994) 732.

[182] S. J. Campbell, W. A. Kaczmarek, G. M. Wang, Mechanochemical transformation of haematite to magnetite. *Nanostruct. Mater.* 6 (1995) 735.

[183] J. Z. Jiang, Y. X. Zhou, S. Mørup, C. B. Koch, Microstructural evolution during high energy ball milling of Fe_2O_3-SiO_2 powders. *Nanostruct. Mater.* 7 (1996) 401.

[184] M. Zdujić, Ć. Jovalekić, Lj. Karanović, M. Mitrić, The ball milling induced transformation of α-Fe_2O_3 powder in air and oxygen atmosphere. *Mater. Sci. Eng. A* 262 (1999) 204.

[185] H. Yang, P. G. McCormick, Combustion reaction of zinc oxide with magnesium during mechanical milling. *J. Solid State Chem.* 107 (1993) 258.

[186] J. Ding, W. F. Miao, T. Tsuzuki, P. G. McCormick, R. Street, In: *Synthesis and Processing of Nanocrystalline Powder.* D. L. Bourell (Ed.), TMS, Warrendale, 1996, p. 69.

[187] N. J. Welham, Mechanochemical reduction of $FeTiO_3$ by Si. *J. Alloy Compd.* 274 (1998) 303.

[188] N. J. Welham, Formation of micronised WC from scheelite ($CaWO_4$). *Mater. Sci. Eng. A* 248 (1998) 230.

[189] L. Takacs, Reduction of magnetite by aluminum: a displacement reaction induced by mechanical alloying. *Mater. Lett.* 13 (1992) 119.

[190] M. Sorescu, Phase transformations induced in magnetite by high energy ball milling. *J. Mater. Sci. Lett.* 17 (1998) 1059.

[191] Y. Shi, J. Ding, Strong unidirectional anisotropy in mechanically alloyed spinel ferrites. *J. Appl. Phys.* 90 (2001) 4078.

[192] G. F. Goya, H. R. Rechenberg, J. Z. Jiang, Structural and magnetic properties of ball milled copper ferrite. *J. Appl. Phys.* 84 (1998) 1101.

[193] V. Šepelák, M. Menzel, K. D. Becker, F. Krumeich, Mechanochemical reduction of magnesium ferrite. *J. Phys. Chem.* B 106 (2002) 6672.

[194] R. Justin Joseyphus, A. Narayanasamy, N. Sivakumar, M. Guyot, R. Krishnan, N. Ponpandian, K. Chattopadhyay, Mechanochemical decomposition of $Gd_3Fe_5O_{12}$ garnet phase. *J. Magn. Magn. Mater.* 272–276 (2004) 2257.

[195] A. Teleki, M. Suter, P. R. Kidambi, O. Ergeneman, F. Krumeich, B. J. Nelson, S. E. Pratsinis, Hermetically coated superparamagnetic Fe_2O_3 particles with SiO_2 nanofilms. *Chem. Mater.* 21 (2009) 2094.

[196] D. Li, W. Y. Teoh, R. C. Woodward, J. D. Cashion, C. Selomulya, R. Amal, Evolution of morphology and magnetic properties in silica/maghemite nanocomposites. *J. Phys. Chem. C* 113 (2009) 12040.

[197] J. Z. Jiang, Y. X. Zhou, S. Mørup, C. B. Koch, Microstructural evolution during high energy ball milling of Fe_2O_3-SiO_2 powders. *Nanostruct. Mater.* 7 (1996) 401.

List of Figures

Curriculum Vitae

Personal details

First name, surname: Maksym, Myndyk
Academic title: Master in Electronics
Date of birth: 24. November 1981
Place of birth: Mshana, Lviv region, Ukraine
Nationality: Ukrainian
Marital status: Single
Parents: Roman Myndyk and Nadiya Myndyk

Schooling

09/1989-05/1993	Primary School in Mshana, Lviv region, Ukraine
09/1993-06/1999	Secondary School in Mshana, Lviv region, Ukraine

Study

09/1999 – 12/2004	Study at Lviv Polytechnic National University, Lviv, Ukraine
21.12.2004	Bachelor degree
31.12.2004	Master's degree in Electronics graduated from Lviv Polytechnic National University Diploma Thesis: "Magnetization Processes of the Epitaxial Thin Films of Iron-Yttrium Garnets" under supervision of Prof. S. Ubizskii, Institute of Telecommunications, Radio Electronics and Electronic Engineering, Lviv, Ukraine

Graduation

06/2005 – 05/2008	Recipient of Georg Christoph Lichtenberg Fellowship (State of Lower Saxony, Germany)
06/2008 – 03/2010	Scientific co-worker at the Institute of Physical and Theoretical Chemistry, Technische Universität Braunschweig, Germany, under supervision of Prof. K.-D. Becker and Prof. V. Šepelák